

**7TH INTERNATIONAL CONFERENCE
ON
SIMULATION AND MODELLING
IN THE
FOOD AND BIO-INDUSTRY
2012**

FOODSIM'2012

**EDITED BY
Horst-Christian Langowski
and
Sven Franke**

**JUNE 18-20, 2012
FREISING, GERMANY**

A Publication of EUROSIS-ETI

Printed in Ghent, Belgium

7th International Conference on
Simulation and Modelling
in the
Food and Bio-Industry
FREISING, GERMANY

JUNE 18-20, 2012

Organised by

ETI

The European Technology Institute

In Cooperation with

TU München

Fraunhofer IVV

Sponsored by

EUROSIS

The European Simulation Society

LMS

Ghent University

University of Skovde

BITE

Higher Technological Institute

Hosted by

**Fraunhofer Institute for
Process Engineering and Packaging IVV
Freising, Germany**

EXECUTIVE EDITOR

PHILIPPE GERIL
(BELGIUM)

EDITORS

General Conference Chair

Prof. Dr. rer. nat. Horst-Christian Langowski
TU München
Freising-Weihenstephan, Germany

General Program Chairs

Dr. Hannes Petermeier
TU München
Freising-Weihenstephan, Germany

Dr. Kathrin Mathmann
TU München
Freising-Weihenstephan, Germany

Local Programme Committee

Dipl.-Ing. Sven Franke
TU München
Freising-Weihenstephan, Germany

Christoph Nophut
TU München
Freising-Weihenstephan, Germany

International Programme Committee

Simulation in Food Engineering and Processing

Lionel Boillereaux (ONIRIS, Nantes, France)
Cedric Brandam (INPT-ENSIACET, Toulouse, France)
Matthew de Roode (NIZO, The Netherlands)
Jean-Yves Monteau (ONIRIS, Nantes, France)
Olivier Vitrac (INRA-UMR FARE, Reims, France)

Simulation in Food Sciences and Biotechnology

Francis Butler (UCD, Dublin, Ireland)
Enda Cummins (UCD, Dublin, Ireland)

Methods and Tools Applied to Food and Bio-Industries

Kristel Bernaerts (Katholieke Universiteit, Leuven, Belgium)
Pierre-Sylvain Mirade (INRA-Theix, St Genes Champanelle, France)
Leon Rothkrantz (Delft University of Technology, Delft, The Netherlands)
Xavier Serra (IRTA, Girona, Spain)

International Programme Committee

Methods and tools applied to Food Quality and Safety Evaluation

Manuel Rui Alves (IPV, Viana Castelo, Portugal)
Joana Amaral (ESTiG-IPB, Bragança, Portugal)
Ursula Gonzales Barron (University College Dublin, Food Science and Veterinary Medicine, Ireland)
Vasco Cadavez (ESA-IPB, Bragança, Portugal)
Luis Dias (ESA-IPB, Bragança, Portugal)
Isabel Ferreira (ESA-IPB, Bragança, Portugal)
Isabel Mafra (REQUIMTE, Porto, Portugal)
Beatriz Oliveira (FF-UP, Porto, Portugal)
José Alberto Pereira (ESA-IPB, Bragança, Portugal)
Isabel M. Vicario (University of Sevilla, Spain)
Miguel Vilas-Boas (ESA-IPB, Bragança, Portugal)

Simulation in Functional Foods

Lourdes Amigo Garrido (CSIC, Madrid, Spain)
Gianpaolo Ruocco (University of Basilicata, Potenza, Italy)

Simulation in Food Production Management, Economics and Traceability

Martin Cloutier (UQAM, Montreal, Canada)
Magda Aguiar Fontes (Faculdade de Medicina Veterinária, UTL, Lisboa, Portugal)
Martin Grunow (Technical University of Munich, Munich, Germany)
Vincent Hovelaque (INRA, Rennes, France)

Sustainable Food Production

Albino Bento (ESA-IPB, Bragança, Portugal)
Cesar de Prada (University of Valladolid, Spain)
Federico Ferreres (Cebas-CSIC, Murcia, Spain)
Björn Johansson (Chalmers University of Technology, Sweden)
Jaime Pires (ESA-IPB, Bragança, Portugal)
Manuel Ângelo Rodrigues (ESA-IPB, Bragança, Portugal)

Innovation in Traditional Food Products

Maria J. Alcalde (University of Sevilla, Spain)
Leticia Estevinho (ESA-IPB, Bragança, Portugal)
Dietrich Knorr (Technische Universität, Berlin, Germany)
Toomas Paalme (Tallinn University of Technology, Tallinn, Estonia)
Elsa Ramalhosa (ESA-IPB, Bragança, Portugal)

© 2012 EUROSIS-ETI

Responsibility for the accuracy of all statements in each peer-referenced paper rests solely with the author(s). Statements are not necessarily representative of nor endorsed by the European Simulation Society. Permission is granted to photocopy portions of the publication for personal use and for the use of students providing credit is given to the conference and publication. Permission does not extend to other types of reproduction, nor to copying for incorporation into commercial advertising nor for any other profit-making purpose. Other publications are encouraged to include 300- to 500-word abstracts or excerpts from any paper contained in this book, provided credits are given to the author and the conference.

All author contact information provided in this Proceedings falls under the European Privacy Law and may not be used in any form, written or electronic, without the written permission of the author and the publisher. Infringements of any of the above rights will be liable to prosecution under Belgian civil or criminal law.

All articles published in these Proceedings have been peer reviewed

EUROSIS-ETI Publications are ISI-Thomson and IET referenced
Legal Repository: Koninklijke Bibliotheek van België, Keizerslaan 4, 1000 Brussels, Belgium
CIP 12.620 D/2011/12.620/1

Selected papers of this conference are published in scientific journals.

For permission to publish a complete paper write EUROSIS, c/o Philippe Geril, ETI Executive Director, Greenbridge Science Park, Ghent University Ostend Campus, Wetenschapspark 1, Plassendale 1, B-8400 Ostend, Belgium.

EUROSIS is a Division of ETI Bvba, The European Technology Institute, Torhoutsesteenweg 162, Box 4, B-8400 Ostend, Belgium

Printed and bound in Belgium by Reproduct NV, Ghent, Belgium
Cover Design by Grafisch Bedrijf Lammaing, Ostend, Belgium

EUROSIS-ETI Publication
ISBN: 978-90-77381-72-4
EAN: 978-90-77381-72-4

PREFACE

Dear Participants,

It is our great pleasure to welcome you in Freising – Weihenstephan for the 7th International Conference on Simulation and Modelling in the Food and Bioprocess Industry.

More than a century of tradition and experience have made the Centre of Life and Food Sciences Weihenstephan of the Technische Universität München unique in the world. At Weihenstephan interdisciplinary networking amongst all the life science departments enables the exploration of the entire life cycle of foodstuffs and raw materials. The Centre of Life and Food Sciences Weihenstephan is the largest faculty of the Technische Universität München and enjoys a global recognition in this area.

The Fraunhofer Institute for Process Engineering and Packaging (IVV), which is also located in Freising, complements this extraordinary research infrastructure. Its competent and professional organization carries out contract research and development work for the industry.

At both these research locations, mathematical modelling and simulation plays an important role for the optimization and management in the food and bio-processing area.

Thus we see FOODSIM'2012 as a platform to exchange ideas and modelling techniques and as an opportunity to expand the network for researchers, food experts and industrial users in the field of simulation and modelling in the Food and Bioprocess Industry.

We are looking forward to lively discussions and hope that this meeting will give you the opportunity to build contacts for future co-operation.

Your local committee

Sven Franke
Chair of Food Packaging Technology
Technische Universität München, Freising, Germany

Prof. Dr. Horst-Christian Langowski
Chair of Food Packaging Technology
Technische Universität München, Freising, Germany
and
Fraunhofer Institute for Process Engineering and Packaging (IVV)
Freising, Germany

Preface	VII
Scientific Programme	1
Author Listing	107

SIMULATION METHODOLOGY IN FOOD SCIENCES

Design of dynamic Experiments for Discrimination between Models for microbial Growth Kinetics as a Function of Temperature I. Stamati, F. Logist, E. Van Derlinden and J. Van Impe	5
--	----------

Molecular Dynamics Simulations as a Predictive Tool for the Behavior of Fats in High-Pressure Processes Maximilian Greiner, Ekaterina Elts and Heiko Briesen	10
--	-----------

Population Balance Modelling of Flocculation of Biological Cells Andre Braun and Heiko Briesen.....	15
---	-----------

Towards optimized salt perception: simulation and correlation of salt release during mastication Georg C. Ganzenmüller, Christian Zacherl and Regina Fischl,.....	20
---	-----------

SIMULATION IN FOOD PROCESSING

Simulation Model Design and Assessment of Nanoparticle Migration from a Nanocomposite with Experimental Validation Maeve Cushen and Enda Cummins	29
--	-----------

Computational Fluid Dynamics (CFD) modelling of the fluidised bed coating process Frederik Ronsse, Wasan Duangkhamchan, Koen Dewettinck and Jan G. Pieters	34
--	-----------

ENERGY APPLICATIONS IN FOOD PRODUCTION

Simulation based Energy Management Tools for the Food Processing Industry Sven Franke, Josef Höfler, Isabel Osterroth, Tobias Voigt, Horst–Christian Langowski and Hannes Petermeier.....	45
---	-----------

Energy Based Production Plan Assessment and Optimization Josef Höfler, Hannes Petermeier, Sven Franke, Veronika Strobl, and Horst–Christian Langowski	52
---	-----------

CONTENTS

Effect of Electron Beam Irradiation Doses in Antioxidant Activity and Phenolics Content of Portuguese Chestnuts

Márcio Carochó, Lillian Barros, Albino Bento, Isabel C.F.R. Ferreira, Amílcar L. Antonio and Iwona Kałuska.....59

Compartment Modelling in Drying of Gamma Irradiated Chestnut Fruits

Amílcar L. Antonio, Elsa Ramalhosa, Albino Bento, Mauro Trindade, Guillermo Sanchez, M. Luisa Botelho, Begoña Quintana62

FOOD CONTAMINATION AND SAFETY MEASURES

AFM1 Exposure in the French Population via Milk Products Consumption using Monte Carlo Simulation

Nathalie Wesolek and Alain-Claude Roudot67

Software Tool for Assessment of Food Contamination and Food Bans Regulations

Petr Pecha, Radek Hofman and Emilie Pechova.....72

Combined Effects of γ -irradiation and Storage Times on Sugars Composition of *Lactarius deliciosus*: Comparison through Linear Discriminant Analysis

Ângela Fernandes, João C.M. Barreira, Anabela Martins, Isabel C.F.R. Ferreira, M. Beatriz P.P. Oliveira and Amílcar L. Antonio77

A Meta-Analytical Assessment of the Variability between Abattoirs in the Effect of Chilling on the *Salmonella* incidence on Pig Carcasses

Ursula Gonzales-Barron, James Sheridan, Francis Butler and Vasco Cadavez.....80

FOOD PACKAGING

Modelling and Numerical Simulation of Water Vapour Sorption Kinetics in Humidity regulating Polypropylene Films containing Sodium Chloride

Solange Sanahuja, Oliver Miesbauer, Ellen Reichmann and Sven Sänglerlaub91

Permeation through Passive and Active Barrier Materials – A Continuum Theoretical Approach

Oliver Miesbauer.....98

SCIENTIFIC PROGRAMME

**SIMULATION
METHODOLOGY
IN
FOOD
SCIENCES**

DESIGN OF DYNAMIC EXPERIMENTS FOR DISCRIMINATION BETWEEN MODELS FOR MICROBIAL GROWTH KINETICS AS A FUNCTION OF TEMPERATURE.

I. Stamati, F. Logist, E. Van Derlinden and J. Van Impe

BioTeC & OPTEC - Chemical and Biochemical Process Technology and Control,
Department of Chemical Engineering, KU Leuven, W. de Croylaan 46, B-3001 Leuven, Belgium
email: [ioanna.stamati, filip.logist, eva.vanderlinden, jan.vanimpe]@cit.kuleuven.be

KEYWORDS

optimization, dynamic modelling, parameter identification, nonlinear, agriculture

ABSTRACT

In the field of predictive microbiology, mathematical models play an important role for describing the microbial growth, survival and inactivation. Often different models are available for describing the microbial dynamics in a similar way. However, the model that describes the system in the *best* way is desired. Optimal experiment design for model discrimination (OED-MD) is an efficient tool for discriminating among rival models.

In this work the OED-MD method proposed by Schwaab et al. (2008) and Donckels et al. (2010) will be used for discriminating among dynamic models of microbial growth rate as a function of temperature. This method provides experiments with an increased discriminatory potential and better estimates of the uncertainties.

Results from a simulation study indicate that it is possible to validate the case that one of the proposed models is more accurate for describing the temperature effect on the microbial growth rate.

INTRODUCTION

The need to find the best model arises when different models are proposed for the same process. For describing the influence of temperature on the microbial growth rate there exist several models in predictive microbiology. Two of these models are the CTMI (Cardinal Temperature Model with Inflection (Rosso et al. 1993)) and the aCTMI (adapted CTMI (Le Marc et al. 2002)). Up to now, it is assumed that the CTMI is valid for all strains. Divergence from this model only has been observed for *Listeria* (Le Marc et al. 2002) and *E. coli* K12 (Van Derlinden et al. 2012).

The idea is to use experimental design to discriminate between the available models. New experimental conditions will be designed that maximize the difference between the outputs of the different models. There ex-

ist in literature several criteria which take this difference into account. In the current work the method proposed by Schwaab et al. (2008) and Donckels et al. (2010) will be used. The criterion includes the posterior covariance matrix of estimated model parameters. This approach provides conditions for an increased discriminatory prospective in combination with better estimates of the model parameter values.

The paper is structured as follows. In the first part the case study with the two proposed models are presented. In the second part the methodology both in theory and practice is outlined. Finally in the last part the results from the discrimination between the CTMI and aCTMI are presented followed by the conclusions.

CASE STUDY

The growth model of the cell density as a function of time of Baranyi and Roberts (1994) is used:

$$\begin{aligned}\frac{dn(t)}{dt} &= \frac{Q(t)}{Q(t)+1} \cdot \mu_{max}(T(t)) \cdot [1 - \exp(n(t) - n_{max})] \\ \frac{dQ(t)}{dt} &= \mu_{max}(T(t)) \cdot Q(t)\end{aligned}$$

with $n(t)$ [ln(CFU/mL)] the cell density at time t [h], n_{max} [ln(CFU/mL)] the maximum value for $n(t)$ and μ_{max} [1/h] the maximum specific growth rate. $Q(t)$ [-] is a measure for a physiological state of the cells. For this work $Q(t)$ is excluded (see Van Derlinden et al. (2010) for details). The microbial growth rate as a function of temperature can be described by CTMI and aCTMI.

The CTMI model is described by:

$$\mu_{max} = \gamma \cdot \mu_{opt} \quad (1)$$

with

$$\gamma = \begin{cases} 0 & T \leq T_{min} \text{ or } T \geq T_{max} \\ \frac{(T - T_{min})^2 (T - T_{max})}{(T_{opt} - T_{min})(\gamma_A - \gamma_B)} & T_{min} < T < T_{max} \end{cases}$$

$$\begin{aligned}\gamma_A &= (T_{opt} - T_{min})(T - T_{opt}) \\ \gamma_B &= (T_{opt} - T_{max})(T_{opt} + T_{min} - 2T)\end{aligned} \quad (2)$$

The parameters included in this model are the three cardinal temperatures $T_{min}[^{\circ}\text{C}]$, $T_{opt}[^{\circ}\text{C}]$ and $T_{max}[^{\circ}\text{C}]$ (i.e., the minimum, optimum and maximum temperature for growth, respectively) and $\mu_{opt}[1/h]$ (the maximum specific growth rate at T_{opt}).

The aCTMI model is described in a similar way as the CTMI but with a different γ function:

$$\gamma = \begin{cases} 0 & T \leq T_{min} \text{ or } T \geq T_{max} \\ \frac{(T - T_1)^2(T - T_{max})}{(T_{opt} - T_1)(\gamma_C - \gamma_D)} & T_{min} < T < T_c \\ \frac{(T_c - T_1)^2(T_c - T_{max})}{(T_{opt} - T_1)(\gamma_E - \gamma_F)} \gamma_G & T_c < T < T_{max} \end{cases}$$

$$\begin{aligned} \gamma_C &= (T_{opt} - T_1)(T - T_{opt}) \\ \gamma_D &= (T_{opt} - T_{max})(T_{opt} + T_1 - 2T) \end{aligned}$$

$$\begin{aligned} \gamma_E &= (T_{opt} - T_1)(T_c - T_{opt}) \\ \gamma_F &= (T_{opt} - T_{max})(T_{opt} + T_1 - 2T_c) \end{aligned}$$

$$\gamma_G = \left(\frac{T - T_{min}}{T_c - T_{min}} \right)^2 \quad (3)$$

Apart from the previous parameters the adapted model is defined also by $T_c[^{\circ}\text{C}]$ the so-called change temperature and $T_1[^{\circ}\text{C}]$ the intersection point between the first linear part and the temperature axis. In Figure 1 the $\sqrt{\mu_{max}}$ versus the temperature is displayed for the two models, and their difference in the region of T_{min} can be seen.

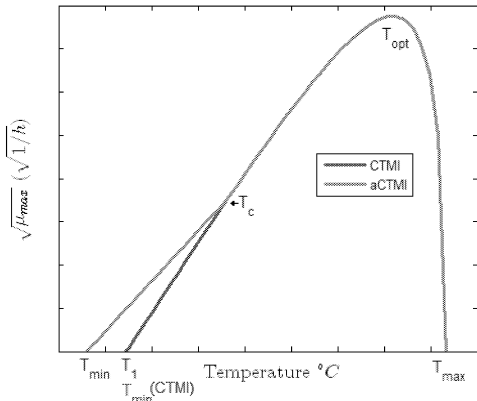


Figure 1: $\sqrt{\mu_{max}}$ as a function of temperature for the CTMI and aCTMI models

METHODOLOGY

The procedure followed for OED-MD is illustrated in Figure 2 and the different steps are explained.

Preliminary experiment

An initial experiment is required in order to have an estimate of the unknown parameters. This experiment is chosen arbitrarily and will provide measurements for the initial parameter values.

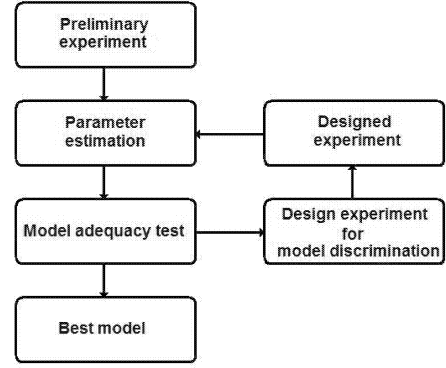


Figure 2: Steps for OED-MD (Donckels et al. 2010).

Parameter estimation

Given an input (preliminary or designed) and the corresponding experimental data parameters can be estimated. Parameters are selected such that the model predictions $\mathbf{y}(\mathbf{p}, t_i)$ fit the measurements $\mathbf{y}_{exp}(t_i)$, at times t_i , as accurately as possible despite the presence of measurement errors. The most common assumption about the probability distribution of the measurement errors is that they are additive, independent and identically distributed according to a Gaussian distribution. These assumptions typically lead to a *weighted sum of squares* objective (WSSE) (Walter et al. 1997)

$$J(\mathbf{p}) = \sum_{i=1}^{n_t} (\mathbf{y}(\mathbf{p}, t_i) - \mathbf{y}_{exp}(t_i))^T \mathbf{Q} (\mathbf{y}(\mathbf{p}, t_i) - \mathbf{y}_{exp}(t_i)) \quad (4)$$

with n_p the number of parameters and n_t the number of measurements. The *weighting matrix* \mathbf{Q} is typically selected as the inverse of the measurement error variance-covariance matrix.

Model adequacy test

To be able to discriminate between the two models there should be a proof that one model is unable to fit accurately to the data, whereas the other model is able. The use of the χ^2 -test can prove a lack of fit (Chen et al. 2003). Since the measurements are assumed to follow a normal distribution with zero mean and known covariance σ^2 , the WSSE function follows a χ^2 distribution with $n - n_p$ degrees of freedom. This allows the use of the χ^2 adequacy test (Donckels et al. 2009). If the WSSE value is above the $\chi_{n_e - n_p}^2$ value ($n_e =$ number of experiment points, $n_p =$ the number of unknown parameters) then there is a lack of fit.

Experiment design for model discrimination

Optimal experiment design for dynamic systems leads to a particular class of optimal control problems:

$$\min_{\mathbf{u}} J \quad (5)$$

subject to:

$$\frac{d\mathbf{x}}{dt} = \mathbf{f}(\mathbf{x}(t), \mathbf{u}(t), \mathbf{p}, t) \quad t \in [0, t_f] \quad (6)$$

$$\mathbf{0} = \mathbf{b}_c(\mathbf{x}(0), \mathbf{p}) \quad (7)$$

$$\mathbf{0} \geq \mathbf{c}_p(\mathbf{x}(t), \mathbf{u}(t), \mathbf{p}, t) \quad (8)$$

Here, \mathbf{x} are the state variables, \mathbf{u} the time-varying control inputs and \mathbf{p} the model parameters. The vector \mathbf{f} represents the dynamic system equations (on the interval $t \in [0, t_f]$) with initial conditions given by the vector \mathbf{b}_c . The vector \mathbf{c}_p indicates path inequality constraints on the states, controls and parameters. \mathbf{y} are the measured outputs, which are typically a subset of the state variables \mathbf{x} .

The objective function J for model discrimination is typically a discrimination criterion that maximizes the difference between the model outputs. In the current work the criterion for discriminating between model m and n , for experiment $\xi_{n_e+1} = (u_{n_e+1}(t), t, p)$ (n_e : number of available experiments) is:

$$\mathbf{D}_{m,n}(\xi_{n_e+1}) = d_{m,n}^T(\xi_{n_e+1}) \mathbf{V}_{m,n}^{-1}(\xi_{n_e+1}) d_{m,n}(\xi_{n_e+1}) \quad (9)$$

with:

$$\begin{aligned} d_{m,n}(\xi_{n_e+1}) &= \mathbf{y}_m(\xi_{n_e+1}) - \mathbf{y}_n(\xi_{n_e+1}) \\ \mathbf{V}_{m,n}(\xi_{n_e+1}) &= 2\mathbf{V} + \mathbf{V}_m(\xi_{n_e+1}) + \mathbf{V}_n(\xi_{n_e+1}) \\ \mathbf{V}_m(\xi_{n_e+1}) &= \mathbf{B}_m(\xi_{n_e+1}) \mathbf{V}_{p,m}(\xi_{n_e+1}) \mathbf{B}_m^T(\xi_{n_e+1}) \\ \mathbf{V}_{p,m}(\xi_{n_e+1}) &= [\mathbf{B}_m^T(\xi_{n_e+1}) \mathbf{V}^{-1} \mathbf{B}_m(\xi_{n_e+1}) + \\ &\quad \mathbf{V}_{p,m}^{-1}(\xi_{n_e})]^{-1} \end{aligned}$$

Here $\mathbf{y}_m(\xi_{n_e+1})$ is the *output for model m* (similarly for model n), $\mathbf{V}_{m,n}(\xi_{n_e+1})$ is the *posterior covariance matrix* of the differences between model predictions, \mathbf{V} is the *covariance matrix of the experimental deviations* and $\mathbf{V}_m(\xi_{n_e+1})$ is the *covariance matrix of model prediction variations* calculated from model m (and similar for model n). The model uncertainty includes the uncertainty on the model predictions and on the measurements (Donckels et al. 2009). $\mathbf{B}_m(\xi_{n_e+1})$ is the sensitivity matrix that contains the first derivatives of model m responses with respect to its parameters $\left(\frac{\partial \mathbf{y}_m(\xi_{n_e+1})}{\partial \mathbf{p}} \right)$.

$\mathbf{V}_{p,m}(\xi_{n_e+1})$ is the *posterior covariance matrix of model parameters*. It can be seen that $\mathbf{V}_{p,m}$ consists two parts, i.e., the covariance matrix of the new designed experiment with input $\mathbf{u}_{n_e+1}(t)$ and the current covariance matrix of the parameter estimates. The covariance matrix of the estimated parameters is approximated by the Fisher information matrix (FIM) (Walter et al. 1997).

The primary objective is the increase of the discrimination power but a decrease of the parameter variances is obtained as well, with the use of the posterior covariance matrix of parameter estimates (Schwaab et al. 2008).

Best model

After the model adequacy test it can be checked whether only one model is able to accurately describe the data. Otherwise the loop has to be entered again and a new discriminatory experiment has to be designed.

IMPLEMENTATION

The aCTMI model coincides the CTMI model if parameters T_c [°C] and T_1 [°C] are well chosen. Whereas the CTMI model does not always coincide the aCTMI model. This will be verified with the use of model discrimination techniques. Assuming aCTMI is the *correct* model, *in silico* data have been created and used as measurement data. The discrimination procedure as explained previously has been applied for this data. More specifically the steps followed are:

- i The preliminary experiment is performed *in silico* by generating data from the aCTMI model and adding an error with known variance.
- ii The generated data is used for estimating the parameters of both models CTMI and aCTMI.
- iii A discriminatory experiment is designed. The designed inputs are applied and the data are obtained (again *in silico*).
- iv Using all the data the parameters for both models are re-estimated. The χ^2 -test is applied.
- v According to the test results a model is selected or a new discriminatory experiment is designed.

Input profile

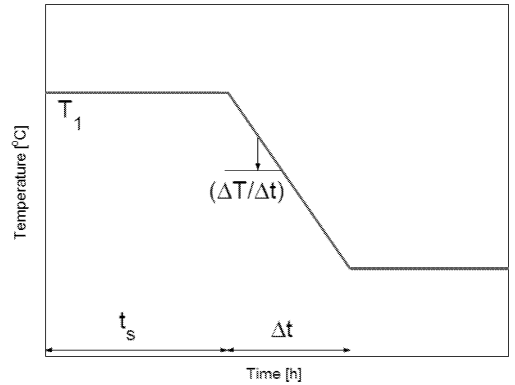


Figure 3: Representation of the parameterized temperature profile (Van Derlinden et al. 2010).

The input profile (Figure 3) is parametrized with four degrees of freedom: T_1 [°C] the initial temperature, t_s [h] the time at which the increase or decrease in temperature starts, $\Delta T/\Delta t$ [°C/h] the rate of temperature change and Δt [h] the duration of the temperature change (Van Derlinden et al. 2010).

This input profile is optimized for the discrimination experiment. The temperature is allowed to be in the region of $[0, 45]^{\circ}\text{C}$, the total time is 38 hours with a sampling time of 1 hour.

Measurement data and parameters

The parameters used for generating the pseudo-measurements are $\mu_{opt} = 2.41$ 1/h, $T_{min} = 5.67^{\circ}\text{C}$, $T_c = 23^{\circ}\text{C}$ and $T_1 = 12.3^{\circ}\text{C}$ (Van Derlinden et al. 2012). The error added to the output data (for generating the pseudo-measurements) has a variance $\sigma^2 = (3.27 \cdot 10^{-2})^2$. The two models differ in the temperature region below T_{opt} , therefore for this work the temperature parameters T_{opt} and T_{max} are identical for both models and based on previous estimations (Van Derlinden et al. (2012)). For the CTMI model, two parameters are unknown (i.e., μ_{opt} and T_{min}), whereas four parameters have to be identified for the aCTMI (i.e., μ_{opt} , T_{min} , T_c and T_1).

Algorithms

The parameter estimation is performed with the lsqnonlin matlab function. This function solves a least squares problem using the trust-region-reflective algorithm. The optimal experiment design is solved with the patternsearch matlab function from the global optimization toolbox. This function finds the minimum of the objective function using a pattern search algorithm.

RESULTS

The preliminary experiment (with input $u = [T_1 = 13^{\circ}\text{C}, t_s = 10$ h, $\Delta T/\Delta t = 0.5^{\circ}\text{C/h}$, $\Delta t = 25^{\circ}\text{C}$] Figure 4) is performed *in silico* generating data from the aCTMI model. The obtained data are used for parameter estimation, the resulting estimated parameters can be found in Table 1. The pseudo-measurements together with the model outputs using the estimated parameters are displayed in Figure 5. The model adequacy test is performed and both models are able to fit the data. The next step is the design of the discriminatory experiment based on the method explained in the previous section. The discrimination value obtained is $D = 2616.3$ for input $u = [T_1 = 40.87^{\circ}\text{C}, t_s = 4.12$ h, $\Delta T/\Delta t = -5^{\circ}\text{C/h}$, $\Delta t = 6.48^{\circ}\text{C}$].

An experiment using the new designed input (first discrimination input in Figure 4) is performed again *in silico*. The new obtained data together with the previous data are used for re-estimating the parameters. The parameter values can be seen in Table 1 whereas the outputs of the two models (using the new found parameters) and the pseudo-measurements using both the preliminary and the first designed inputs are displayed in Figure 6.

The model adequacy test proves that the aCTMI is the best model (see Table 2). And this because the WSSE

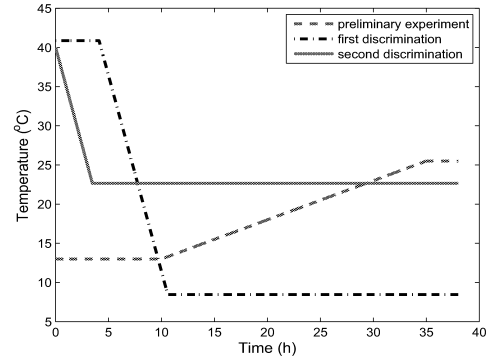


Figure 4: Temperature profile for every of the three experiments.

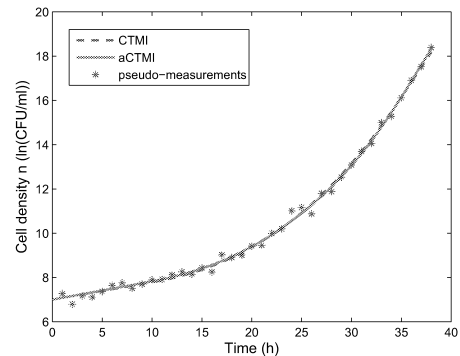


Figure 5: CTMI and aCTMI model outputs after the estimation together with the pseudo-measurements for the preliminary experiment.

value of the CTMI model is above the $\chi_{n-n_p}^2$ and thus indicates that the CTMI can not describe the data accurately. Whereas the WSSE value of the aCTMI model is below the $\chi_{n-n_p}^2$ and indicates a good fit. To increase the discrimination an additional experiment is designed and performed.

Table 1: Parameter values

model	μ_{opt} [1/h]	T_{min} [$^{\circ}\text{C}$]	T_c [$^{\circ}\text{C}$]	T_1 [$^{\circ}\text{C}$]
original aCTMI	2.41	5.67	23	12.3
preliminary experiment				
CTMI	1.71	6.81		
aCTMI	2.12	6.10	21.79	10.15
first designed experiment				
CTMI	2.36	9.27		
aCTMI	2.41	5.99	22.66	11.94
second designed experiment				
CTMI	2.27	9.47		
aCTMI	2.40	5.81	22.66	12.05

The second discrimination experiment gives a discrimination value $D = 892.85$ for input $u = [T_1 = 40.06^{\circ}\text{C}, t_s = 0$ h, $\Delta T/\Delta t = -5^{\circ}\text{C/h}$, $\Delta t = 3.48^{\circ}\text{C}$] (see Figure 4).

Again the new experimental data together with the ones from the two previous experiments are used for estimat-

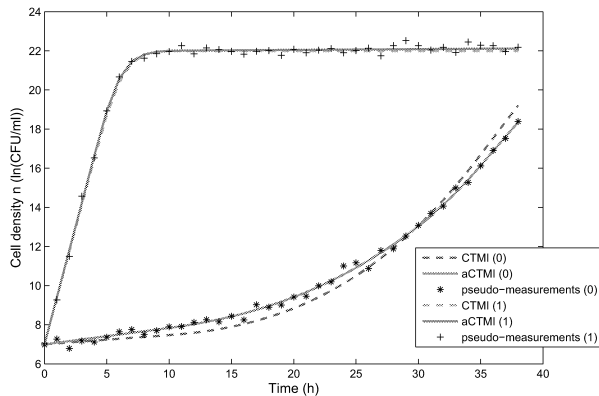


Figure 6: CTMI and aCTMI model outputs after the new estimation together with the pseudo-measurements using the preliminary (0) and first designed (1) inputs.

ing the unknown parameters. In Table 1 it can be seen that the parameters are closer to the original. This is accomplished through the use of the posterior covariance matrix in the discrimination (see Equation (9)).

After the second discrimination experiment it is observable that aCTMI is the *best* model (see Table 2 and Figure 7). Since the experiments are *in silico* and it was known beforehand that aCTMI is the correct model these results confirm the possibility of OED-MD methods do discriminate between the two models.

Table 2: Model adequacy test results

model	WSSE	$\chi^2_{n-n_p}$
After preliminary experiment		
CTMI	40.05	52.19
aCTMI	36.81	49.80
After first discrimination experiment		
CTMI	300.58	97.35
aCTMI	74.45	95.08
After second discrimination experiment		
CTMI	1100	141.03
aCTMI	103.26	138.81

CONCLUSIONS

Between the two models CTMI and aCTMI the question of the *best* model arises. Here, through OED-MD the ability to discriminate between the two models is studied and evaluated. The results from the simulation study show that if the aCTMI model can describe more accurately the region around T_{min} , it is possible through model discrimination to confirm it. In future research, designed experiments for discrimination will be performed in a bioreactor.

ACKNOWLEDGEMENTS

This research is supported by Projects OT/10/035, PFV/10/002 (Center-of-Excellence Optimization in Engineering) of the Research Council of the Katholieke Universiteit Leuven, and Project KP/09/005 (SCORES4CHEM) of the Industrial Research Council of

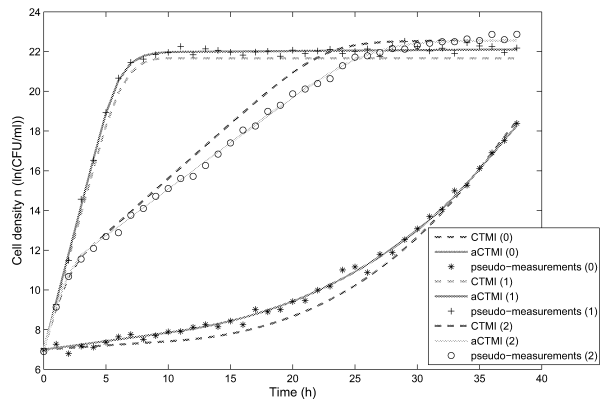


Figure 7: CTMI and aCTMI model outputs after the third estimation together with the pseudo-measurements using the preliminary (0), first designed (1) and second designed (2) inputs.

the Katholieke Universiteit Leuven, and the Belgian Program on Interuniversity Poles of Attraction, initiated by the Belgian Federal Science Policy Office. J. Van Impe holds the chair Safety Engineering sponsored by the Belgian chemistry and life sciences federation *essenscia*. The scientific responsibility is assumed by its authors.

REFERENCES

- Baranyi J. & Roberts, T. A. 1994. "A dynamic approach to predicting bacterial growth in food". *Int. J. Food Microbiol.*, 23, 277–294.
- Chen B.H. & Asprey S.P. 2003. "On the design of optimally informative dynamic experiments for model discrimination in multiresponse nonlinear situations". *Ind. Eng. Chem. Res.*, 1379-1390
- Donckels B.M.R., De Pauw D.J.W., De Baets B., Maertens J. & Vanrolleghem P.A. 2009. "An anticipatory approach to optimal experimental design for model discrimination". *Chemometr. Intell. Lab.*, 95(1): 53-63.
- Le Marc, Y., Huchet, V., Bourgeois, C., Guyonnet, J., Mafart, P. & Thuault, D. 2002. "Modelling the growth kinetics of *Listeria* as a function of temperature, pH and organic acid concentration". *Int. J. Food Microbiol.*, 73, 219-237.
- Rosso, L., Lobry, J. R. & Flandrois, J. P. 1993. "An unexpected correlation between cardinal temperatures of microbial growth highlighted by a new model". *J. Theor. Biol.*, 162, 447–463.
- Schwaab M., Monteiro J.L. & Pinto J.C. 2008. "Sequential Experimental Design for Model Discrimination. Taking Into Account the Posterior Covariance Matrix of Parameter Uncertainties". *Chem. Eng. Science*, 63(9), 2408-2419.
- Van Derlinden, E., Bernaerts, K. & Van Impe, J. F. 2008. "Accurate estimation of cardinal temperatures of *Escherichia coli* from optimal dynamic experiments". *Int. J. Food Microbiol.*, 128, 89–100.
- Van Derlinden, E., Bernaerts, K. & Van Impe, J. F. 2010. "Simultaneous versus sequential optimal experiment design for the identification of multi-parameter microbial growth kinetics as a function of temperature". *J. Theor. Biol.*, 264, 347-355.
- Van Derlinden, E. & Van Impe, J. F. 2012. "Modeling growth rates as a function of temperature: Model performance evaluation with focus on the suboptimal temperature range". *Int. J. Food Microbiol.*, (submitted)
- Walter, E. & Pronzato, L. 1997. *Identification of Parametric Models from Experimental Data*, Springer, Masson.

MOLECULAR DYNAMICS SIMULATIONS AS A PREDICTIVE TOOL FOR THE BEHAVIOR OF FATS IN HIGH-PRESSURE PROCESSES

Maximilian Greiner, Ekaterina Elts and Heiko Briesen
Chair for Process System Engineering
Technische Universität München
85350 Freising, Germany

email: {maximilian.greiner, ekaterinaelts, heiko.briesen}@mytum.de

KEYWORDS

triacylglycerides, phase co-existence, high-pressure processing

ABSTRACT

In this contribution, molecular dynamics simulations are presented as a valuable tool to predict phase-transition diagrams of saturated as well as unsaturated fats. Choosing the Gibbs-Duhem integration with temperature step size as little as 3 K simulations were performed for the three main components of cocoa butter: 1,3-distearoyl-2-oleoylglycerol (SOS), 1-palmitoyl-2-oleoyl-3-stearoylglycerol (POS) and 1,3-dipalmitoyl-2-oleoylglycerol (POP). Such high-resolution results suggest a non-linear, constantly increasing slope towards higher pressures. The proposed method is easily transferable to fats of various chain lengths and double bonds. On modern desktop computers the presented results can be computed within the time scale of hours, making the technique feasible for standard use. It may thus be an important tool to expand the knowledge on the behaviour of the homologous series of saturated and unsaturated fats, of interest for high-pressure processing of food.

INTRODUCTION

High-pressure treatment of food is becoming increasingly important in the food industry. It provides an effective method to extend the shelf-life with less impact on texture when compared with thermal processing (Torres and Velazquez 2005). For a proper design of high-pressure treatment of food, detailed knowledge of their phase behavior is necessary. However, for many food systems there is still a lack of comprehensive data of pressure-dependent thermodynamic properties.

While experimental (Ferstl et al. 2010; 2011) determination of phase behaviour gives reliable and exact results, it is often time-consuming and requires special equipment. This is one reason why experimental data is still scarce and can be cumbersome to obtain.

Thermodynamic model predictions were published previously (Delgado et al. 2008), though the approach demands for in-situ measurement techniques for proper validation.

Molecular dynamics (MD) simulations are a promising alternative. They provide a predictive tool to explore the phase behavior of fats based on the structure of the molecules. By integrating Newton's equation of motion for a set of molecules in a simulation box, it is possible to obtain macroscopic properties like density or diffusion coefficients via thermodynamic analysis of the molecule's trajectories (Allen and Tildesley 1989).

Pioneering molecular simulations of fats focused on the energies of different conformations (Yan et al. 1994). Further force-field development in the 1990s (Chandrasekhar and van Gunsteren 2002), together with increasing computational resources, led to increasingly predictive and physically realistic models. The calculations presented here are based on the NERD force-field from Sum et al. (2003), which has been adopted previously (Hsu and Violi 2009) and thus provides a well-validated (Sum et al. 2003, Hsu and Violi 2009, Greiner et al. 2012) approach for temperature- as well as pressure-dependent calculations.

Our contribution presents MD simulation results, obtained from few-hour timescale calculations with the GROMACS code (Van der Spoel et al. 2005, Hess et al. 2008). Our previously published results (Greiner et al. 2012) focused on fats built from single components of saturated fatty acids only. Many food products, however, largely contain unsaturated fatty acids. For this reason we present the phase transition diagrams for 1,3-distearoyl-2-oleoylglycerol (SOS), 1-palmitoyl-2-oleoyl-3-stearoylglycerol (POS) and 1,3-dipalmitoyl-2-oleoylglycerol (POP), the three main components of cocoa butter - the base material for chocolate. Additionally, a higher degree of automation in the code allowed us to produce more accurate results compared to our previous work.

METHODS

For single component fats there are currently only few phase-transition diagrams available (Lee et al. 2010). To explore the solid-liquid co-existence curve, which is of a particular interest in understanding the interplay between pressure and temperature during processing, we employ a Gibbs-Duhem integration scheme (Kofke 1993b;a). After calculating the slope of the co-existence line for known combinations of temperatures and pressures, the temperature is slightly increased and the pressure is adjusted using the Clausius-Clapeyron equation:

$$\frac{dp}{dT} = \frac{\Delta H_f}{T\Delta V}, \quad (1)$$

where $\frac{dp}{dT}$ gives the slope in a pT phase transition diagram, ΔH_f is the molar enthalpy of fusion, T is the temperature and ΔV is the difference in molar volume between the crystal and liquid state, calculated as (Lee et al. 2010):

$$\Delta V = M \frac{\rho_s - \rho_l}{\rho_s \rho_l}, \quad (2)$$

with M as the molar mass, ρ_s as the mass density for the solid and ρ_l for the liquid phase. A schematic representation of the solid and liquid structures of the simulation cell are given in figure 1. Hence, knowing the value of ΔV at a certain T and p , such as the melting temperature at ambient pressure, an estimate for a linear portion of the solid-liquid co-existence curve can be made.

SIMULATION DETAILS

The Gromacs code (version 4.5.4) was used for all simulations. The liquid as well as the solid simulation boxes contained 160 molecules and were initially pre-equilibrated over 50000 integration steps with a time-step of 2 fs, ensuring constant potential energies. All simulations were performed in an NPT ensemble using the Parrinello-Rahman barostat, as well as the Nosé-Hoover temperature coupling (Allen and Tildesley 1989). Periodic boundary conditions were applied in all directions and a cut-off of 1.1 nm, with the potential smoothly decreasing to zero at 1.4 nm, was used. Long-range interactions were calculated with the particle-mesh Ewald method (Allen and Tildesley 1989).

RESULTS

Results published previously (Greiner et al. 2012) show the phase co-existence curve for Trilaurin (LLL) and tripalmitin (PPP) along with experimental results for triarachidin (AAA) (Masberg 1999), as depicted in figure 2. Given the structural similarity between PPP and AAA, their similar slopes indicate good agreement between our predicted phase co-existence curves and

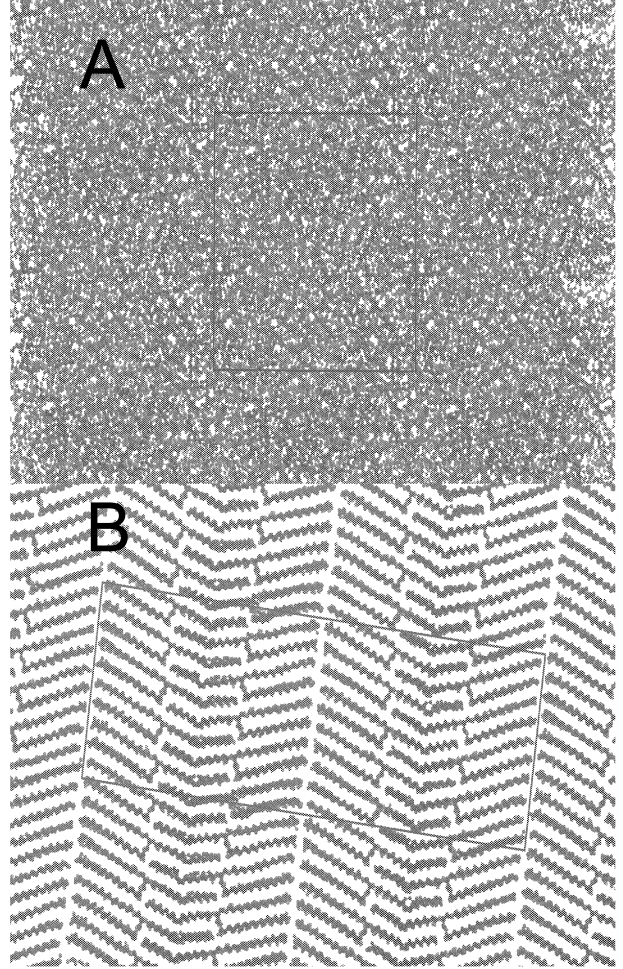


Figure 1: Representation of a liquid (A) and solid (B) simulation box with periodic boundaries containing 160 fat molecules on the example of POS.

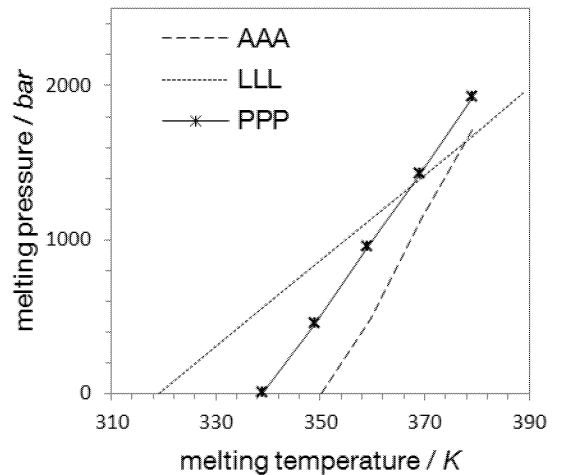


Figure 2: Plots of the phase co-existence lines for saturated fats with references printed as dotted lines.

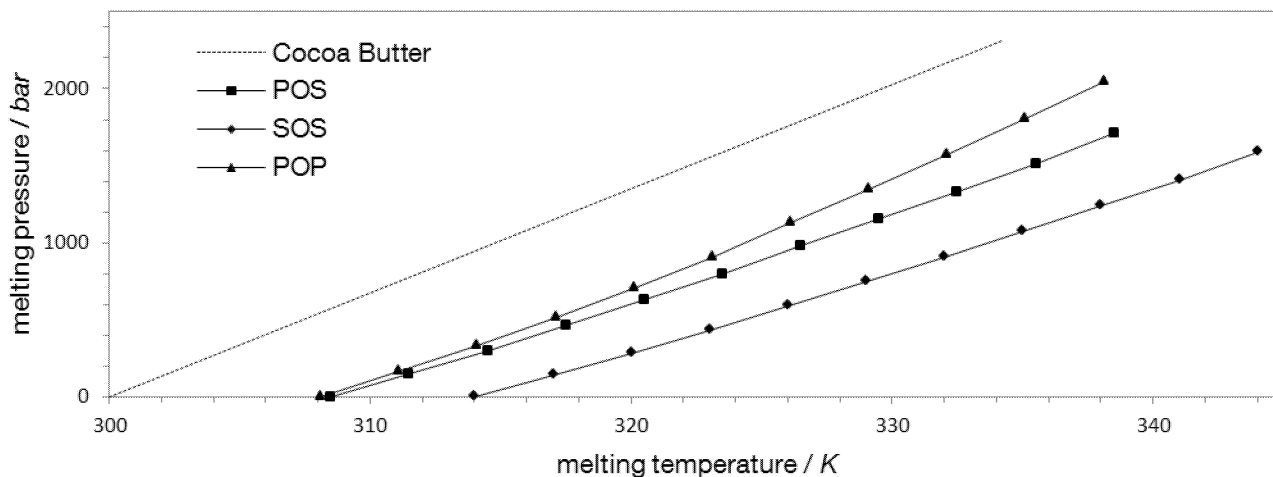


Figure 3: Plots of the slope for unsaturated fats in the predicted phase co-existence diagrams with reference printed as dotted line.

experimental values. The co-existence line for LLL has been estimated by using a single value for ΔV taken from Lee *et al.* (Lee et al. 2010). The smaller slope for LLL, when compared with PPP, indicates a larger volume change for smaller chains. As there is a lack of experimental data for both phase transition diagrams of fats and precise crystal coordinates, we did not calculate further phase co-existence lines for saturated fats. Nevertheless, the results suggest that MD is capable of predicting phase transition diagrams for saturated fats.

Very important for many food products, however, are unsaturated fats. A double bond in the aliphatic chain makes it kink at this very position (see figure 1B), thus largely changing the physical properties of the product. One example where unsaturated fatty acids play an important role is cocoa butter. Roughly 80% of the total fat content comes from POP, POS and SOS. There, one unsaturated oleic acid is attached to the central carbon atom of the glycerol backbone, together with two saturated fatty acids on the outer carbons.

For the implementation in GROMACS we have improved the Gibbs-Duhem integration scheme based on the *Automated Gromacs Simulations*-script by Marc Offmann (URL: <https://github.com/offmarc/AGroS>). Simulations were run fully automated allowing multiple calculations with small integration steps of 3 K.

The phase co-existence lines estimated for POP, POS and SOS are shown in figure 3. The trends for POP, POS and SOS are in reasonable agreement with the reference values for cocoa butter. Given their quantitatively similar molecular structure and liquid behavior, as reported in the literature (Sum et al. 2003), it is

not surprising that the phase co-existence lines show similar slopes. Nevertheless, there seems to be a trend to steeper slopes for components melting at lower temperatures. Due to the small range of pressures explored in experiment, often linear co-existence lines are used to correlate the data. While this simplifies equations for continuum models, the results presented suggest a non-linear behavior when covering large pressure ranges.

A more detailed representation of the slope of the co-existence line for each component is given in figure 4. Results show the described trend of higher slopes towards combinations of higher temperatures and pressures, whereas the slope for cocoa butter, as taken from literature, is constant. Ferstl *et al.* (Ferstl et al. 2010) experimentally determined the phase transition diagram for Triolein and applied a polynomial function to accurately fit their results in a range of 40 K and 4 kbar. For minor changes in the pressure the increasing slope may not be of practical relevance, however in high-pressure treatment, applied pressures can reach values in excess of 15 kbar (Delgado et al. 2008).

CONCLUSION AND OUTLOOK

MD simulations may play an important role in predicting phase transition diagrams. Previously published models (Delgado et al. 2008) show the validity of linear co-existence line estimations for edible fats for pressures as high as 2 kbar. The constant increase of the slope in the pT -diagram would lead to a significant off-set towards higher pressures.

The aim of future calculations will be to explore the

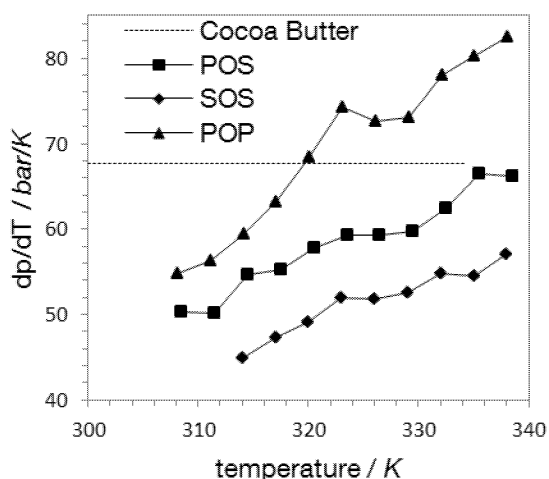


Figure 4: Plots of $\frac{dp}{dT}$ from equation 1 for SOS (diamond), POS (square) and POP (triangle) with reference given for cocoa butter (Yasuda and Mochizuki 1992) (dotted line).

co-existence lines in more detail to further verify the qualitative and quantitative behavior of the given fats, such as comparing the chemical potential between the two phases after every integration step.

ACKNOWLEDGEMENT

This work has been supported by the *Deutsche Forschungsgemeinschaft* (DFG) through grant BR 2035/4-1 and has made use of the computer resources provided by the Leibniz Supercomputing Centre. M.G. gratefully acknowledges the support by the Faculty Graduate Center Weihenstephan of TUM Graduate School at Technische Universität München, Germany. The ScalaLife Competence Center (<http://www.scalalife.eu/>) is also acknowledged for assistance with computing resources and the Gromacs code.

REFERENCES

Allen M.P. and Tildesley D.J., 1989. *Computer Simulation of Liquids*. Oxford University Press Inc., New York.

Chandrasekhar I. and van Gunsteren W.F., 2002. A comparison of the potential energy parameters of aliphatic alkanes: molecular dynamics simulations of triacylglycerols in the alpha phase. *Eur Biophys J Biophys*, 31, no. 2, 89–101.

Delgado A.; Rauh C.; and Benning R., 2008. *Thermodynamisches Modell zum Fest/flüssig-Phasenübergang*

von Substanzen hohen molaren Volumens. *Chemie Ingenieur Technik*, 80, 1185–1192.

Ferstl P.; Eder C.; RußW.; and Wierschem A., 2011. Pressure-induced crystallization of triacylglycerides. *High Pressure Res*, 31, 339–349.

Ferstl P.; Gillig S.; Kaufmann C.; Dürr C.; Eder C.; Wierschem A.; and RußW., 2010. Pressure-induced phase transitions in triacylglycerides. *Ann N Y Acad Sci*, 1189, 62–67.

Greiner M.; Reilly A.; and Briesen H., 2012. Temperature- and pressure-dependent densities, self-diffusion coefficients and phase behavior of monoacid saturated triacylglycerides: towards molecular-level insights into processing. *J Agric Food Chem*, accepted paper to be published soon.

Hess B.; Kutzner C.; van der Spoel D.; and Lindahl E., 2008. *GROMACS 4: Algorithms for highly efficient, load-balanced, and scalable molecular simulation*. *J Chem Theory Comput*, 4, no. 3, 435–447.

Hsu W.D. and Violi A., 2009. Order-disorder phase transformation of triacylglycerols: effect of the structure of the aliphatic chains. *J Phys Chem B*, 113, no. 4, 887–893.

Kofke D.A., 1993a. Direct evaluation of phase coexistence by molecular simulation via integration along the saturation line. *J Chem Phys*, 98, no. 5, 4149–4162.

Kofke D.A., 1993b. Gibbs-Duhem integration: a new method for direct evaluation of phase coexistence by molecular simulation. *Mol Phys*, 78, no. 6, 1331–1336.

Lee Y.L.; Ristic R.I.; DeMatos L.L.; and Martin C.M., 2010. Crystallisation pathways of polymorphic triacylglycerols induced by mechanical energy. *J Phys: Conf Ser*, 247, 1–16.

Masberg S., 1999. *Differentialkalorimetrie (DSC) und Differentialthermoanalyse (DTA) bei hohen Drücken: Untersuchungen zum Phasenverhalten ausgewählter Triacylglycerine, Flüssigkristalle und Anthrachinonfarbstoffe bis 200 MPa*. Ph.D. thesis, Ruhr-Universität Bochum, Fakultät für Chemie und Biochemie.

Sum A.K.; Biddy M.J.; de Pablo J.J.; and Tupy M.J., 2003. Predictive molecular model for the thermodynamic and transport properties of triacylglycerols. *J Phys Chem B*, 107, no. 51, 14443–14451.

Torres J.A. and Velazquez G., 2005. Commercial opportunities and research challenges in the high pressure processing of foods. *J Food Eng*, 67, no. 1-2, 95–112.

Van der Spoel D.; Lindahl E.; Hess B.; Groenhof G.; Mark A.E.; and Berendsen H.J.C., 2005. *GROMACS: Fast, flexible, and free*. *J Comput Chem*, 26, no. 16, 1701–1718.

Yan Z.Y.; Huhn S.D.; Klemann L.P.; and Otterburn M.S., 1994. *Molecular modeling studies of triacylglycerols*. *J Agric Food Chem*, 42, no. 2, 447–452.

Yasuda A. and Mochizuki K., 1992. *High Pressure Res Technol*, 224–225.

AUTHOR'S BIOGRAPHY

MAXIMILIAN GREINER has studied Technology and Biotechnology of Foods at the Technische Universität München from 2006 to 2011. Currently he is working as a PhD student at the chair for process systems engineering in the field of Molecular Dynamics Simulations. While the main focus in the work published here being on foods, he is also highly interested in the molecular dissolution processes of active pharmaceutical ingredients.

EKATERINA ELTS was born in St. Petersburg, Russia. She studied at the Faculty of Physics, St. Petersburg State University, where in 2008 she obtained her PhD in computational physics. Afterwards, in 2011 she received her PhD in Informatics at the Faculty of Informatics, Technische Universität München. Since 2012 she is working as a PostDoc at the chair of process systems engineering in the field of multiscale simulation, combining Molecular Dynamics and Monte Carlo techniques.

HEIKO BRIESEN has graduated in chemical engineering in Karlsruhe and afterwards worked as a PostDoc in the field of crystallization at the RWTH Aachen. After leading the junior research group population dynamics at the Max-Planck Institute in Magdeburg, he now holds the chair for process systems engineering at the Technische Universität München since 2008. His main fields of interest are modeling and simulation of complex processes.

POPULATION BALANCE MODELLING OF FLOCCULATION OF BIOLOGICAL CELLS

André Braun and Heiko Briesen
Chair for Process System Engineering
Technische Universität München
85350 Freising, Germany
email: andre.braun@tum.de

KEYWORDS

Population balance, flocculation, yeast, cells

ABSTRACT

The objective of this work is to model the flocculation process as encountered in many food- and biotechnological applications concerning solid-liquid separation. A population balance framework is used to couple the shear induced aggregation and breakage processes. To solve the population balance model efficiently, the model equations were recasted in moment form, and a 9-th order polynomial closure rule to approximate the missing fractal moments was applied as proposed by Sommer et al. (2006). A parameter study was performed using parameters for yeast flocculation as found in literature. The simulation results are qualitatively in agreement with experimental findings. Furthermore, we show how this model may be used to increase flocculation efficiency by applying a time-dependent shear rate.

INTRODUCTION

Flocculation often occurs in food- and biotechnological applications when dealing with colloidal dispersions (such as biological cells, enzyme granules, or fat globules). In many of these processes, the flocculation is used to facilitate solid-liquid separation. For example, yeast cells are supposed to flocculate towards the end of the fermentation process to improve the filtrability. As has been shown with bottom-fermenting yeast strains (e.g. Annemueller et al. (2005)), the sedimentation speed increases with increasing floc sizes. However, the calculations performed in those studies assumed a statistical mean floc size. To improve the prediction of the sedimentation behavior, those calculations should be performed using a distribution of floc sizes. Therefore, simulations are needed to predict floc size distributions in dependence of their agitation schedule.

One common practice to increase flocculation is agitating the dispersions. The agitation enables shear induced collisions between the particles which are essential for flocs to grow. However, flocs may also break, especially when they increase in size. Thus, flocculation is an inter-

play between aggregation and breakage processes, from which a steady state floc size distribution arises (Han et al. 2003).

A simulation technique allowing to superpose the two opposing processes is the population balance method, where partial differential equations are solved numerically. This technique has already been applied for simulating flocculation of various materials. However, only a few studies have been dealing with biological cells (e.g. Han et al. (2003), van Hamersveld et al. (1998)). Short computational times are necessary when combining the population balance simulations with computational fluid dynamic simulations in order to reproduce the agitation of cells in a complex process in detail. A popular numerical method to reduce computation time is to recast the population balance equations in the moment form. This work adopts the population balance model and the numerical method as described by Sommer et al. (2006). Their model has been successfully applied to describe flocculation of nanoparticles in stirred media mills. We will apply this model to describe the flocculation behavior of yeast cells exposed to shear flow and perform a model parameter study where we use typical model parameters accounting for yeast cells as found in literature. In addition, we will show how such calculations may be used to optimize the shear rate settings of real industrial flocculation processes.

POPULATION BALANCE MODEL IN MOMENT FORM

The population balance equations taking aggregation and breakage into account take the following form (Sommer et al. 2006):

$$\begin{aligned} \frac{dn(v)}{dt} = & \frac{1}{2} \int_0^v \beta(v', v-v')n(v')n(v-v')dv' \\ & - n(v) \int_0^\infty \beta(v', v)n(v')dv' \\ & - \Gamma(v)n(v) + \int_v^\infty \Gamma(v')b(v, v')n(v')dv', \end{aligned} \quad (1)$$

where $n(v, t)$ is the time-dependent number density distribution with the floc volume v as a characterizing variable. β is the aggregation rate kernel, Γ the breakage rate, and b the fragment distribution function. We use the volume v as the characterizing variable since the total volume of all flocs remains constant which allows a simple consistency check.

The first two terms of the right hand side of equation (1) account for the aggregation process. When a floc of size v' collides with a floc of size $v - v'$, they form a new floc of size v . Therefore, the first term is the birth term accounting for the formation of the new floc, whereas the second term is the sink term accounting for the loss of the smaller flocs.

The aggregation rate kernel is a function of the floc volumes since larger flocs are more likely to collide in shear flow than smaller flocs. The turbulent shear-induced aggregation rate kernel has then the extended form of the Saffman-Turner kernel (Saffman and Turner 1956) as given by Sommer et al. (2006):

$$\beta(v, v') = \frac{0.31}{W} G(v^{1/3} + v'^{1/3})^3, \quad (2)$$

where W is the stability factor and G the shear rate. The last two terms of the right hand side of equation (1) account for the breakage process where a floc of size v breaks into two smaller flocs of size v and $v - v'$. The third term is the sink term and the fourth term is the birth term. Both terms depend on the breakage rate Γ , given by:

$$\Gamma(v) = A' G^\mu v^\mu, \quad (3)$$

where A' is a constant, μ a constant exponent, and y a constant inversely proportional to the floc strength (Sommer et al. 2006).

The fragment distribution function $b(v, v')$ is the number density of resulting particles with volume v when a particle with volume v' breaks. In this work, a generalized form of Hill and Ng's power-law breakage distribution is applied (Sommer et al. 2006):

$$b(v, v') = \frac{p v^c (v' - v)^{c+(c+1)(p-2)} [c + (c+1)(p-1)]!}{v'^{pc+p-1} c! [c + (c+1)(p-2)]!}, \quad (4)$$

where p is the number of fragments per breakage event and c determines the shape of the daughter distribution. By using the substitution $z = v/v'$, equation (4) can be written in a self-similar form which now depends on the self similar distribution function $\Phi(z)$:

$$b(v, v') = \frac{p z^c (1-z)^{c+(c+1)(p-2)} [c + (c+1)(p-1)]!}{v' c! [c + (c+1)(p-2)]!} = \frac{\Phi(z)}{v'}. \quad (5)$$

The k -th moment $M_k = \int_0^\infty v^k n(v) dv$ of the distribution $n(v)$ is normalized as follows:

$$m_k = \frac{(\hat{M}_0^\infty)^{k-1}}{M_1^k} M_k, \quad (6)$$

where M_0 is the number concentration and M_1 the volume concentration of the system. \hat{M}_0^∞ is part of the 0-th moment at steady state and can be calculated from

$$\hat{M}_0^\infty = \left(\frac{A' G^\mu (p-1)}{\frac{0.31 G}{W} M_1^{1-\mu}} \right)^{\frac{1}{\mu}}. \quad (7)$$

By multiplying equation (1) with v^k and taking the integral on both sides, the population balance equations can be expressed in the moment form:

$$\begin{aligned} \frac{d}{dt} (\ln(m_k)) = & A' G^\mu (b_k - 1) \frac{m_{k+\mu}}{m_k} \left(\frac{M_1}{\hat{M}_0^\infty} \right)^\mu \\ & + \frac{0.31}{W} G \left(\frac{1}{2} \sum_{s=0}^k \sum_{r=0}^3 \binom{k}{s} \binom{3}{r} \frac{m_{k-s+\frac{3-r}{3}} \cdot m_{s+\frac{r}{3}}}{m_k} M_1 \right. \\ & \left. - \sum_{s=0}^3 \frac{m_{\frac{3-s}{3}} \cdot m_{k+\frac{s}{3}}}{m_k} M_1 \right), \quad (8) \end{aligned}$$

with $k = 1, \dots, 9$ and $b_k = \int_0^1 z^k \Phi(z) dz$ being the k -th moment of the self similar distribution function $\Phi(z)$. In particular, the volume is conserved, i.e. $\frac{d}{dt} (\ln(m_1)) = 0$. In order to solve equation (8) numerically, a closure rule has to be applied to approximate the missing fractal moments. Frenklach and Harris (1987) proposed a 9th order polynomial closure rule to calculate the missing moments m_j as follows:

$$\ln(m_j) = \ln(\gamma_j) - (j-1) \ln(m_0), \quad (9)$$

where $\gamma_j = m_j m_0^{j-1}$ and is calculated from

$$\ln(\gamma_j) = \sum_{k=2}^9 f_k (j^k - j). \quad (10)$$

The coefficient f_k of the k -th order polynomial are found by solving

$$\underline{A}^{-1} \ln(\underline{\gamma}) = \underline{f}, \quad (11)$$

where \underline{A} is a matrix with elements $a_{mk} = m^k$. The moment method has the advantage of a very moderate computational effort.

SIMULATION DETAILS

The ordinary differential equations for the moments are solved numerically using the MATLAB solver ode23tb with a relative error tolerance of 10^{-3} and an absolute error of 10^{-6} . In each time step, the closure rule (equations (9) - (11)) is applied to find the missing fractal moments. The implementation of this model was validated carefully with the results from Sommer et al. (2006).

In our simulation, we use realistic model parameters for yeast as can be found in literature (Han et al. 2003).

The initial moments were calculated from a monodispersed suspension with spherical yeast cells with a diameter of $d_0 = 8 \cdot 10^{-4} \text{ cm}$ and with a cell number of $c_n = 10^6 \text{ \#/ml}$. The other model parameters were chosen as follows: $p = 2$ and $c = 30$ (for binary and uniform breakage), $y = 1.6$, $\mu = 1/3$, $W = 1$, $A' = 0.0047 \text{ cm}^{-1} \text{ s}^{y-1}$, and $G = 100 \text{ s}^{-1}$.

RESULTS AND DISCUSSION

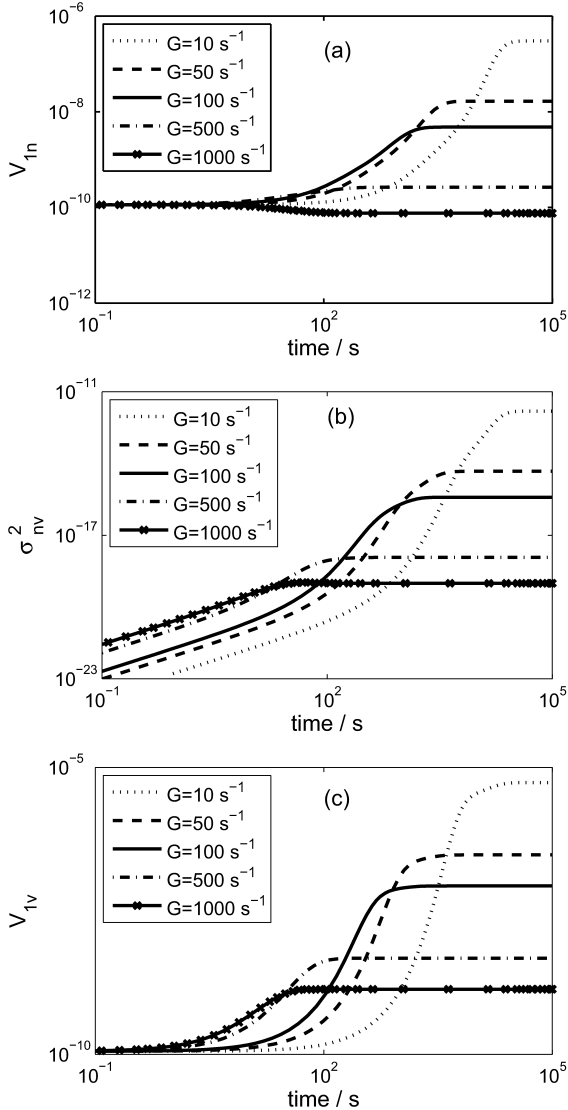


Figure 1: Effect of shear rate on number mean floc size (a), its variance (b), and volume mean floc size (c).

The simulations were performed with the set of model parameters as described above. To perform a parameter study, selected model parameters were varied: the shear rate G accounting for the flow condition, the primary cell size d_0 , the initial number concentration of cells c_n , the stability factor W , and the constant y ac-

counting for cell-cell interactions. The sensitivity of those parameters is studied in terms of the number mean floc size in volume units $V_{1n} = M_1/M_0$, its variance $\sigma_{nv}^2 = M_2/M_0 - V_{1n}^2$, and the volume mean floc size in volume units $V_{1v} = M_2/M_1$.

In figure 1 the influence of the shear rate on those three quantities is shown. With increasing shear rate, the mean floc sizes as well as the variance of the distribution decrease (though the variance is still rather small due to the monodisperse initial distribution). This result is expected since the aggregation kernel is proportional to G whereas the breakage kernel is proportional to G^y , with $y > 1$. Therefore, with increasing shear rate the breakage process becomes dominant compared to the aggregation process.

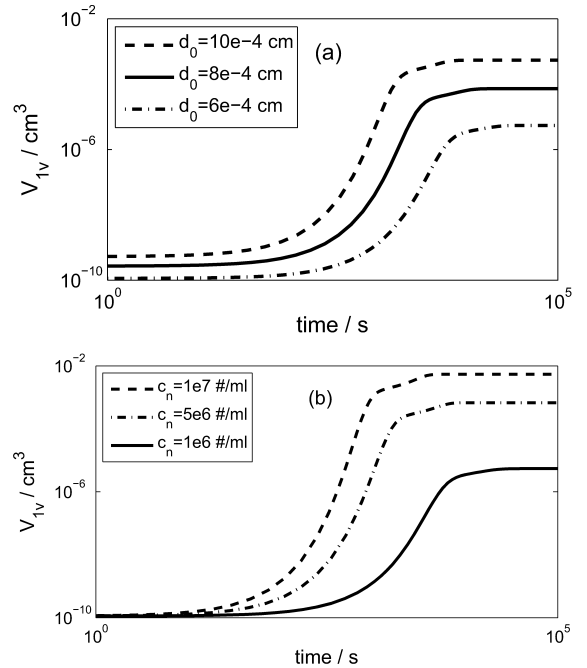


Figure 2: Effect of initial cell diameter (a) and cell number concentration (b) on volume mean floc size.

The influences of the initial cell size and number concentration on the volume mean floc size are shown in figure 2. With increasing cell number or sizes, the collision frequency increases leading to an increase in floc volumes.

Until now, a collision efficiency of unity was assumed, i.e. all cell collisions are effectively forming a new, larger floc. However, this is only the case in the absence of repulsive cell-cell interactions. In the case of repulsive interactions, the collision probability may be reduced by increasing the stability factor W . With an increasing stability factor, the breakage process becomes more dominant and the number cell volume decreases (see figure 3). However, a floc consisting of a single cell cannot break into smaller, undamaged cells. Therefore, when a

single cell gets damaged and lysis occurs, this breakage differs from the breakage of flocs. Such an occurrence should be taken into account in future when modeling the breakage of single cells.

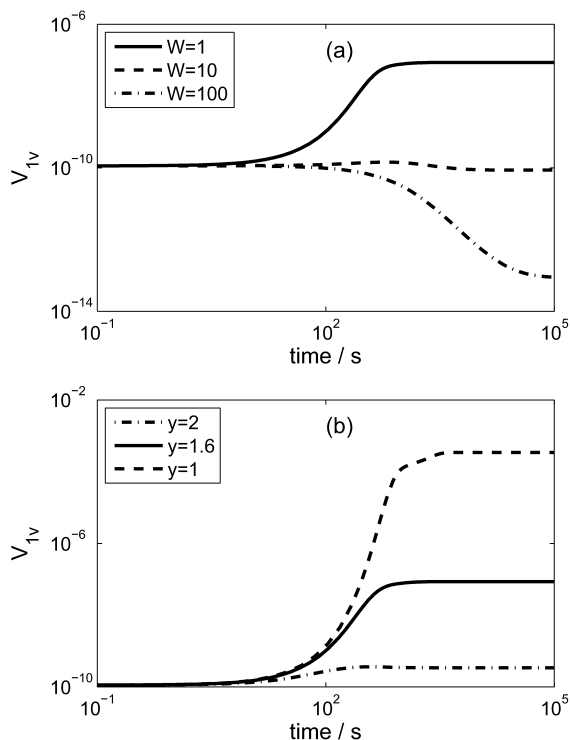


Figure 3: Effect of the stability factor (a) and floc strength (b) on volume mean floc size.

The model parameter y can be seen as inversely proportional to the floc strength. By increasing the floc strength (i.e. decreasing y), breakage is inhibited and the floc volume increases, as shown in figure 3.

Figure 1 clearly shows that the time to reach steady state varies with shear rate (i.e. agitation speed). This behavior may be exploited for a more efficient flocculation process design. Instead of using a constant low shear rate, the fast aggregation behavior for higher shear rates may be utilized for reducing flocculation time scales. In figure 4 we have decreased the shear rate whenever steady state is approached. The final shear rate was $G = 10 \text{ s}^{-1}$. To compare, the mean volume floc size for a constant shear rate with same magnitude was added in this figure. An increase of floc size starts earlier in the process using a time-dependent shear rate and the final steady state was reached sooner. This example shows that the flocculation process may be optimized by designing shear rate trajectories.

CONCLUSION AND OUTLOOK

The population balance model proposed by Sommer et al. (2006) in the context of milling nanoparticles was

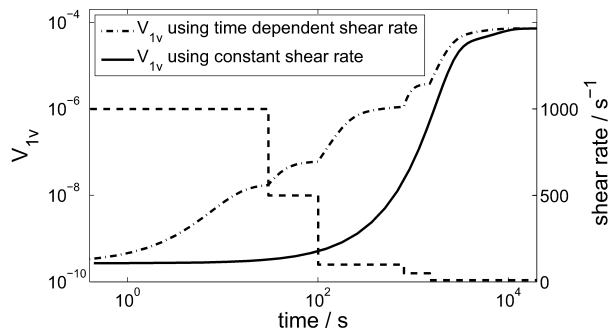


Figure 4: Decrease of flocculation time scale by using time dependent (- -) instead of constant shear rate.

adopted for yeast cells. Realistic model parameters from the literature for yeast cell systems have been used (Han et al. 2003). A parameter study showed that this model yields qualitatively to realistic results (see e.g. Wickramasinghe et al. (2002)). Therefore, the model may be used to optimize the process with model parameters obtained from experiments for a particular situation.

However, as van Hamersveld et al. (1998) discuss in detail, some experimental studies using yeast cells have found that the resulting floc size distribution is rather bimodal due to the presence of single cells originating from surface erosion. This fragmentation behavior was not considered in the given model since a binary and uniform breakage was assumed. Along with avoiding the breakage of single cells, the fragmentation behavior should be included in future models.

REFERENCES

- Annemüller G.; Manger H.; and Lietz P., 2005. *Die Hefe in der Brauerei*. VLB Berlin.
- Frenklach M. and Harris S., 1987. *Aerosol dynamics modeling using the method of moments*. *J Colloid Interface Sci*, 118, no. 1, 252–261.
- Han B.; Akeprathumchai S.; Wickramasinghe S.; and Qian X., 2003. *Flocculation of biological cells: Experiment vs. theory*. *AIChE J*, 49, no. 7, 1687–1701.
- Saffman P. and Turner J., 1956. *On the collision of drops in turbulent clouds*. *Journal Fluid Mech*, 1, no. 1, 16–30.
- Sommer M.; Stenger F.; Peukert W.; and Wagner N., 2006. *Agglomeration and breakage of nanoparticles in stirred media mills - a comparison of different methods and models*. *Chem Eng Sci*, 61, no. 1, 135–148.
- van Hamersveld E.; van der Lans R.; Caulet P.; and Luyben K., 1998. *Modeling brewers' yeast flocculation*. *Biotechnol and bioeng*, 57, no. 3, 330–341.

Wickramasinghe S.; Wu Y.; and Han B., 2002. *Enhanced microfiltration of yeast by flocculation*. *Desalination*, 147, no. 1-3, SI, 25-30.

AUTHOR BIOGRAPHIES

ANDRE BRAUN has graduated in physics at the Swiss Federal Institute of Technology Zurich, where he obtained his PhD in food process engineering in 2009. He is currently working as a PostDoc at the chair of process engineering at the Technische Universität München. His main research interests are rheology and shear sensitivity of biological organisms.

HEIKO BRIESEN has graduated in chemical engineering in Karlsruhe and afterwards worked as a PostDoc in the field of crystallization at the RWTH Aachen. After leading the junior research group population dynamics at the Max-Planck Institute in Magdeburg, he now holds the chair for process systems engineering at the Technische Universität München since 2008. His main fields of interest are modeling and simulation of complex processes.

Towards optimized salt perception: simulation and correlation of salt release during mastication

Georg C. Ganzenmüller[†], Christian Zacherl^{*}, Regina Fischl^{*}

[†] Fraunhofer Institute for High-Speed Dynamics, Ernst-Mach Institut, EMI,
Eckerstrasse 4, 79108 Freiburg, Germany

^{*} Fraunhofer Institute for Process Engineering and Packaging, Giggenhauserstr. 35, 85354 Freising, Germany.
Contact: christian.zacherl@ivv.fraunhofer.de Phone: +49 (0) 8161 491 426

KEYWORDS

Salt perception, salt reduction, numerical simulations

ABSTRACT

We present an approach to a currently relevant challenge in the food industry: The optimization problem of developing a food matrix with maximum salt taste perception and minimum total salt content. A combination of different methodologies is employed in order to identify those food properties, which are most important for salt perception: Laboratory experiments including an artificial mastication machine, numerical simulations, and a panel of human sensorial analysts. The correlations between perceived salt taste and salt content, or salt distribution in the food matrix show a promising potential for the guided design of an optimized, salt reduced food.

1. Introduction

Salt (NaCl) plays an important role in the human nutrition, especially due to its sensorial and flavour enhancing properties.

However, according to epidemiological, migration, intervention, treatment, animal and genetic evidence salt is the primary cause of raised blood pressure (He et al., 2007).

Mean daily salt intake of the European population ranges from approximately 8 – 11 g/day and is well in excess of dietary needs (approximately 3 – 4 g salt/day in adults) (EFSA, 2005). Recent EU legislation allows products which have salt levels below 0.3 % to be labelled as “low salt” and allow claims in relation to sodium intake and heart health to

be made (Commission of the European Communities, 2003).

Discretionary salt (added during cooking and at the table) and naturally occurring sodium in unprocessed foods combined, contribute to 10 – 15 % of total daily intake (FSAI, 2005). The main source of salt in the diet is processed foods (about 70-75 % of the total intake) (James et al., 1987). As relatively moderate restrictions in salt intake have the potential to reduce average blood pressure, reducing salt in processed meat products may substantially reduce the burden of morbidity and mortality from cardiovascular diseases at a population level.

Processed meat products as boiled or raw sausages comprise one of the major sources of sodium in the form of sodium chloride (salt). In those products the salt is, besides its sensorial properties, necessary for technological reasons. Particularly salt is added for conservation, colour, texture, water binding and protein solution. The technologically needed amount is, however, much lower than the amount added because of sensorial reasons. The levels of NaCl in sausages is usually between 1.5 and 4%, the main part of the salt is located in the water phase between the protein gel structure shown in Figure 1 (Kretzschmann, 1996; Franzke, 1990; Gerhardt, 1994).

The overall aim is to reduce the salt content in processed meat products as sausages significantly (<20%) without affecting the sensorial properties.

State-of-the art approaches to reduce salt content via the addition of salt substitutes or salt enhancers have shown only moderate success and are partly not

accepted by the consumers due to the bitter off-flavours induced by the salt substitutes.

Tests indicate that up to 90% of the salt in sausages is swallowed “untasted”, that means that during chewing the sausage the major part of the salt does not dissolve in the saliva and diffuse to the tongue. Other work showed that alternating salt-rich and salt-poor layers inside a food matrix lead to an increased salt perception compared with homogenously distributed salt inside the food matrix (Noort, 2010). There is a lack of knowledge regarding the interactions of the food matrix and texture with the salt release and perception while eating the food.

The approach of this work is to understand the mechanisms of salt release during eating from a food matrix (model food: sausage) to saliva, as well the diffusion to the tongue, which then leads to salt perception.

The knowledge of these mechanisms is expected to contribute to an improved design of the food (sausage) matrix to enhance salt release, availability and consequently perception during food consumption.

In order to design the work in an efficient and target-oriented manner, the experimental design is performed along three parallel directions: (i) human sensorial analytics by a group of specifically trained testing professionals, (ii) laboratory mouth model via an artificial masticator setup, and (iii) numeric simulation of the chewing process and the associated salt release. The work reported here presents the first phase of this project; accordingly we focus on the development and correlation of the mouth model with numeric simulation and sensorial tests. The remainder of this article is organized as follows: part 2 describes our approach of modelling salt perception and release both via laboratory experiments and numerical simulations. Results are presented for both methods and compared with those obtained from a human sensorial analytics board.

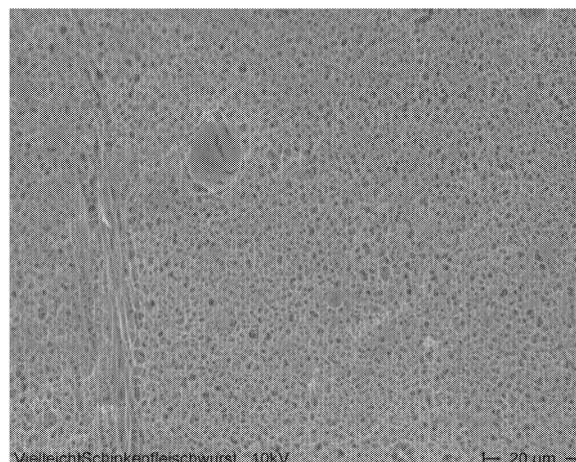


Figure 1: Sausage matrix structure with water located in between the protein network

2. Simulation of Salt Perception and Correlation with Human-Sensorial Analytics

In this section, we describe the experiments used to correlate salt content in the food with actual salt perception by a group of human test subjects.

2. 1. Laboratory Experiments

An artificial masticator is employed to act as „mouth model system“ in order to simulate, monitor, and analyze the chewing process of food with *in situ* analysis of the salt release out of the food matrix. A defined sample of the food matrix (sausage) is placed in a cylindrical beaker, which is turned during the experiment after each chewing cycle by 90° in order to mimic the movement of the food induced by the tongue. A cylindrical indenter, mimicking the destructive effect of the teeth is moved by a texture analyser at defined speed and frequency, based on human-physiological parameters. Prior to the mastication simulation artificial saliva is dosed to the system. The release and diffusion of salt from the food matrix to the saliva is measured by a conductivity electrode. The experiments are carried out at a temperature of 37°C. A draft of the experimental setup is shown in Figure 2.

Sausage matrices with different concentrations of salt (between 1.0 % and 2.40 %) are analysed by the artificial masticator, results are shown in Figure 3. It is evident that the salt release during mastication is

dependent on the initial salt concentration in the food matrix.

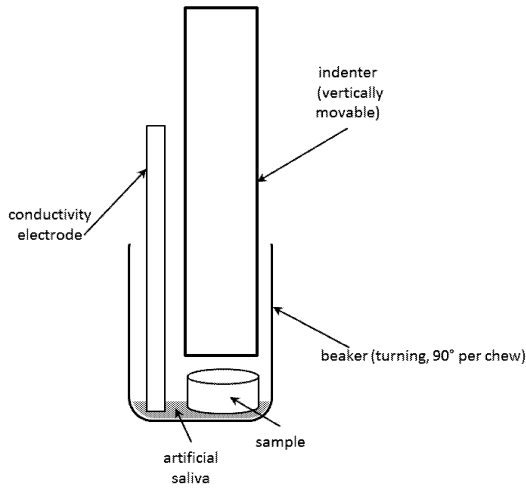


Figure 2: artificial masticator setup

In addition to the experiments with the masticator, the samples are also analysed by a sensorial panel. The aim is to describe and quantify the salty taste of the different sausages.

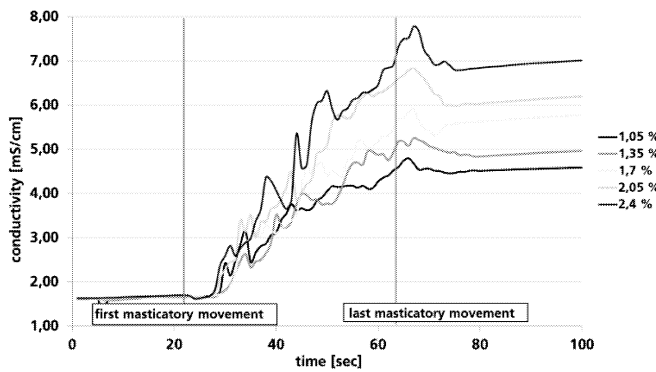


Figure 3: salt release from different sausage matrices analysed by the artificial masticator

2. 2. Numerical Simulations

In order to understand the mechanisms as to how salt is released from the food bolus into saliva, a new numerical approach for the chewing process was developed. The main requirements for such a computer simulation program are as follows.

- The ability to model both solid, visco-plastic/elastic materials with shear strength as well as fluids.

- Tolerance to severe deformations and mixing of solid and fluid materials.
- The ability to describe salt transport from food into saliva, both via diffusive and convective mechanisms.

These requirements are difficult, if not impossible to handle with commercially available Engineering simulation software. In order to amend this situation, we resorted to developing our own simulation software, which is based on a mesh-free continuum-mechanics method, Smooth Particle Hydrodynamics (SPH) (Lucy, 1977; Gingold and Monaghan, 1997). Meshfree methods are preferred over the traditional Engineering approaches, which are typically based on Finite-Element or Finite Volume methods, as these rely on an explicit mesh representation of the material to be simulated. The mesh itself is typically not compatible with severe distortions and therefore cannot handle the large deformations encountered during the chewing process. In contrast, SPH does not require a mesh and is well suited for complex, mixed fluid and solid flows. All that is needed is a discretization of the material into integration nodes. To this end, the initial artificial masticator geometry introduced above is represented by the points of an alpha-FCC close-packed lattice with lattice constant 1 mm.

We model the food material as a viscous body with shear strength. Its resistance to compression (i.e., pressure p) is described with Tait's equation of state,

$$p(\rho) = \frac{K}{7} \left[\left(\frac{\rho}{\rho_0} \right)^7 - 1 \right].$$

Here, p is pressure, ρ and ρ_0 are the current and equilibrium mass densities, and K is the bulk modulus. These quantities have been chosen to represent those of water. Shear strength is realized through the introduction of explicit linear springs between neighboring integration nodes. The spring constant is adjusted such that the force-displacement curve of a uniaxial compression test of a food specimen is reproduced. As well as providing shear strength, the springs also serve as the failure mechanism which allows the food material to be split into smaller entities as chewing progresses. This is realized by describing a maximum spring elongation,

beyond which the spring fails irreversibly. This maximum elongation is again parameterized using the failure response of the food material. Saliva is modeled with Tait's equation of state and the bulk modulus of water. In order to describe salt diffusion from the food material into saliva, we use the diffusion equation, which is also discretized with the SPH formalism. Note that, in order to achieve a realistic transport of salt into saliva, the effective diffusion coefficient is proportional to the damage parameter (the ratio of failed springs over the initial number of springs) of an integration node. This affects salt transport only between those parts of the food which have been partially disintegrated via the chewing motion, and saliva. Table 1 summarizes the simulation parameters used here.

Table 1: simulation parameters

simulation parameter	value
bulk modulus of water	$K = 2.2 \text{ GPa}$
spring constant	$k = 2.25 \times 10^{-3} \text{ N}$
max. relative spring elong.	$S = 0.61$

Simulations performed with this numerical model result in good agreement with experimental data. Figure 4 shows the stress-displacement curve for uniaxial compression of a food specimen, and the corresponding simulated response. Note that the complex failure at high compression is well reproduced using our conceptually straightforward damage criterion.

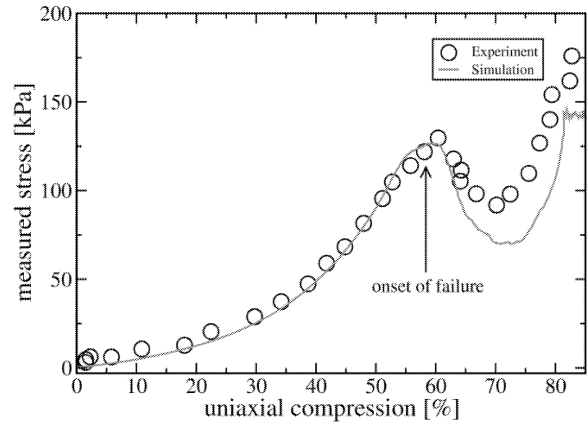


Figure 4: comparison of stress response between simulation and experiment. Shown is data for uniaxial compression of a cylindrical (height 2 cm, diameter 4 cm) food specimen (fat reduced sausage).

Using the parameters as detailed above, we simulate a complete run of the artificial mastication process with 14 successive chewing motions. The complex flow and damage response, as well as the salt diffusion into saliva is visualized in Figure 5. Based on this simulation, the concentration of salt in saliva and food damage parameter is plotted versus the number of chewing cycles, see Figure 6. Note that no physical units are given for the salt concentration, as a dimensionless salt diffusion coefficient has been assumed as the determination of a physical diffusion coefficient is ongoing work performed by us. Regardless of this issue, the results very clearly demonstrates that our model captures the expected physical behavior of the mastication process, with the amount of salt transferred from the food specimen to saliva being directly related to the chewing motion.

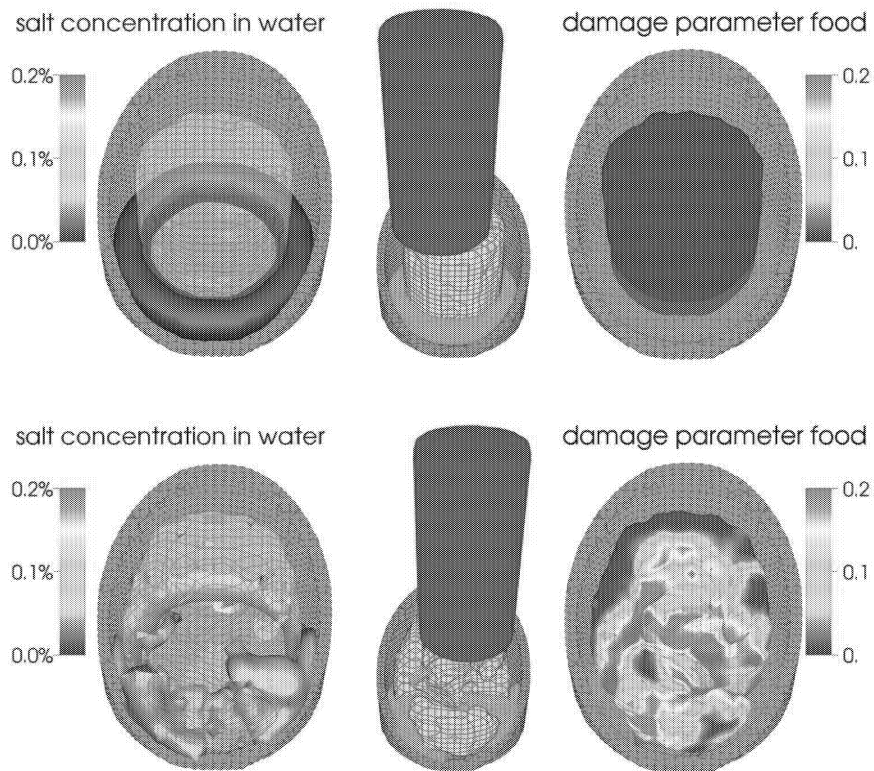


Figure 5: numerical simulation of artificial mastication process. Top row: The centered image shows the initial configuration, with a cut view through the container (gray), saliva (blue), food material (yellow), and impactor (lilac). The left and right figures show a color-coding of salt content in water and food damage parameter, respectively. Bottom row: these images show the simulation after two chewing motions. A considerable amount of salt has been released into saliva, the food specimen shows considerable damage, and food and saliva are mixed.

2.3 Correlation with human salt perception

The different sausage products with varying concentrations of salt were analyzed by a trained sensorial panel regarding the salt intensity during the chewing process according to DIN 10966:1997-12. The perceived salt intensity was scaled between 0 (no perception) until 10 (high salt intension) and plotted over the time during chewing and swallowing. In Figure 7 the results of the sensorial analyses of different sausages with varying salt concentration between 1.0% and 2.4% are shown. The maximal salt intensity as well as the increase of saltiness before swallowing correlate with the concentration of salt in the sausage matrix.

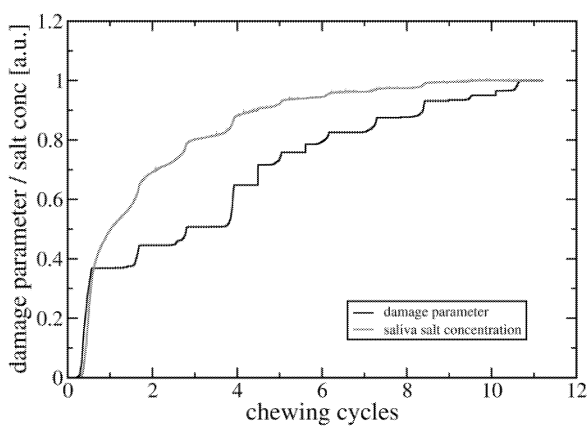


Figure 6: correlation of salt concentration in saliva with total damage of food specimen. Note that the ordinate has been rescaled.

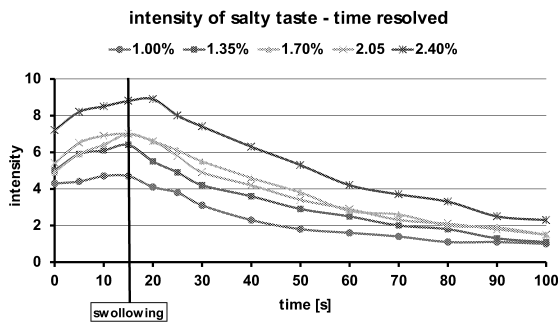


Figure 7: Salt intensity of sausages with different salt concentrations between 1.0% and 2.4% plotted over the mastication and swallowing time analyzed by a sensorial panel

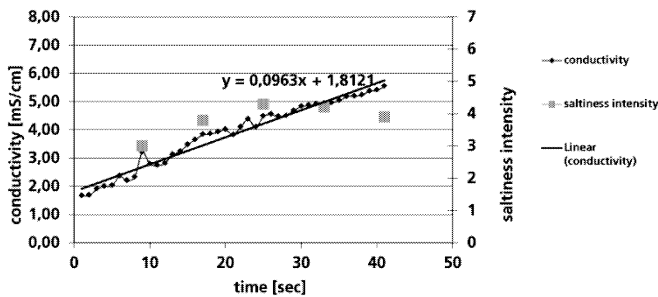


Figure 8: Dynamic increase of salt intensity of sausages (1.4 % salt content) during mastication at sensorial panel (large squares, violet) and conductivity measured during artificial mastication (small squares, blue)

In Figure 8 the results of the artificial mastication and the time-dependent salt perception of the sensorial panel are shown. The results indicate that there is in a specific range a correlation between both analytic tools. At longer times the saltiness measured by the sensorial panel shows a slight plateau or even a decrease, while the conductivity measured via artificial masticator increases still linear. This difference may be caused by the non-linear dynamic salt perception by the human salt receptor cells, which tend to get accustomed by longer constant salt stimulus (McCaughey 2007).

3. Discussion

This work presents an approach to a currently relevant challenge in the food industry: The optimization problem of developing a food matrix with maximum salt taste perception and minimal total salt content.

Our approach to this problem is threefold: we combine laboratory experiments of food mastication with numerical simulation, and compare the predictions of these methods with a board of trained human sensorial analysts. We have developed both an artificial food masticator and a simulation code. These tools provide us with quantitative data on the salt release as a function of the number cycles. Initial experiments show good correlation between these methods and the human sensorial panel for the food model system used (sausage). Thus, we have established systems which can rapidly evaluate an approximate degree of salt taste for different food matrix specimens in a simple laboratory experiment, decreasing the need for lengthy and costly human sensorial analytics. On the other hand, the detailed information available from the numerical simulations can direct the development of the food matrix into successful direction. For example, the optimal degree of locally varying salt concentration can first be predicted using the simulation code, before a laboratory trial is conducted.

4. References

McCaughey, S., (2007), in *Reducing salt in foods* D. Kilcast, F. Angus, Eds. Woodhead Publishing, pp. 18-46.

He, F.J. and MacGregor, G.A. (2007), in *Reducing salt in foods* D. Kilcast, F. Angus, Eds. Woodhead Publishing, pp. 18-46.

EFSA, (2005). Opinion of the Scientific Panel on Dietetic Products, Nutrition and Allergies on a request from the Commission related to the Tolerable Upper Intake Level of Sodium. The EFSA Journal 209, 1-26.

Commission of the European Communities, (2003). Proposal for a Regulation of the European Parliament and of the Council on Nutrition and Health Claims made on Foods. COM 424 final.

- FSAI, (2005), "Salt and Health: Review of the Scientific Evidence and Recommendations for Public Policy in Ireland" Food Safety Authority of Ireland.
- James, W. P., Ralph, A. and Sanchez Castillo, C. P., (1987). The dominance of salt in manufactured food in the sodium intake of affluent societies. *Lancet* 8530, 426-429.
- Kretzschmann, F, (1996). Nichtoriginäre Stoffe in Fleisch und Fleischerzeugnissen, In: *Fleischtechnologie*, Behrs Verlag Hamburg. Pp. 167-179.
- Franzke, C (1990). *Lehrbuch der Lebensmittelchemie*, Band 1: *Lebensmittelinhaltsstoffe*, Akademie-Verlag Berlin.
- Gerhardt, U (1994). Zutaten und Zusatzstoffe für die Herstellung von schnittfester und streichfähiger Rohwurst. In: *1. Stuttgarter Rohwurstforum*, Stuttgart Pp. 99-114.
- Noort, M.W.J., et al. (2010), Saltiness enhancement in bread by inhomogeneous spatial distribution of sodium chloride. *Journal of Cereal Science*, 1-9.
- Lucy, L. B., (1997), „A Numerical Approach to the Testing of the Fission Hypothesis”, *The Astronomical Journal* 82, 1013-1024.
- Gingold, R. A., and Monaghan, J. J. (1997), “Smoothed Particle Hydrodynamics: Theory and Applications to Nonspherical Stars”, *Monthly Notices of the Royal Astronomical Society* 181, 375-389.
- Tait, P. G. (1888), “Physics and Chemistry of the Voyage of H.M.S. Challenger”, Vol. 11, Part IV, S.P. LXI.

SIMULATION IN FOOD PROCESSING

SIMULATION MODEL DESIGN AND ASSESSMENT OF NANOPARTICLE MIGRATION FROM A NANOCOMPOSITE WITH EXPERIMENTAL VALIDATION

Maeve Cushen, Enda Cummins
School of Biosystems Engineering, Agriculture and Food Science Centre, University College Dublin, Belfield,
Dublin 4, Ireland
E-mail: maeve.cushen@ucd.ie

KEYWORDS

Nanocomposite, migration, model validation

ABSTRACT

Silver nanoparticles (nanosilver) that exhibit antimicrobial activity have been incorporated into polymers to create antimicrobial packaging materials. Their use in conjunction with food has caused concerns regarding the risk of migration. This could increase human exposure to nanoparticles. A migration model was developed based on relationships defining migratability and subsequent migratables and uses the Williams-Landel-Ferry equation. Input parameters were based on observed data in experimental migration tests and data available from literature. The migration of nanosilver from low density polyethylene (PE) nanocomposites at 4 storage conditions was modelled with mean migration ranging from 3.12×10^{-3} to 6.63×10^{-3} mg/dm². A parallel validation study was used to validate model migration predictions.

INTRODUCTION

Many new technological applications have emerged based on the novel behaviours exhibited by some materials at the nanoscale (materials that have a particle size between 1-100 nm). The collective term used to describe these applications is nanotechnologies and the food industry, among other industries, is likely to benefit from them. An area within the food industry that nanotechnologies have shown promise is advancements in food packaging materials (Cushen et al. 2012a). Nanosilver shows unique antimicrobial behaviour and so has been incorporated into commercially available food packaging matrices; nanocomposites, which are designed to exploit the novel properties of their respective nanocomponent. Some nanomaterials are not permitted in the EU due to limited toxicity research results.

Simulation models can be a valuable resource in risk assessment, particularly in migration and exposure assessments.

MATERIALS AND METHODS

Mathematical Model

A simulation model was designed using equations defining migratability and subsequent migratables of the nanocomposite/food system. The Williams-Landel-Ferry equation was used with the dynamic viscosity of the polymer to obtain the viscosity at the glass transition temperature of the polymer, as in Simon et al. (2008). It is defined as

$$\eta(T_g) = \frac{\eta(T)}{\left(\exp^{\left(\frac{-1(c_1(T-T_g))}{(c_2+T-T_g)} \right)} \right)} \quad (1)$$

where $\eta(T_g)$ is the viscosity at the glass transition temperature, $\eta(T)$ is the viscosity at the experimental temperature as mentioned above, in this case, the dynamic viscosity information of the polymer was used. C_1 and C_2 are constants with values of 17.44 K and 51.6 K respectively. The Williams Landel Ferry equation is also used for the subsequent calculation of the viscosity at a particular temperature, during validation, experimental temperatures were used as inputs.

$$\eta(T) = \eta(T_g) * \exp^{\left(\frac{-1(c_1(T-T_g))}{(c_2+T-T_g)} \right)} \quad (2)$$

Migratability (M), is a value of the likelihood of particles migrating from a given system is defined as

$$M = \left(\frac{k_B T t}{24(\pi^2) \eta r} \right) \quad (3)$$

where k_B is the Boltzmann constant ($k_B = 1.3807 \times 10^{-23}$ J.K⁻¹), t is time in seconds and r is the radius of the particles. Migratables (N) is the quantity of nanoparticles migrating from the polymer matrix.

$$N = M a c \quad (4)$$

Where a is area of the nanocomposite-food interface and c is the initial concentration of nanoparticles in the nanocomposite.

A Monte-Carlo simulation model was used so that inherent variability of the input parameters was taken

into consideration (Table 1). @RISK software (Palisade, UK), a package specifically used for risk assessment, was used as an *add in* in Microsoft Excel. The inputs, constants and outputs of the model are shown in Table 1.

Table 1: Inputs, Constants and Outputs of the Simulation Model

	Name	Subdivision	Value	Unit	Symbol	Eq ⁿ	Reference
Inputs							
PE	Dynamic viscosity	Viscosity	Uniform(1263*,10000)	Pa.s	$\eta(p)$	-	Ghaneh-Fard et al. (1996)
		Temperature	Uniform(423,453)	K	x	-	Faghihl et al. (2002), Ghaneh-Fard et al. (1996)
	Glass transition temperature		Triangular(143,173,193)	K	T_g	-	Web reference 1, Šimon et al. (2008), Web reference 2
	Density		921	kg/m ³	$\rho(p)$	-	Product specification
Nano-particle	Density		10490	kg/m ³	$\rho(n)$	-	Ghander et al. (2007)
	Diameter		Logistic(1.01×10^{-8} , 6.4×10^{-10})	M	$2r$	-	Measured value (mv)
Storage	Time (there were two levels of this factor)	1.1 days :	95040	seconds	t	-	mv
		3.1 days:	267840				
	Temperature (there were two levels of this factor)	T1	Logistic(281.04,0.16)	K	T	-	mv
		T2	Logistic(294.86,0.31)				
System	Surface area		Uniform(0.0099,0.0101)	m ²	a	-	mv
	Conc. of nanoparticles in PE		**	kg/m ³	c	-	mv
Constants							
	Pi		22/7	-	π	-	
	Boltzmann constant		1.3087×10^{-23}	J.K ⁻¹	k_B	-	Šimon et al. (2008)
	Empirical parameter		17.44	K	C_1	-	Šimon et al. (2008)
	Empirical parameter		51.6	K	C_2	-	Šimon et al. (2008)
Outputs							
	Viscosity at the glass transition temperature		Distribution with a mean of 1.27×10^{10} and σ of 5.9×10^9	Pa.s	$\eta(T_g)$	[1]	
	Temperature dependence of viscosity		Distribution with a mean of 8.9×10^4 and σ of 4.8×10^4	$d\eta/dT$	$\eta(T)$	[2]	
	Migratability		Specific to the levels of the factors: t and T	-	M	[3]	
	Migratables		Specific to the value of M and c and thus the factor $\rho(n)$	Mg	N	[4]	

*calculated from data reported in Ghaneh-Fard et al. (1996) and Faghihl et al. (2008) using the equation for complex viscosity of polymers (Web reference 3).

**see table 2.

σ : standard deviation of the distribution

Model Validation

Experimental Procedure

PE nanocomposites were designed which incorporated silver nanoparticles, radii of 25 nm, at 0.5% w/w. Skinless, boneless chicken breasts (samples) were sourced from an Irish supplier and wrapped in 120 cm² of one of the prepared nanocomposites on the breast bone side of the chicken. Aluminium foil was wrapped around these to eliminate any possible variation that light may impart (Cruz et al. 2008).

Each sample, nanocomposite, foiled (unit) was then vacuum packed to ensure maximum contact between the active nanocomposite and the chicken. For such active packaging materials, sharing a common interface or physical contact with the food surface is essential for the desired effect to be observed (Vermeiren et al. 2002). Each unit was done in quadruplicate. Two control samples were prepared for each storage condition tested.

Units were kept in constant temperature rooms for the duration of the experiment; either 1.1 days or 3.1 days. Temperature probes were used to log the internal temperatures of the samples at the various temperature levels. This period allowed for the nanosilver in the nanocomposites to migrate into the samples.

All packaging was removed from the samples and Inductively Coupled Plasma Mass Spectroscopy (ICPMS) analysis was used to quantify silver in the samples. Samples were analysed according to the protocol assigned the ISO number: DIN EN ISO 17294-2-E29.

Model-Experimental Synchronization

The conditions of the experiment were used as inputs in the model. This allowed for the direct comparison of the model outputs with the experimental results. The input variable of concentration was converted from % w/w (given in experimental procedure above) to kg/m³ as required by the model (Table 2).

Table 2: Inputs and outputs of the model of nanosilver concentration in the Nanocomposite

	Value	Symbol	Unit	Equation
Inputs				
Quantity of PE in nanocomposite	Triangular(99.48, 99.5, 99.52)	b	% w/w	
Quantity of Silver in nanocomposite	Triangular(0.48,0.5,0.52)	d	% w/w	
PE Density	921	$\rho(p)$	kg/m ³	
Silver density	10490	$\rho(n)$	kg/m ³	
Outputs				
Volume of PE	Distribution with a mean of 1.08×10^{-3} and σ of 8.86×10^{-8}	f	m ³	$b/\rho(p)$
Volume of silver	Distribution with a mean of 4.76×10^{-7} and σ of 7.78×10^{-9}	g	m ³	$d/\rho(n)$
Volume of 1 kg of nanocomposite	Distribution with a mean of 1.08×10^{-3} and σ of 8.09×10^{-8}	h	m ³	$f+g$
Weight of 1 m ³ of nanocomposite	Distribution with a mean of 925 and σ of 0.07	j	kg/m ³	$1/h$
Weight of nanocomponent in 1 m ³ of nanocomposite	Distribution with a mean of 1.53×10^{-5} and σ of 1.45×10^{-6}	c	kg/m ³	$j \times d$

RESULTS

Experimental Migration

The mean of the control samples for each storage condition was subtracted from each replicate result in that storage condition. The mean and standard deviation of the 4 replicates (after control samples were taken into consideration) were calculated for each storage condition. Control chicken samples' silver quantities had a mean of 0.008 mg/kg and a standard deviation of 0.001 mg/kg, this may be due to test sensitivity and background noise.

It should be noted that the levels of migration observed in this study are from a pilot bench scale nanocomposite composed in a laboratory for experimental uses only. Commercially, it would be unlikely that nanocomposites containing 5% w/w fill of nanosilver would be produced because novel effects are observed at much lower levels; less than 10% of the nanocomponents incorporated into the nanocomposites described in this study and the *law of diminishing returns* applies (Cruz-Romero et al. 2012). This is particularly important as the level of nanoparticulate fill was identified as the most significant parameter influencing migration compared to other parameters of time, temperature and

nanoparticle size in a recent study (Cushen et al. 2012b).

The two levels of temperatures set and logged over the course of the laboratory based experiment (and also used as input distributions in the simulation model) are both above the recommended storage temperature of a perishable food product ($> 5^{\circ}\text{C}$); the means of the temperature distributions, T1 and T2, were 8.14°C and 21.87°C respectively. This is an important consideration when comparing the migration of nanosilver in this study to other studies or ingestion limits. This study assesses the migration in a nanocomposite – food system, not only from nanocomposites with a high nanoparticle fill level but at relatively high temperatures. Hence the study represents a pessimistic evaluation of potential commercial use.

Model

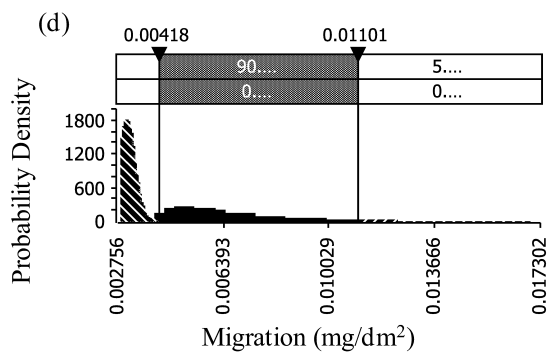
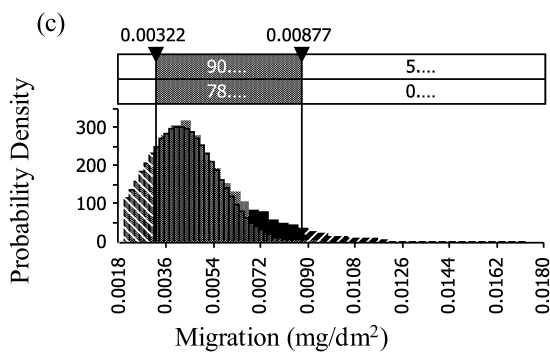
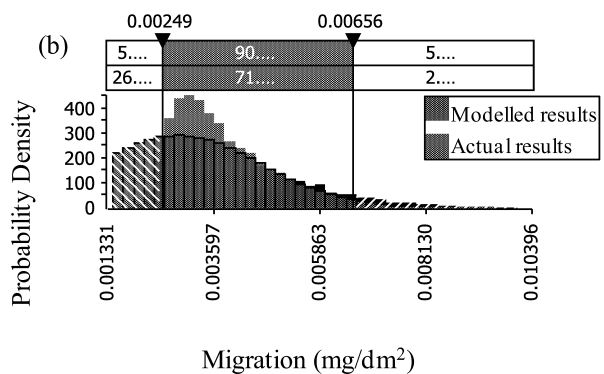
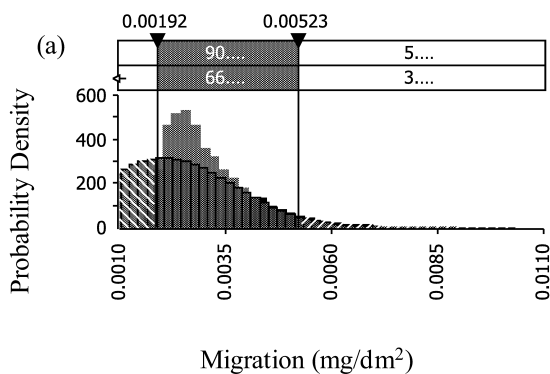


Figure 1: Model predictions for the migration of nanosilver from PE nanocomposites compared to experimental migration results at (a) Time 1.1 days, Temperature T1 (b) Time 1.1 days, Temperature T2 (c) Time 3.1 days, Temperature T1 (d) Time 3.1 days, Temperature T2

In the case where a migration simulation model was being used for a commercial food packaging material, the underestimation of migration would be a greater cause for concern in a migration simulation model than an overestimation. In general, if there is any

The predicted migration values increased with time and temperature, this trend corresponds to results in Šimon et al (2008) where a broader temperature range and longer time periods were studied.

Model Validation

It is shown in Figure 1 that the model proved to be reliable in predicting the migration results for nanosilver over a range of storage conditions. The model overestimated the result in all storage conditions tested. However, for the storage time of 3.1 days at temperature T2, the model overestimated the result to a greater extent, thus the prediction had a larger margin of error than the other storage conditions tested (Table 3). The reason for this is unclear and requires further investigation. It is noted that for the other cases (Figure 1. a – c), the model slightly overestimates migration. However, in all cases, the model predictions lie within the range of the experimental results.

margin for error in simulating models, the model should overestimate migration rather than underestimating it (Helmroth et al., 2002). This is to ensure the toxicological safety of the material and to protect consumers.

Table 3: Accuracy of Migration Model Predictions for Nanosilver from PE Nanocomposites over the Range of Experimental Storage Conditions

Time (days)	Temperature	Modelled mean, st. Dev.	Experimental mean, st. Dev.	% Error
1.1	T1	2.3×10^{-3} , 1.4×10^{-4}	2.1×10^{-3} , 1.6×10^{-3}	15.27
3.1	T1	2.9×10^{-3} , 1.7×10^{-4}	2.8×10^{-3} , 1.7×10^{-3}	21.43
1.1	T2	3.85×10^{-3} , 2.3×10^{-4}	4.1×10^{-3} , 1.4×10^{-3}	13.17
3.1	T2	4.9×10^{-3} , 2.9×10^{-4}	3.1×10^{-3} , 3×10^{-4}	108.88

CONCLUSION

Migration occurred in the nanosilver PE nanocomposite – chicken system with mean migration ranging from 8.0×10^{-4} to 5.4×10^{-3} mg/dm². The model distributions had mean values ranging from 3.12×10^{-3} to 6.63×10^{-3} mg/dm². The validation stage confirmed that model predictions were within the measured range. The model outlined in this paper requires a review of all input parameters to ensure all variability is accounted for. Inputs tend to err on the side of caution, which is particularly important to consider when considering consumer exposure and hence safety.

Before this simulation model is used in an exposure assessment, it must undergo further validation so discrepancies may be reduced and the overall accuracy improved.

REFERENCES

- Cruz, J. M., Sanches Silva, A., Sendón García, R., Franz, R., and Paseiro Losada, P. 2008 “Studies of mass transport of model chemicals from packaging into and within cheeses.” *Journal of Food Engineering*, 87(1), 107-115.
- Cruz-Romero, M., Kerry, J., and Morris, M. 2012. “Antimicrobial properties and mechanical durability of nanopolymer films.” *personal communication*.
- Cushen, M., Kerry, J., Morris, M., Cruz-Romero, M., and Cummins, E. 2012a. “Nanotechnologies in the food industry - Recent developments, risks and regulation.” *Trends in Food Science & Technology*, 24(1), 30-46.
- Cushen, M., Kerry, J., Morris, M., Cruz-Romero, M., and Cummins, E. 2012b. “Migration and exposure assessment of silver nanoparticles from a PVC nanocomposite.” *unpublished work*.
- Faghihi, F., Morshedjan, J., Razavi-Nouri, M., & Ehsani, M. (2008). Dynamic Rheological and Mechanical Behaviours of Poly(dimethylsiloxane)/Low Density Polyethylene Immiscible Blends: Interfacial Modification via Reactive Blending. *Iranian Polymer Journal*, 17(10), 755-765.
- Ghaneh-Fard, A., Carreau, P. J., & Lafleur, P. G. (1996). Study of instabilities in film blowing. *AIChE Journal*, 42(5), 1388-1396.

- Šimon, P., Chaudhry, Q., and Bakos, D. 2008. “Migration of engineered nanoparticles from polymer packaging to food - a physicochemical view.” *Journal of Food and Nutritional Research*. 47(3), 105-113.
- Vermeiren, L., Devlieghere, F., and Debevere, J. 2002. “Effectiveness of some recent antimicrobial packaging concepts.” *Food Additives & Contaminants: Part A: Chemistry, Analysis, Control, Exposure & Risk Assessment*, 19(4 supp 1), 163 – 171.
- Helmroth, E., Rijk, R., Dekker, M., & Jongen, W. (2002). Predictive modelling of migration from packaging materials into food products for regulatory purposes. *Trends in Food Science & Technology*, 13(3), 102-109.

WEB REFERENCES

1. <http://www.plasticmoulding.ca/polymers/polyethylene.htm>,
2. http://www.polyesterconverters.com/pcl_apps/stage1/stage2/applications_and_enduses/polyethene.htm
3. <http://composite.about.com/library/glossary/c/bld-ef-c6199.htm>

Computational Fluid Dynamics (CFD) modelling of the fluidised bed coating process

Frederik Ronsse^a,
Wasan Duangkhamchan^a
Koen Dewettinck^b
Jan G. Pieters^a

^aBiosystems Engineering, ^bFood Technology & Engineering
Ghent University
Coupure Links 653
B-9000 Ghent, Belgium
E-mail: Frederik.Ronsse@UGent.be

KEYWORDS

Fluidisation, Mass transfer, Heat transfer, Simulation, CFD.

ABSTRACT

A multiphase Eulerian Computational Fluid Dynamics (CFD) model was developed to simulate the batch fluidised bed coating process. Model development is described using stepwise addition: First, a gas-solid 2- and 4-phase Eulerian model was used to evaluate the appropriate selection of the drag model. Next, the effect of the pneumatic nozzle – used to atomize the coating solution – on the gas/solid fluidisation behaviour was described. A third step dealt with the inclusion of the liquid phase (coating solution) dispersion in the reactor, using appropriate atomizer models in a Lagrangian extension to the CFD model. Finally, the overall CFD fluidised bed coating model, complemented with the heat and mass transfer equations to account for particle heating and droplet evaporation phenomena was presented. Comparison and evaluation between time-averaged solids volume fractions obtained from experiments and from simulations was made using experimental data of Depypere *et al.* (2009).

INTRODUCTION

Fluidised bed coating is a process in which a particulate solid (i.e. core) material is encapsulated by spraying a coating polymer directly into a fluidised bed. The aim of coating particulates is to control their dissolution behaviour (release control), to protect the core ingredients, to increase the overall product quality or to increase the processing convenience (Depypere *et al.*, 2003).

An aqueous or organic solvent-based solution containing the coating polymer is continuously sprayed by means of a pneumatic or binary nozzle, which may be submerged in or positioned above the bed (Ronsse *et al.*, 2007a,b; Depypere *et al.*, 2009). In top-spray configuration (Figure 1), regarded as the most appropriate method for food ingredient applications, binary nozzles are positioned above the bed, producing droplets with a size ranging from 10 to 40 μm (Guignon *et al.*, 2002). Due to the complex thermodynamic interactions between the droplet phase, the particles and the gas phase, the coating process is prone to unwanted yield-reducing or quality-degrading side effects, such as

agglomeration, premature droplet evaporation, attrition of friable and degradation of heat-sensitive core or coating materials (Guignon *et al.*, 2002; Ronsse *et al.*, 2007c). Consequently, it is not possible to design and optimise fluidised bed coating processes without extensive trial-and-error testing which results in expensive and time-consuming scaling studies because of the large amount of variables involved (Cooper and Coronella, 2005). Therefore, in order to reduce the research and design work, mathematical models could be used to understand and clarify the impact of different input variables on process efficiency.

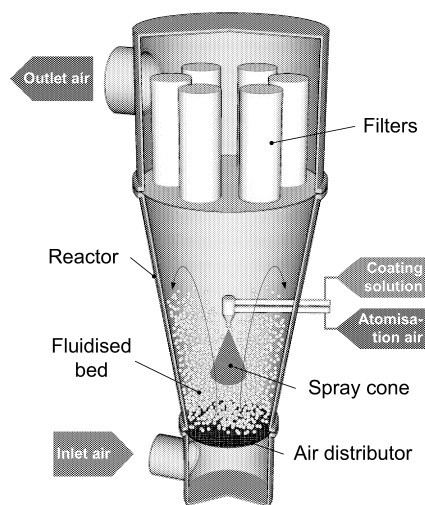


Figure 1. Overview of the batch, top-spray fluidised bed coating reactor.

Computational Fluid Dynamics (CFD), a powerful numerical tool for solving fluid flow problems, has been widely used in an attempt to model gas-solid fluidised beds using two different approaches: a discrete method (Euler-Lagrangian model) and a continuous approach (multifluid or Eulerian-Eulerian model). In the discrete phase method, the force balance, with the inclusion of contact forces arising during interparticle collisions, is calculated for each particle within the solid phase while the fluid phase is described by a locally averaged Navier-Stokes equation with the use of interphase forces for coupling of the two phases. The multifluid model, on the other hand, is based on continuum mechanics which treat the two phases as interpenetrating continua (Taghipour *et al.*, 2005). Up to date, many researchers have attempted to study the complex flow behaviour in gas-solid flow systems by means of CFD,

as shown in the review papers of Lettieri and Mazzei (2009) and Zhou (2009).

In this paper, the hydrodynamic behaviour of the fluidised bed coater was modelled by means of CFD associated with an Eulerian-Eulerian approach. Modelling was performed in four successive steps. First, a 2-phase gas-solid CFD model was developed in which the appropriate drag model was selected that gave the best agreement with the experimental PEPT data from Depypere *et al.* (2009). Also, an improved model was developed based on a 4-phase Eulerian model to account for particulate phase polydispersity and to improve overall agreement with the experimental data. Next, the release of compressed air, resulting from the use of the binary nozzle, was added to the CFD-model. In a third step, the atomisation of the droplets was added by means of an air-blast atomizer model and droplets were tracked by means of a Lagrangian extension to the CFD model developed in the first two steps. A fourth and final step comprised the addition of the heat and mass transfer equations in order to describe phenomena such as particle (convective) heating and droplet evaporation.

MODEL DESCRIPTION

Introduction

An Eulerian modelling approach was used whereby the different phases were treated as interpenetrating continua by incorporating the concept of phase volume fraction, and to solve the conservation equation for each phase to obtain a set of equations which have a similar structure for each phase.

Governing equations: mass and momentum

The conservation of mass of phase q (with q , either gas or solid) is described as

$$\frac{\partial}{\partial t}(\alpha_q \rho_q) + \nabla \cdot (\alpha_q \rho_q \vec{v}_q) = 0 \quad (1)$$

where α_q is the phase volume fraction, ρ_q the density and v_q the velocity of phase q .

The volume fractions of each phase are constrained by (with N_q being the number of phases in the model):

$$\sum_{q=1}^{N_q} \alpha_q = 1 \quad (2)$$

The conservation of momentum for the fluid (i.e. gas) phase is given by the following equation:

$$\begin{aligned} \frac{\partial}{\partial t}(\alpha_l \rho_l \vec{v}_l) + \nabla \cdot (\alpha_l \rho_l \vec{v}_l \vec{v}_l) = & -\alpha_l \nabla \cdot p + \nabla \cdot \bar{\tau}_l \\ & + \alpha_l \rho_l \vec{g} - \sum_{s=1}^{N_s} K_{ls} \vec{v}_s \end{aligned} \quad (3)$$

In Eq. (3), v_{ls} is the slip velocity between the phases, where the subscript l denotes the fluid phase and s indicates the solid phase. The symbol N_s equals the number of solid phases in total. Most CFD models only treat a single solid phase, however in this paper, models having more than one solid phase were dealt with as well. Finally, in Eq. (3), K_{ls} is the drag force coefficient relevant to the phases l and s , p is the pressure and $\bar{\tau}_l$ the deviatoric effective stress tensor of the fluid phase.

Analogous, the conservation of momentum for each solid phase ($1 \leq s \leq N_s$) is expressed by adding the solid pressure term $-\nabla p_s$ to the right side of Eq. (3),

$$\begin{aligned} \frac{\partial}{\partial t}(\alpha_s \rho_s \vec{v}_s) + \nabla \cdot (\alpha_s \rho_s \vec{v}_s \vec{v}_s) = & -\alpha_s \nabla \cdot p - \nabla p_s \\ & + \nabla \cdot \bar{\tau}_s + \alpha_s \rho_s \vec{g} + K_{ls} \vec{v}_s + \sum_{m=1, m \neq s}^{N_s} K_{ms} \vec{v}_m \end{aligned} \quad (4)$$

In this equation, K_{ls} denotes the momentum exchange coefficient between the fluid (i.e. gas) phase l and solid phase s , while K_{ms} represents the momentum exchange coefficient between solid phases s and m ($1 \leq s \leq N_s$, $m \neq s$, only applicable when using more than one solid phase).

Interphase momentum exchange coefficients

It can be seen in Eqs. (3) and (4) that momentum exchange between the two phases (drag force) can be represented by the product of the slip velocity (v_{ls}) and the gas-solid exchange coefficient, K_{ls} .

In this study, five different drag force models were evaluated based on different exchange coefficient models. Besides the gas-solid exchange coefficient models available in FLUENT, namely the Wen-Yu model (1966), Symlal-O'Brien model (1989) and Gidaspow model (Gidaspow *et al.*, 1992), the other models proposed by Arastoopour *et al.* (1990) and Gidaspow (1994) – the so-called modified Gidaspow model – were evaluated for application in fluidised bed reactors with tapered geometry (as shown in Figure 1). For more details concerning these drag models, the reader is referred to Duangkhamchan *et al.* (2010).

When using more than one solid phase, the solid-solid momentum exchange coefficient, K_{ms} , needs to be calculated as well, as shown in Duangkhamchan *et al.* (2011).

Droplet model and discrete phase extension

In addition to solving transport equations for the continuous phases (i.e. gas and solids), a discrete phase of droplets was simulated in a Lagrangian framework. The trajectories of these discrete phase entities were computed individually by integrating the force balance of the droplets (Newton's second law) (Behjat *et al.*, 2010; Pimentel *et al.*, 2006),

(5)

With F_D , the drag force exerted onto the droplet, v_d being the droplet velocity and, ρ_d and ρ_l being the density of the droplet and the gas phase, respectively. Assuming spherical droplets, the drag force was calculated using the Morsi and Alexander (1972) drag coefficient correlation. Initial droplet diameter, at the nozzle, was calculated using the air-blast atomizer model. For more details concerning the droplet model, the reader is referred to Duangkhamchan *et al.* (2012).

In the overall multiphase CFD model, the coupling between the continuous (gas/solids) and discrete (droplets) phases and the impact on both the discrete phase trajectories and the continuous phase flow were included.

Governing equations: energy

In the final stage of model development, heat and mass transfers were included using the conservation of energy equation. For the gas phase, this conservation equation is expressed as

$$\frac{\partial}{\partial t}(\alpha_l \rho_l h_l) + \nabla \cdot (\alpha_l \rho_l \bar{v}_l h_l) = -\alpha_l \frac{\partial p_l}{\partial t} + \tau_l : \nabla \bar{v}_l - \nabla \cdot \bar{q}_l + \sum_{s=1}^{N_s} Q_{ls} + Q_{ld} + m_{ld} h_{ld} \quad (6)$$

And for the solid phase(s),

$$\frac{\partial}{\partial t}(\alpha_s \rho_s h_s) + \nabla \cdot (\alpha_s \rho_s \bar{v}_s h_s) = -\alpha_s \frac{\partial p_s}{\partial t} + \tau_s : \nabla \bar{v}_s - \nabla \cdot \bar{q}_s + Q_{sl} + \sum_{m=1, m \neq s}^{N_s} Q_{sm} + Q_{sd} \quad (7)$$

In Eqs. (6) and (7) is h the specific enthalpy of the phase, Q is the intensity of interphase heat exchange and q is the heat flux (thermal conduction). Concerning the interphase heat exchange, the gas phase energy conservation equation contains transfer terms with the solid phases (Q_{ls}) and the droplet (discrete) phase (Q_{ld}). The solid phase conservation equation contains transfer terms with the other solid phases (Q_{sm}), the gas phase (Q_{sl}) and the droplet phase (Q_{sd}). These transfer terms are calculated using the dimensionless Nusselt numbers.

For the droplet phase (discrete), the energy conservation equation was expressed on an individual droplet basis. Heat and mass transfers were estimated using the dimensionless Nusselt and Sherwood numbers. The complete overview of all model equations is presented in Duangkhamchan (2012).

NUMERICAL SET-UP

The half geometry of a laboratory-scale Glatt GPCG-1 fluidised bed (Glatt GmbH, Germany), as shown in Figure

2, was defined and a grid was generated using Gambit 2.2.30 (Ansys Inc., Canonsburg, PA). A hybrid hexahedral-tetrahedral grid with mesh refinement at near-wall regions was generated, containing 108721 cells. Adding the nozzle into the model geometry further increased mesh complexity up to 209955 cells. For the modelling work including droplet dispersion, a full geometry mesh was used and contained up to 473083 cells.

The mesh was exported into Ansys Fluent v12 (Ansys Inc., Canonsburg, PA). Flow turbulence was simulated using the standard k- ϵ model with standard wall functions, and first order upwind schemes were selected for the convection terms. The relation between velocity and pressure corrections was calculated using the phase-coupled SIMPLE algorithm. Finally, a time step of 0.0001 s with a maximum of 100 iterations per time step was chosen in order to improve convergence behaviour. CFD simulations were performed using a single-precision, unsteady-state, first order implicit solver.

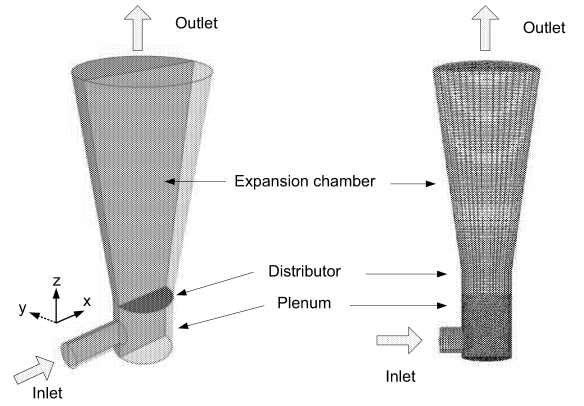


Figure 2. The Glatt GPCG-1 fluidised bed reactor geometry (left) and the mesh used in the CFD model (right).

EXPERIMENTAL VALIDATION

For the validation of the model predicted results, the experimental data obtained by Depypere *et al.* (2009) were used. In this research work, fluidisation experiments were conducted in a laboratory-scale Glatt GPCG-1 fluidised bed (Glatt GmbH, Germany), the reactor had dimensions $0.15 \times 0.56 \times 0.30$ m (*bottom diameter* \times *height* \times *top diameter*).

For the fluidisation experiments 0.75 kg of glass beads (Microbeads®, Sovitec, Belgium) were used (surface-weighted diameter, d_{32} : 196.5 μm). The motion of the glass beads (solids) inside the reactor vessel was recorded using Positron Emission Particle Tracking (PEPT). This technique allows 3-D movement of a single tracer particle to be followed in a non-invasive way. By tracking the particle location and movement over prolonged periods, time-averaged steady-state solids volume concentration and voidage profiles can be derived.

RESULTS

Hydrodynamic bed behaviour modelling

As a first step, a two-phase (solid/gas) CFD model was used to predict the hydrodynamic behaviour of the fluidised bed. Different drag force models were evaluated in order to select the most suitable drag model for further modelling.

Using the CFD model, it was found that after simulating 5 seconds of fluidisation, near steady-state conditions were attained (Duangkhamchan *et al.*, 2010). Consequently, to evaluate the model-predicted voidage profiles with the experimental PEPT data, time averaged profiles were taken between 5 and 15s of simulated data.

In Figure 3, comparison is made between the model-predicted voidage profiles using five drag models and the experimental voidage profile, as measured using PEPT.

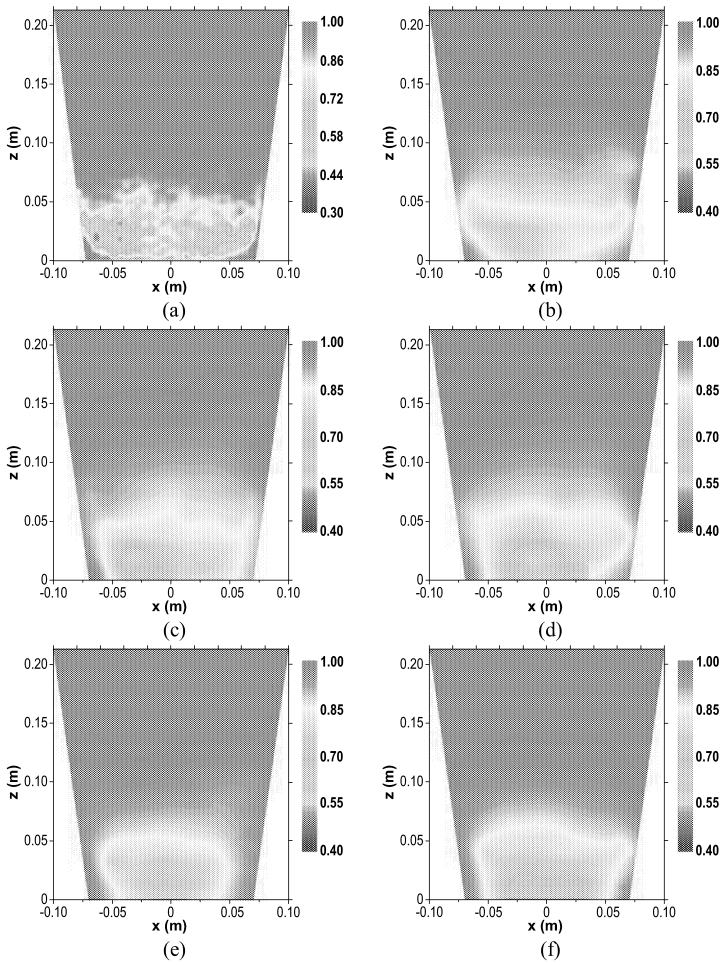


Figure 3. Model-predicted (2-phase) and experimental bed voidage (dimensionless) contour plots in the XZ plane for glass beads fluidised at $97 \text{ m}^3 \text{ h}^{-1}$ from (a) PEPT-experiment, (b) Wen-Yu, (c) Symlal-O'Brien, (d) Gidaspow, (e) modified Gidaspow and, (f) Arastoupour model.

From Figure 3, it is found that the model-predicted voidage contours showed poor agreement with the experimental results. A possible explanation could be the effect of the width of the particle size distribution used in the experiments as opposed to the model, in which the solid phase is characterised by a single particle diameter.

In order to study the effect of particle size distribution, the simulations were repeated using the 4-phase Eulerian model, in which three separate solid phases were defined. The diameters of the solids in each of the three phases were 135, 185 and 235 μm , respectively. These particle sizes correspond to the average size of the particles with a diameter below the 20th, between the 20th and 80th, and above the 80th percentile, respectively, from the particles used in the PEPT-experiments, as is also shown in Figure 4 (Depypere *et al.*, 2009).

The voidage profiles, as predicted by the 4-phase model and using 5 different drag models, are presented in Figure 5. As can be observed, significant improvement over the 2-phase model was achieved. Comparing the different drag models, it was found that the modified Gidaspow model (Fig. 4e) gave the best agreement compared to the experimental PEPT results.

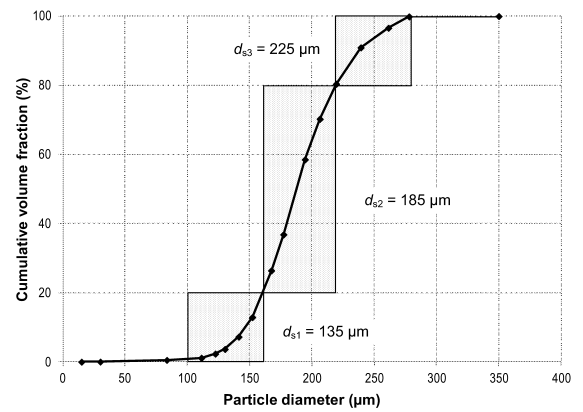
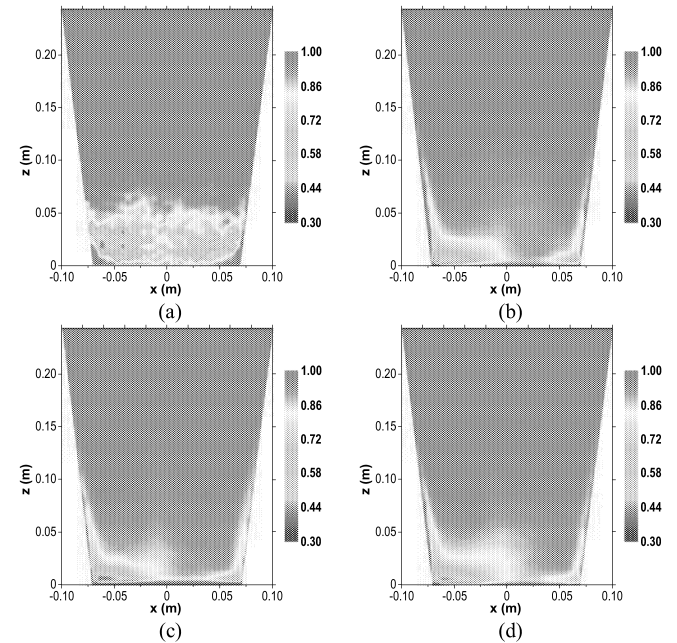


Figure 4. Particle size distribution of the glass beads used in the PEPT-measurements and definition of the 3 solid phases with their corresponding diameter in the 4-phase model.



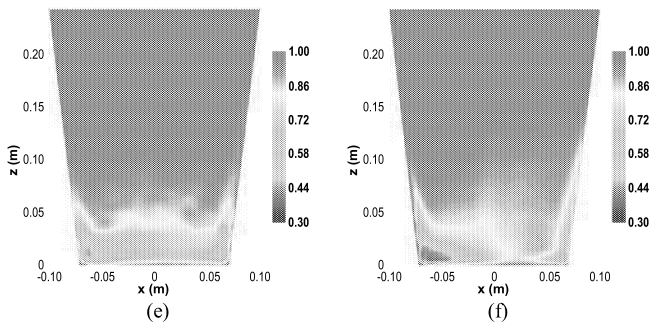


Figure 5. Model-predicted (4-phase) and experimental bed voidage (dimensionless) contour plots in the XZ plane for glass beads fluidised at $97 \text{ m}^3\text{h}^{-1}$ from (a) PEPT-experiment, (b) Wen-Yu, (c) Symlal-O'Brien, (d) Gidaspow, (e) modified Gidaspow and, (f) Arastoopour model.

Effect of atomisation air

In the second step, the model geometry and associated boundary conditions were modified to include the pneumatic nozzle in the modelled reactor domain. The simulations were carried out using the modified Gidaspow drag model, as it has been demonstrated in the previous section to be the most suitable drag model. Furthermore, all results presented in this and the next sections were all carried out using the 4-phase Eulerian CFD model. A comparison between simulation and experimental results with variation of atomisation air pressure, more specifically pressures of 1.5, 2, 3 and 4 bar, is presented in Figure 6.

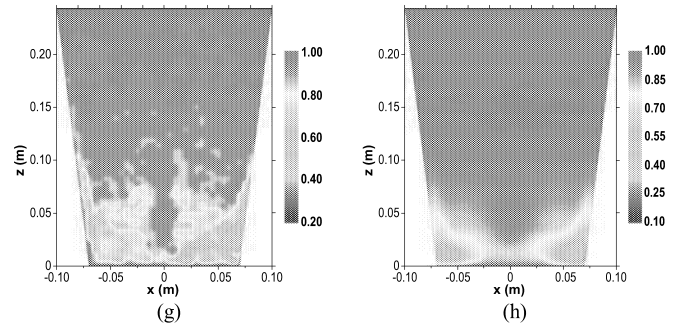
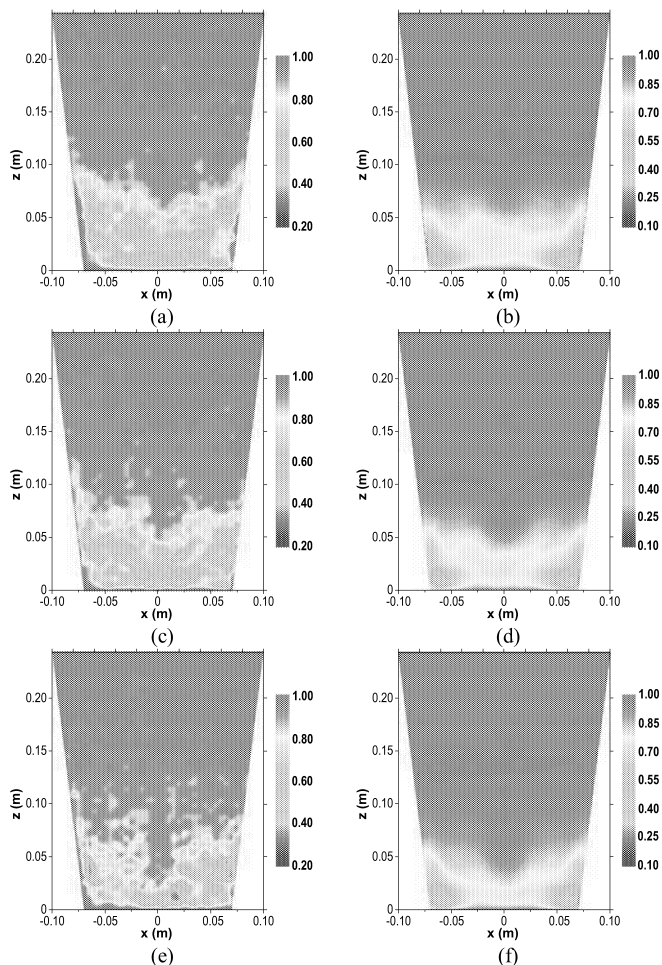


Figure 6. Comparison between PEPT and simulated, time-averaged steady-state voidage in the YZ plane at different atomisation air pressures: (a) PEPT-1.5 bar, (b) simulation-1.5 bar, (c) PEPT-2 bar, (d) simulation-2 bar, (e) PEPT-3 bar, (f) simulation-3 bar, (g) PEPT-4 bar, (h) simulation-4 bar.

From these figures, the change of the time-averaged voidages with the increase of atomisation pressure can be observed. More specifically, the central part of the conical vessel below the nozzle (positioned 12 cm above the air distributor) is occupied by a hollow cone. As seen in the experiments and as predicted by the model, this hollow cone enlarged with the increase of atomisation air pressure resulting in a smaller radial zone between the nozzle atomisation cone and the reactor wall. In the hollow region below the nozzle, the solid particles have to be lifted by the fluidising air against the counterforce of the atomisation air resulting in a voidage. It could be explained that particles move predominantly upwards in the centre to the above bed region, then move radially towards the walls and downwards along the walls. This particle flow behaviour was confirmed by experimental results obtained by Positron Emission Particle Tracking (PEPT) (Depypere *et al.*, 2009).

Again, these results confirm that using the 4-phase Eulerian model and the modified Gidaspow drag model, sufficient accuracy can be achieved in predicting the time-averaged hydrodynamic behaviour of the fluidised bed.

Droplet dispersion

Droplet dispersion was added to the 4-phase CFD model by using a Lagrangian extension (also called discrete phase model, DPM) in which individual droplets were tracked throughout the computational domain. Initial droplet diameter was calculated using the air-blast/air-assisted atomiser model (Duangkhamchan *et al.* 2012), of which the parameters were calibrated using experimental droplet size data as supplied by the nozzle's manufacturer (Duesen-Schlick, Germany).

Figure 7a shows the contour plot of the simulated time-averaged steady-state voidage when fluidising 1 kg of glass beads using a fluidisation air flow rate of $97 \text{ m}^3\text{h}^{-1}$. As can be observed from this figure, in the central part of the reactor, the region under the nozzle is occupied by the hollow atomisation cone.

Fig. 7b shows the droplet positions at $t = 15$ s. The calculated droplet tracks revealed that droplets moved downwards along with the atomisation air cone until facing the counter-current fluidising solid particles. Considering the absence of phenomena including droplet evaporation and droplet/solids adhesion, the DPM algorithm continues to track the droplets until they exit the reactor at the top or impact one of the reactor geometry boundaries. In reality, the majority of the droplets adhere onto the fluidised particles, contributing to the layered growth of the coating wall around the individual core particles.

Unfortunately, due to practical constraints in the PEPT experiments it was not possible to trace droplet trajectories and consequently, no validation of the droplet trajectories could be performed in a liquid-sprayed gas-solid fluidised bed. However, limited validations using fluorescent dyed coating solutions sprayed in a transparent reactor, in the absence of the fluidised particles and using high-speed imaging recording proved satisfactory agreement with the model predicted droplet trajectories (Duangkhamchan *et al.*, 2012).

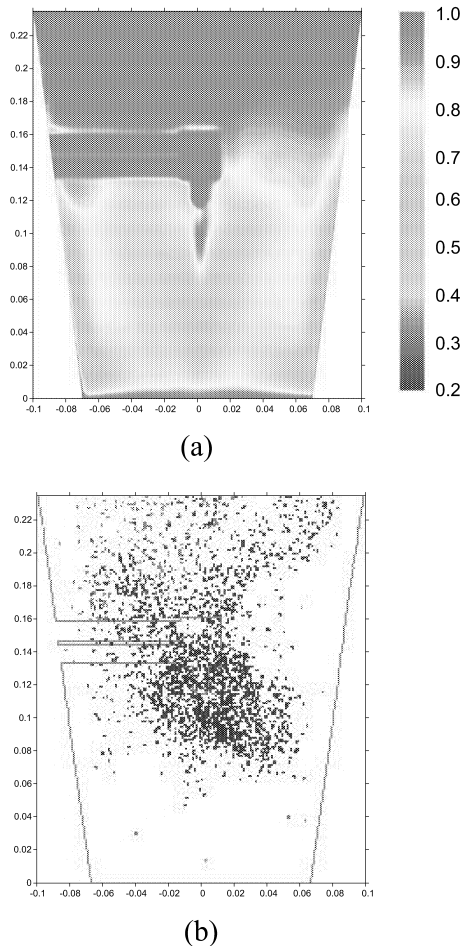


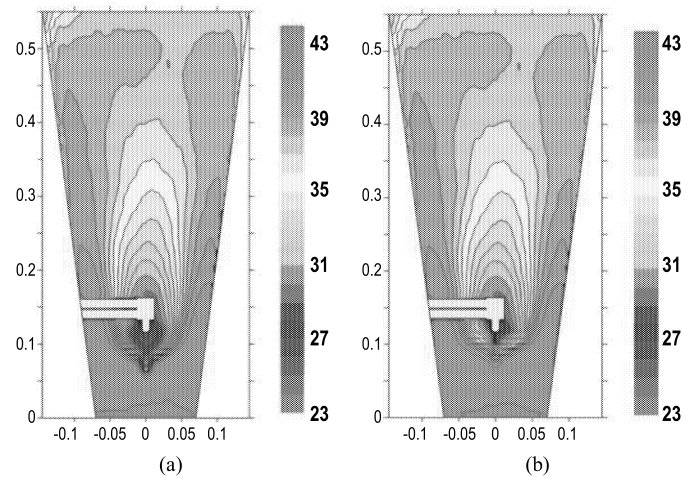
Figure 7. The simulated time-averaged voidage profile in the XZ-plane with 1 kg of glass beads and a fluidisation air flow rate of $97 \text{ m}^3\text{h}^{-1}$ (a) and (b), the corresponding droplet tracks, simulated at $t = 15$ s.

Heat and mass transfer

In a final and still ongoing step in modelling the fluidised bed coating process, the energy conservation equation was added to the existing 4-phase model with the Lagrangian extension for the droplet trajectories. Heat transfer between the gas and solid phases was modelled, as well as the heat and mass transfer between the individual droplets (Lagrangian extension) and the gas phase.

Preliminary simulations were performed to test the model and comparison was made with the reference experimental scenario described in Ronse *et al.* (2007b). In this reference scenario, 0.75 kg of glass beads with an average diameter of $365 \mu\text{m}$ were fluidised using air at 50°C and plain water was atomised onto the bed at a rate of 5.52 g/min and using atomisation air at 2.5 bar. These boundary conditions were also applied in the preliminary simulations using the 4-phase model, of which the three solid phases were defined to have a particle diameter of 230, 330 and $430 \mu\text{m}$.

The model-predicted time-averaged gas (air) and solids temperature distribution as well as the air absolute humidity are plotted in Figure 8. The model-predicted air temperature and absolute humidity distributions were consistent with the experimental observations carried out by Jimenez *et al.* (2006). The air and solid temperature contour plots revealed the existence of a low temperature region below the binary nozzle partly. In this region, the temperatures of gas and solid phases were approximately $26\text{-}29^\circ\text{C}$ below the fluidisation inlet air temperature. The presence of the low temperature zone can be explained by the evaporation of freely moving droplets – hence the higher air humidity, as well as by the release of cold (room temperature) compressed air.



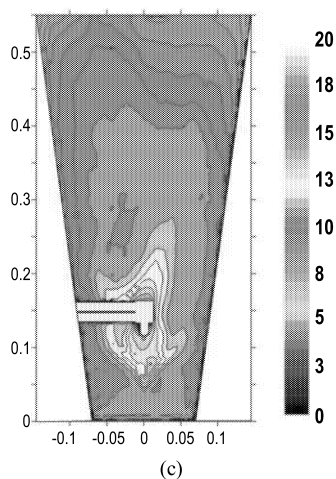


Figure 8. The simulated time-averaged air (a) and solids (b) temperature ($^{\circ}\text{C}$) in the XZ-plane, and (c) the time-averaged absolute air humidity (g/m^3).

Also, the low temperature zone below the nozzle extended deeper for the gas phase compared to the solids. This observation is explained by the predominant upward movement of solid particles in the centre-bottom part of the bed. Due to thermal inertia of the particles, they require a certain time and consequently, a certain vertical distance, until they equilibrate with the local (colder) temperature of the gas phase below the nozzle.

However, when the modelled outlet air temperature of the reactor, being 37°C , was compared to the experimental value of 30.4°C (Ronsse *et al.*, 2007b), a large discrepancy was observed. The reason for this difference is the absence of the droplet-particle interaction in the current model. In reality, droplets adhere onto the fluidised particles and through evaporation, they remove latent heat at the particle surface. Because in the model, droplets do not interact with the solid particles in the model, the algorithm continues to track droplets until they exit the reactor or impinge on the reactor walls. Thus, only evaporation in freely moving droplets is taken into account. Consequently, the overall latent heat removal from the fluidised bed was largely underestimated in the model, explaining the higher air and solids temperatures observed in the simulation. Therefore, in future work, the presence of droplet deposition onto the fluidised particles and the subsequent heat and mass transfer between fluidising hot air and wet particles will be taken into account.

CONCLUSIONS

In this paper, a multiphase Computational Fluid Dynamics (CFD) model was developed to simulate the batch fluidised bed coating process. A modelling methodology was presented which included a stepwise addition of complexity to the CFD model with experimental validation at each step. Through modelling, it was concluded that a 4-phase model could provide significant model accuracy in order to account for the polydispersity of the fluidised solids. Also, in tapered fluidised beds, the modified Gidaspow drag model has been

demonstrated to give the most accurate prediction of solids volume concentration or voidage profiles.

When droplet behaviour has to be included into the model, then a hybrid multiphase Eulerian-Lagrangian model, whereby droplets are modelled as discrete entities proved to be adequate. Considering the modelling of heat and mass transfer during fluidised bed coating processes it has been demonstrated that the model-predicted result was consistent with the experimental tendency. However, discrepancy between the measured outlet air temperature and that predicted by the CFD model could be seen. In order to resolve these discrepancies, other mechanisms including droplet/particle adhesion and mass transfer occurring at the surface of wetted particles, need to be included in the model as well.

Ultimately, the goal in modelling the fluidised bed coating process is to achieve a complete process model in which phenomena such as agglomeration, layered growth and spray drying losses can be predicted.

ACKNOWLEDGEMENTS

Part of the research presented in this paper was funded by the Special Research Fund of the Ghent University.

REFERENCES

- Arastoopour, H., Pakdel, P., Adewumi, M. 1990. Hydrodynamic analysis of dilute gas-solids flow in a vertical pipe. *Powder Technology*, 62, 163-170.
- Behjat, Y., Shahhosseini, S., Marvast, M.A. 2010. Modeling gas oil spray coalescence and vaporisation in gas solid riser reactor. *International Communications in Heat and Mass Transfer*, 37, 935-943.
- Cooper, S., Coronella, C.J. 2005. CFD simulation of particle mixing in a binary fluidised bed. *Powder Technology*, 151, 27-36.
- Depypere, F., Dewettinck, K., Ronsse, F., Pieters, J.G. 2003. Food powder microencapsulation: principles, problems and opportunities. *Applied Biotechnology, Food Science and Policy*, 1, 75-94.
- Depypere, F., Pieters, J.G., Dewettinck, K. 2009. PEPT visualisation of particle motion in a tapered fluidised bed coater. *Journal of Food Engineering*, 93, 324-336.
- Duangkhamchan, W., Ronsse, F., Depypere, F., Dewettinck, K., Pieters, J.G. 2010. Comparison and evaluation of interphase momentum exchange models for simulation of the solids volume fraction in tapered fluidised beds. *Chemical Engineering Science*, 65, 3100-3112.
- Duangkhamchan, W., Ronsse, F., Dewettinck, K., Pieters, J.G. 2011. CFD study of solids concentration in a fluidised-bed coater with variation of atomisation air pressure. *Powder Technology*, 212, 103-114.
- Duangkhamchan, W., Ronsse, F., Depypere, F., Dewettinck, K., Pieters, J.G. 2012. CFD study of droplet atomisation using a binary nozzle in fluidised bed coating. *Chemical Engineering Science*, 68, 555-566.
- Duangkhamchan, W. 2012. CFD modelling of the fluidised bed coating process. PhD dissertation, Ghent, 196p.

- Gidaspow, D., Bezuruah, R., Ding, J. 1992. Hydrodynamics of circulating fluidized beds, kinetic theory approach. *Proceedings of the 7th Engineering Foundation Conference on Fluidisation, Brisbane, Australia*, 75-82.
- Gidaspow, D. 1994. Multiphase flow and fluidisation. Academic Press, San Diego.
- Guignon, B., Duquenoy, A., Dumoulin, E. 2002. Fluid bed encapsulation of particles: principles and practice. *Drying Technology*, 20, 419-447.
- Jiménez, T., Turchiuli, C., Dumoulin, E. (2006). Particles agglomeration in a conical fluidized bed in relation with air temperature profiles. *Chemical Engineering Science*, 61, 5954-5961.
- Lettieri, P., Mazzei, L. 2009. Challenges and issues on the CFD modeling of fluidised beds: a review. *Journal of Computational Multiphase Flows*, 1, 83-131.
- Morsi, S.A., Alexander, A.J. 1972. An investigation of particle trajectories in two-phase flow systems. *Journal of Fluid Mechanics*, 55, 193-208.
- Pimentel, R.G., de Champlain, A., Kretschmer, D., Stowe, R.A., Harris, P., Kurbatskii, K. 2006. Improved atomization model for CFD codes. *Proceeding of the International Conference on Liquid Atomisation and Sprays Systems*, Kyoto, Japan.
- Ronsse, F., Pieters, J.G., Dewettinck, K. 2007a. Combined population balance and thermodynamic modelling of the batch top-spray fluidised bed coating process. Part I – model development and validation. *Journal of Food Engineering*, 78, 296-307.
- Ronsse, F., Pieters, J.G., Dewettinck, K. 2007b. Combined population balance and thermodynamic modelling of the batch top-spray fluidised bed coating process. Part II – Model and process analysis. *Journal of Food Engineering*, 78, 308-322.
- Ronsse, F., Pieters, J.G., Dewettinck, K. 2007c. Numerical spray model of the fluidised bed coating process. *Drying Technology* 25, 1491-1514.
- Symlal, M., O'Brien, T.J. 1989. Computer simulation of bubbles in a fluidized bed. *AIChE Symposium Series*, 85, 22-31.
- Taghipour, F., Ellis, N., Wong, C. 2005. Experimental and computational study of gas-solid fluidized bed hydrodynamics. *Chemical Engineering Science*, 60, 6857-6867.
- Wen, C.Y., Yu, Y.H. 1966. Mechanics of fluidization. *Chemical Engineering Progress Symposium Series*, 62, 100-111.
- Zhou, L.X. 2009. Two-Fluid Models for simulating dispersed multiphase flows - a review. *Journal of Computational Multiphase Flows*, 1, 39-56.

ENERGY APPLICATIONS IN FOOD PRODUCTION

Simulation based Energy Management Tools for the Food Processing Industry

Sven Franke
Chair of Food Packaging Technology
Technische Universitaet Muenchen
85354 Freising - Weihenstephan
sven.franke@tum.de

Isabel Osterroth
Chair of Food Packaging Technology
Technische Universitaet Muenchen
85354 Freising- Weihenstephan
Isabel.osterroth@wzw.tum.de

Horst-Christian Langowski
Chair of Food Packaging Technology
Technische Universitaet Muenchen
85354 Freising- Weihenstephan
langowski@wzw.tum.de

Josef Höfler
Chair of Mathematical Statistics
Technische Universitaet Muenchen
85354 Freising- Weihenstephan
josef.hoefler@tum.de

Tobias Voigt
Chair of Food Packaging Technology
Technische Universitaet Muenchen
85354 Freising- Weihenstephan
Tobias.voigt@wzw.tum.de

Hannes Petermeier
Chair of Mathematical Statistics
Technische Universitaet Muenchen
85354 Freising- Weihenstephan
hannes.petermeier@tum.de

KEYWORDS

energy management, simulation, process integration, optimization

ABSTRACT

Energy demand is an increasingly important issue in the field of food manufacturing because of continuously rising energy cost and of the trend to reduce greenhouse gas emissions. Thus there is a demand in methods to improve the energy efficiency of food production processes as a whole since the plant-specific optimization of single components is already touching its limits. Hence the present work shows a model based approach to improve the energy efficiency of a food production line that can be obtained just via using structured and standardized process data and applying data analysis methods without the need to replace a single component. Exemplarily for a dairy plant it is shown that an overall energy saving of up to 43 percent can be obtained by the integration of a stratified heat storage tank and process modification methods.

In addition, the process simulation tools allow to test different optimization methods as well as to assess conceptual changes in the process heat supply. To illustrate the latter, a case study of heat recuperation within a production process is shown. The tools may be used as a part of an energy management system?

INTRODUCTION

In the EU, food production is the second largest sector of the manufacturing industries, representing 14.5% of the total manufacturing turnover, which is equivalent to 917 billion Euros per year.

The main energy consumers in the food industry, in descending sequence, are dairies, sugar production, bakeries, meat processing, breweries and starch industry. Their share in the energy demand of the whole food industry is 52%. Main energy sources are natural gas (49%), electricity (23%), fuel oil (21%) and coal (7%). [2, 3, 6, 7]

A way for the food industry to comply with the governmental initiatives is to implement an energy management system (EMS). Energy management means a foresighted, organized and systematic generation,

distribution and utilization of energy, taking environmental and economic objectives into consideration. [4]

The latter have been standardized in ISO 50001 (August 2009). The functions of an energy management according to [1, 5] are:

- Energy data warehousing (collect, store, access, analyze)
- Centralized management and monitoring of energy distribution
- Continuous production process optimization targeted at minimum energy consumption
- Reduction of energy system running cost

Finally an EMS as sketched above has to be integrated into the MES (manufacturing execution system) of any potential user [11].

Thus the results of the model validation are discussed and as an application a case study, a variation in the process technology by a virtual modification shows the effect of heat recuperation between two processes

MATERIALS AND METHODS

Process description

For this study process data from a dairy plant with 16 unit operations have been specifically collected for production and packaging of three different product groups, namely fresh milk, high shelf-life products and special yoghurt products. In addition to electricity from the public grid, the plant utilizes steam produced by two steam generators fed by natural gas for processing. At the beginning of the study, no energy monitoring system was installed. To capture the initial situation of the energy consumption and to quantify possible improvement strategies, it was necessary to parameterize and to standardize the different processes and to define the system boundary of each operation unit according to the standardized process description.[8]

For the present work, two operation units, the yoghurt heater and the yoghurt chiller, were chosen to illustrate the methodic approach developed for energy management modeling and optimization.

Figure 1 shows a piping and instrumental diagram (P&ID) flowchart of the yoghurt heater. To acquire the relevant energy data, several measurement points had to be installed

as shown in the flowchart. These measuring points are reflected in the data base structure
 The yoghurt milk flowing from the storage tank is pre-heated by recuperator 1 and 2 before entering the homogenizer. After passing the homogenizer the milk is once more pre-heated by recuperator 3. Then, the primary heating module heats the milk to a pasteurization temperature of about 95°C which is kept constant throughout the holding section. Finally, the milk is cooled down to its fermentation temperature about 40°C by recuperator 2 and 3.

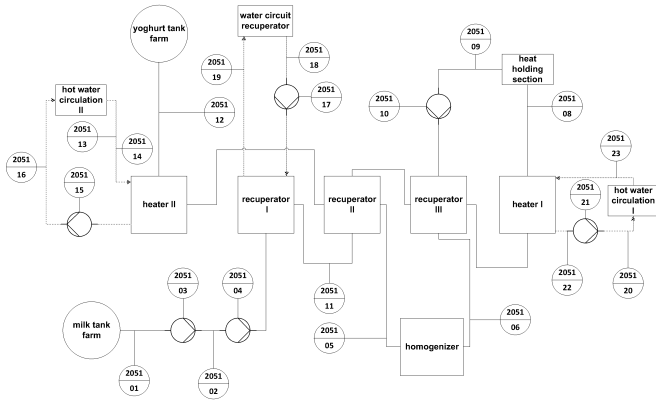


Figure 1 P&ID flowchart of the yoghurt-heating unit with several measurement points

The secondary heating module, also supported by a steam heat exchanger and a hot water circulation, controls the outlet temperature of the milk to this standardized fermentation temperature. The yoghurt heater system, which will be later used in the case study, has a recuperator (recuperator 1) to pre-heat the incoming milk by hot process water.

Further downstream from the fermentation vessel, the fermented milk (i.e. the yoghurt) goes to the cooling section to be cooled to a specific temperature of about 20°C which required for the filling process.

Figure 2 shows the P&ID flowchart of the yoghurt chiller. The unit consists of a heat exchanger, for pre-cooling the warm yoghurt from about 43°C with cold water and another heat exchanger to cool down the yoghurt from about 43°C to the required filling temperature with ice water.

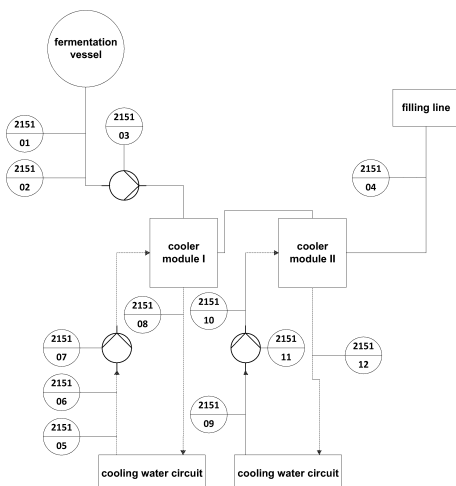


Figure 2 P&ID flowchart of the yoghurt-chilling unit with several measurement points

Data acquisition

The energy data acquisition of the different yoghurt processing units used both process data available from existing equipment and additionally acquired data from separate measurement points equipped with data loggers. In the following the measurement equipment for temperature and flow measurement as well as the measurement procedure is further described.

➤ Energy data acquisition – temperature data loggers

We applied a data logging system in form of a 16 channels recorder MS5+ by COMET Systems s.r.o., linked to Platinum resistance surface temperature sensors with an accuracy of $\pm 0.2^\circ\text{C}$ in a temperature range between -140 and $+100^\circ\text{C}$ and $\pm 0.2\%$ in the range between $+100^\circ\text{C}$ and $+600^\circ\text{C}$. To improve the heat transfer between the sensor and the pipe a special thermal paste was used.

➤ Energy data acquisition – flow rate measurements

As mobile flow rate measurement equipment, a Flexim Fluxus ADM 6725 was used, which is a mobile ultrasonic volumetric flow rate system consisting with clamp-on sensors and a data logging system. The sensor system has a measurement range between 0.01m/s and 25m/s with an measurement error up to $\pm 1.6\%$ of the measured value.

➤ Energy data acquisition - Implementation

The clamp-on temperature sensors were installed at the pipe surfaces of the units. The points - as indicated in the P&ID flowcharts - are described in table 1. The sensors were connected to a computer via the data logger system. For data acquisition, the software MSPlus of COMET Systems s.r.o. was used. The sample rate used was one minute and the time span of the measurements was 56 h for each unit.

Up to three different ultrasonic flow measurement systems was installed at the piping to detect the flows of the product as well as of ice water and hot water. As with the temperature sensors, the clamp-on ultrasonic flow sensors were installed at the pipe surfaces. The measurement principle was a quadruple sound path in reflection mode. Pipe sections that are straight over a longer distance are most suitable for this purpose.

The measurement points for the mass flow measurement are defined in the P&ID flowcharts and shown in in table 1.

Table 1 Measurement points of the examined units

Unit	Sensor Position	Sensor Type	Value
Yoghurt milk heater	Yoghurt milk in/out	Temperature	[°C]
	Yoghurt milk mass flow	Mass flow	[kg/min]
	Yoghurt milk before/after homogenizer	Temperature	[°C]
	Yoghurt milk before/after heat holding section	Temperature	[°C]
	Yoghurt milk between Recuperator I and II	Temperature	[°C]
	Hot water circulation secondary heater in/out	Temperature	[°C]
	Hot water circulation secondary heater mass flow	Mass flow	[kg/min]
	Hot water external heat exchanger in/out	Temperature	[°C]
	Hot water circulation primary heater in/out	Temperature	[°C]
	Hot water circulation primary heater mass flow	Mass flow	[kg/min]
Yoghurt milk chiller	Yoghurt in/out	Temperature	[°C]
	Yoghurt mass flow	Mass flow	[kg/min]
	Cooling water in/out	Temperature	[°C]
	Cooling water mass flow	Mass flow	[kg/min]
	Ice water in/out	Temperature	[°C]
	Ice water mass flow	Mass flow	[kg/min]

The measured signal is influenced by pipe thickness, pipe material, surface roughness of the inside of the pipe, sensor distance and sound path characteristics. These parameters have to be entered into the data processing software and to be verified via calibration measurements to get reliable results. The sampling rate was again set to one measurement per minute. The measured values were stored in the Flexim system.

Data management

For the data management of the measured data as well as for the simulated data a Microsoft SQL database was used. This database is the central part for all further steps and the interface to the data acquisition and the optimization methods. Figure 3 illustrates the database structure with the implemented tables. Each data point is defined by a sensor identification code. This sensor identification number is stored in the sensor definition table. Product-specific values like product density and product heat capacity are stored in definition tables.

This information is also stored in the data base structure: operating conditions are stored in the phase controlling table and defined in the phase definition table. This information is required for the dynamic energy analysis and furthermore to generate energy based key figures to identify a potential for the process integration.

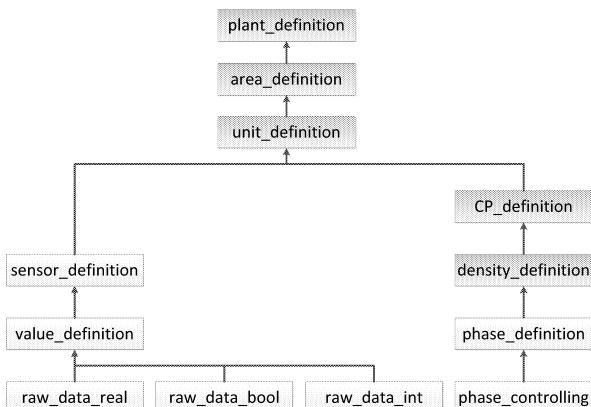


Figure 3 Data base structure implemented in a Microsoft SQL database

The database is connected to MATLAB and thus to the process simulation. Any energy analysis and database query is done by the MATLAB software. Furthermore the stored energy data is used for the automatic validation of the developed process simulation.

Process simulation

The model component library as well as the simulation was based on MATLAB Simulink [12]. For the present work, the most important component of the model library is the heat exchanger. All models were validated, as shown in the results section.

The validation of the process models ensures that the real behavior of the system under study is closely enough reflected by the model. [9, 10]

This allows a flexible adoption of different process simulation setups. An overview of the model components used in this study is given in Table 2.

Table 2 Components of the model library as generated in this work and implemented in MATLAB Simulink

Model component	Model behavior
Plate heat exchanger	Time dependent
Tube heat exchanger	Time dependent
Centrifugal Separator	Time dependent
Homogenizer	Time dependent
Pump	Time dependent (controlled variable)
Product filler	Constant
Electrical consumers	Constant

Note that the time dependency makes the analysis of efficiency for both transient and steady regimes possible.

For the computations, a standard desktop computer (2,66 GHz, 8 GB RAM, Microsoft Windows 7, 64bit Architecture) was used. For the simulation of a process time of 6 h, 8 min of simulation time were needed for the plant setup as discussed above. The input and output specification of the simulations are stated in the results section. The input temperatures are real data in the sense of initial values. The different production phases – production, cleaning, start-up, idle – are represented by different sets of initial temperature values and by their characteristic times.

Optimization tool - methodological approach

The most important components of the optimization tool are the database for real and virtual process data and the module library. The currently followed optimization strategy is summarized in figure 4. The idea of this approach is to compare different production scenarios by using the energy demand or characteristic times as key indicators. Different optimization fields, e. g. the usage of regenerative energies lead to different configurations or to a different operational sequence.

This flexible approach will be used in this paper to quantify a reduction in energy usage as one key indicator. A reduction in non-productive times -as a second key indicator- will be shown in our second paper.

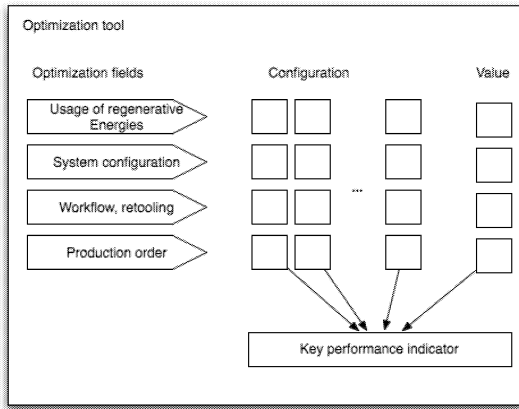


Figure 4 Schematic representation of the optimization tool

RESULTS

Process simulation validation results

The models of the yoghurt heater and of the yoghurt cooler were validated with the help of measured data.

For the validation the temperature of the inlet and outlet flow of the hot water circulation, input temperature of the product and inlet temperature of the ice water were taken as input parameters from measured values stored in the database. The simulated results of the product outlet temperature in different production phases were compared to the measured values. In addition, temperatures at other accessible points between in- and outlet were used to confirm the correct functioning of the simulation.

As an example, figure 5 shows the validation plot of the yoghurt heater. This validation plot compares the measured temperature of the product outlet (blue curve) according to table 1 with the simulated temperature of the product outlet (green curve) over time. The different colors of the bars highlight the different production states: light blue bars stand for production, yellow bars represent cleaning (CIP), green bars start-up and sterilization and white bars show the idle state.

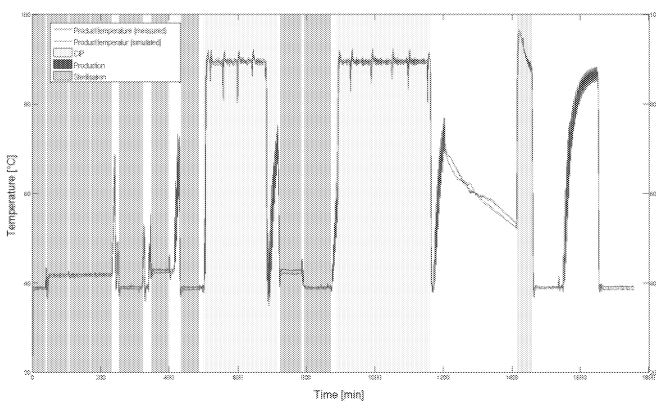


Figure 5 Validation plot of the yoghurt heater

The profile of the simulated temperature differs slightly from the measured data as described in the following. Table 3 summarizes the validation results for the different production phase. Hence for the validation, measured input values are used for the simulation as input variables and the so achieved

simulated values are compared to the measured values. The difference of the simulated and the measured values for each time step is the simulation error. The mean error of the yoghurt heater product outlet temperature is for the production phase -0.007°C with a standard deviation of 0.06°C . It can be observed that the mean error as well as the standard deviation is below 2°C for all components which is a good result for the simulation error.

Note that after a longer idle phase between the last cleaning (center of picture, yellow bar) and start-up (green bar) larger differences between simulated and measured outlet temperature can be observed. This error results from the cooling behavior of the model, since in the real process after cleaning the flush water remains in the piping system and thus the mass flow of the model during the idle phase is set to zero in the simulation due to computational necessities. This fact, however, is not critical for a proper description of the overall process, since in this idle phase no energy is supplied

Hence the model seems to depict the time behavior of the heater unit well for all production states.

Table 3 Standard deviation of simulated data vs. measured data

	Standard Deviation [$^{\circ}\text{C}$]	Mean error [$^{\circ}\text{C}$]
Yoghurt Chiller (n=192)		
Product	1.76	0.83
Cooling water	0.75	0.64
Ice water	1.94	0.62
Yoghurt Heater (n=1750)		
Product	0.06	-0.007
Hot water I	1.54	-1.55
Hot water II	0.51	-0.3

Simulation studies of the process integration

Apparently, the production process as shown above (see figure 6a) is characterized by different temperature levels in the different stages of production, which leads to energy losses. These losses may be reduced by intelligent techniques of heat storage. A cost efficient method for this purpose is the use of a stratified storage tank. In this tank water of different temperature can be stored on a different height level. The changed layout of the production plant as used for simulation can be seen in figure 6b. Using the model library, a suitable recuperator was set up to link the two processes, namely yoghurt heating and yoghurt cooling. The expected results of the heat integration are a reduction of the total energy usage both for the heating process of the yoghurt milk as well as for the cooling process

For the heat integration regenerator 1 of the yoghurt heater is used. This heat exchanger pre-heats the yoghurt milk directly with hot water coming from the upper layer of the stratified thermal storage tank.

In the cooling process of the yoghurt the first heat exchanger module warms the cooling water from a temperature of 3°C to a temperature of 35°C . This warmed water can now be

used in the yoghurt heating process to pre-heat the yoghurt milk directly. The cold return flow from the lower layer of the stratified storage tank is cooled down to 3°C by the cooling system of the dairy plant. This cooled water is used again for the yoghurt cooling process.

In the simulation, recuperator I of the yoghurt heating process is fed by heating water of a mass flow of 50 kg/min and a temperature of 30°C from the stratified storage tank. The incoming milk is pre-heated and the water is cooled down to a temperature of about 10°C. The cooled water is pumped to the NH₃ refrigeration plant where the whole return flow of the ice water system is cooled down to a temperature of 2-4°C. This water can be used directly to cool down the product in the yoghurt-cooling unit. As a result of this simulation, the advantage of this approach is a better usage of the thermal energy fed into the system. Table 4 shows the current energy demand and the simulation results of the yoghurt-heating unit based on different production states. It must be pointed out that the assumption for these results is that both heating and cooling run always in parallel.

The main differences between Yoghurt products A and B are their fat content, resulting in a different density and heat capacity, which in turn cause a difference in energy demand. The energy usage in the production of the different products is compared to the simulation study of the heat integration. At first glance, the simulation results point out a significant saving potential of up to 25% for the heating unit.

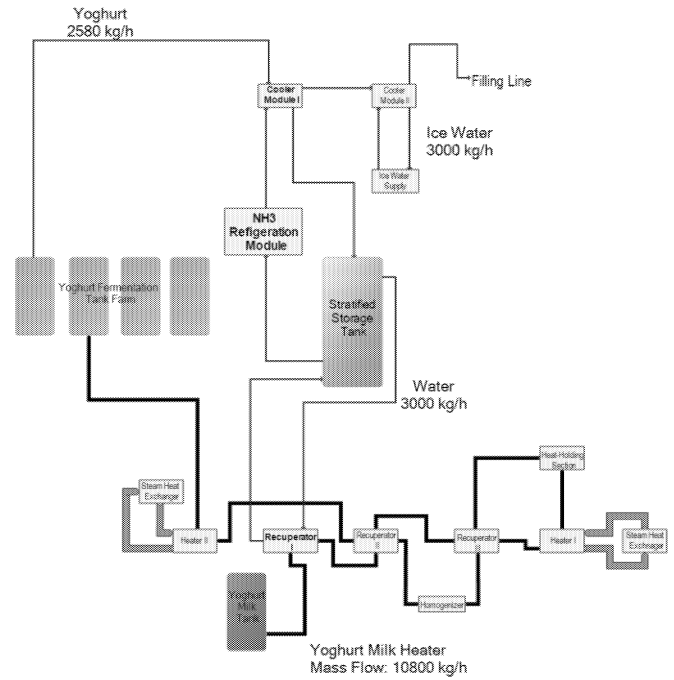


Figure 6b Basic flow sheet of the yoghurt heating and yoghurt cooling unit heat integration concept with a stratified storage tank and the connection to the NH₃ refrigeration plant

Table 4 Energy demand of the different production phases of the yoghurt-heating unit without and with a simulation based heat integration

Production phase	Current energy demand [kJ/min]	Energy demand with simulated heat integration [kJ/min]	Saving potential [%]
Phase one			
<i>Product A</i>	17540	13389	23
Phase two			
<i>Product B</i>	19528	15156	22
Phase three			
<i>Product B</i>	19847	15176	23
Phase four			
<i>Product B</i>	19776	15410	22
Phase five			
<i>Product A</i>	17714	13154	25

The energy needed to cool down the yoghurt is shown in table 5. Less energy for cooling is needed due to the heat exchange of the hot water return flow with the incoming cold milk in recuperator I as shown in figure 6b.

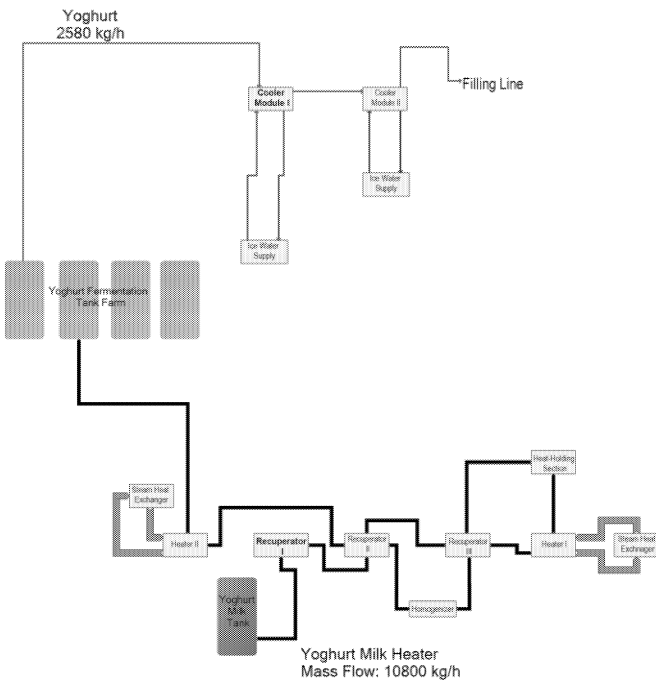


Figure 6a Setup of the yoghurt production line

Table 5 Demand for cooling of the different production phases of the yoghurt-cooling unit without and with a simulation based heat integration

Production phase	Current Energy demand for cooling [kJ/min]	Demand for cooling after simulated heat integration [kJ/min]	Saving Potential [%]
Phase one Product B	6554.81	875.34	86.65
Phase two Product D	4802.17	1022.7	78.70
Phase three Product B	6384.49	1231.88	80.71
Phase four Product B	6325.98	1132.31	82.10
Phase five Product B	6669.33	1439.28	78.42

If, however, a realistic production plan is taken as a basis, the saving potential is reduced. This is because the units are not running at synchronously, as different products are processed at the same time. The result of a simulation, which takes this fact into account, gives the results shown in table 6.

Table 6 Actual energy saving potential by heat integration

<u>Energy consumption yoghurt heating unit:</u>		
	[kJ]	[MWh]
Current operation	136119613.60	37.81
Heat integration (1379 min)	128112519.05	35.59
Saving	8007094.55	2.22
Saving [%]	5.88	5.88
<u>Energy consumption yoghurt cooling unit:</u>		
	[kJ]	[MWh]
Current operation	15556595.53	4.32
Heat integration (1379 min)	8800502.20	2.44
Saving	6756093.33	1.88
Saving [%]	43.43	43.43
<u>Total Energy consumption</u>		
	[kJ]	[MWh]
Current operation	151676209.13	42.13
Heat integration	136913021.25	38.03
Saving	14763187.88	4.10
Saving [%]	9.73	9.73

Taking this into account the true energy saving potential of both cooling and heating in this process is about 10%. Due to technological constraints, the use of heat integration is limited to the production phase. The energy efficiency refers to the associated savings in thermal energy by use of process waste heat. Note that the theoretical saving potential is still of interest since also integration with different units might be possible.

DISCUSSION/CONCLUSIONS

The presented work describes the different steps of the application of an energy management system toolbox developed to optimize the energy efficiency of a real medium enterprise dairy production unit for yoghurt milk. It focuses on the acquisition of energy relevant data, emphasizes the necessity of a standardized data base structure and gives thus also hints for similar assessments in other food processing units.

With these developed data base structure it is possible to use the database for further production based energy analyses. Since optimization by means of mathematical methods need reliable models, an exemplary validation of a model used in a case study is given to show the compliance of simulation and process data.

The validated model is used to point out the saving potential. The greatest energy savings in relation to the basic thermodynamic equations are obtained during the simulation setup: up to 80 percent for yoghurt cooling and 25 percent for yoghurt heating in case of an idealized plant setup. Taking real production schemes as a basis, the savings are up to 40 percent for yoghurt cooling and 6 percent for yoghurt heating. Integrating real production plans will lead to a correspondence to reality. Additional potential savings will result from the adjustment of the production plans of the two processes.

This shows that the model library is capable to forecast time dependent energy and temperature curves for different scenarios.

Note, that due to the sole consideration of thermal energy, the CO₂ savings can be regarded as being proportional to the energy savings.

Future work has to develop a set of key figures, which allow assessing and comparing the energy savings in a standardized way. The observed differences between idealized and realistic energy savings show that there is also a high potential in optimized production planning. The special advantage of this strategy would be to synchronize production flows and heat flows. This approach will be shown in a subsequent paper presented in this congress. As a conclusion, all strategies namely system configuration and workflow retooling and production planning should be optimized at the same time for a maximum effect.

The work ist funded by *Bayrisches Staatsministerium für Wissenschaft, Forschung und Kunst* in the *Foreta* Programme.

REFERENCES

- [1] Dong, Q.; De-jiang, Z.: The research and realization of energy management system in iron and steel enterprise. In: International Conference on Information, Networking and Automation (ICINA), 2010 (2010), S. V1-448-V1-451
- [2] AGEBA (2009): Energiebilanzen der Bundesrepublik Deutschland 1990-2007 und Auswertungstabellen 1990-2008. Published 2009.10.28 DIW Berlin, EEFA, Köln <http://www.ag-energiebilanzen.de>
- [3] IREES Fraunhofer ISI: Arbeitspapier zum Expertenworkshop: Möglichkeiten, Potenziale, Hemmnisse und Instrumente zur Senkung des Energieverbrauchs und der CO₂-Emissionen von

industriellen Branchentechnologien, (2010.6.15)
Frankfurt

- [4] VDI Norm 4602: VDI Norm 4602 - Blatt 1:
Energiemanagement - Begriffe Verband
Deutscher Ingenieure
- [5] Verband Deutscher Ingenieure: Betriebliches
Energiemanagement Energiecontrolling -
Energiekennwerte - Kostenaspekte - Verknüpfung
mit anderen Managementaufgaben -
Erfahrungsberichte und neue Ansätze ; Tagung
Cottbus, 6. und 7. März 2003. Düsseldorf: VDI-
Verlag, 2003
- [6] Lauterbach, C.; Schmitt, B.; Vajen, K.: Das
Potential solarer Prozesswärme in Deutschland Teil
1 des Abschlussberichts zum Forschungsvorhaben
"SOPREN-Solare Prozesswärme und
Energieeffizienz". Kassel, 05.12.2011
- [7] Bundesministerium für Umwelt, und
Reaktorsicherheit (BMU): N. Röttgen: Erneuerbare
Energien und Energieeffizienz rechnen sich auch
für Europa. Berlin
- [8] Franke, S.; Nophut, C.; Voigt, T.; Langowski, H.-
C.; Raab, F.; Ruß, W.; Petermeier, H.: Production
Process simulation for schedule based energy
optimization in the food industries. In:
FOODSIM2010, 2010
- [9] VDI Norm 3633 - Simulation von Logistik-,
Materialfluss- und Produktionssystemen.
Begriffsdefinitionen. Verband Deutscher
Ingenieure, 08.01.1996
- [10] Wenzel, S.: Verifikation und Validierung für die
Simulation in Produktion und Logistik
Vorgehensmodelle und Techniken. Berlin:
Springer, 1. Aufl., 2007
- [11] Amundsen, A.; (2000): Joint management of energy
and environment, Journal of Cleaner Production 8; S.
283-494
- [12] The MathWorks, Inc.: Simulink – Simulation and
Model-Based Design, reference:
<http://www.mathworks.de/products/simulink>

BIOGRAPHY

SVEN FRANKE was born in Schwelm, Germany and went to the Technische Universität München where he studied beverage technology and obtained his degree in 2008. Since October 2008 he works as a scientific assistant at the chair of food packaging technologies of the Technische Universität München. His fields of research are energy optimization of processes in the food industry and energy based process modelling and simulating.

ENERGY BASED PRODUCTION PLAN ASSESSMENT AND OPTIMIZATION

Josef Höfler
Hannes Petermeier

Chair of Mathematical Statistics
Technische Universität München
85354 Freising - Weihenstephan
email: josef.hoefler@tum.de

Sven Franke
Veronika Strobel

Horst-Christian Langowski
Chair for Food Packaging Technology
Technische Universität München
85354 Freising - Weihenstephan

KEYWORDS

Production planning, feedback loop for optimization, production fragmentation, network analysis, energy efficiency

ABSTRACT

The present work deals with the issue of the production plan optimization. As a first step towards an optimization, criteria allowing an assessment are needed making the comparison of different production plans with respect to energy efficiency possible. The use of validated models to simulate the production sequence allows a feedback loop for both assessment and improvement of energy efficiency and energy consumption. Thus the developed optimization of a production plan is a stepwise method, which is applied to an existent production plan. As first results potentials for energy saving as well as for reduction in idle times are shown. As constraints for the optimization process dependencies and enabling conditions between the involved production steps are determined. As an example, the heuristic optimization will be demonstrated on real data from a yoghurt-processing production line of a dairy. From an assessment of an optimized production plan, an energy saving potential up to 20 % for the starting phase and up to 7.5 % for the cleaning processes can be derived. This is resulting in an overall improvement of 3 % for the complete production.

INTRODUCTION

The retrospective production plan assessment as a preparatory measurement for the optimization is in general not common. In this context retrospective means the collection of production data in terms of produced quantities, idle times, energy consumption etc. for a determined production period. This information is used as an additional initial condition for the optimization of the future production and thus creating a feedback loop. Based on the hypothesis that an optimized production

plan ensures a balanced and thus efficient usage of energy, methods to assess as well as to optimize an existing production scheme are needed. Moreover, it is a good option to reduce idle times as well as energy usage in existent systems. For the description of production plans network analysis (Altrogge 1994) is a suitable method. In the present work, the definitions of critical paths as well as visual methods for the analysis of network systems are used.

Process units	Time per mass [min/1000kg]
Milk heater	00 : 04
Cream cooler	00 : 29
Cream heater	00 : 17
Preparation	01 : 03
Yoghurt heater	00 : 06
Yoghurt fermenter	01 : 06
Yoghurt cooler	00 : 07

Table 1: Typical production times per mass per process units

Furthermore, the central problem of the production plan optimization is making different production plans comparable. Thus, there is a need for key indicators, which on the one hand give quality functions for optimization and on the other hand criteria for both comparing and optimizing different production plans. A production plan optimization is per se time dependent. In the present study real plant data from a dairy is analyzed. The considered production steps are related with the heating and fermentation of yoghurt and thus, they represent a combination of a continuous and a batch process. Since heating and cooling processes are the main energy consumers in the whole production process, the current work focuses on those. To estimate the effects of changes in the production, validated models for the processes are used to simulate a virtual production. Therefore for the virtual production an assessment analogous to the real production data is possible. Of course, this makes a flexible model library necessary. An outline of the structure and basic principles of the latter as well as

the validation of the models and the simulation can be found in (Franke et al. 2012).

Note, that for the network sequencer discrete steps are used. As motivation for this approach table 1 below shows the different temporal behavior of process units in a dairy in terms of typical production times per processed mass of product. Since some of the process steps are dependent on others in the sense that they have to be immediately subsequent, this is a technological boundary condition and thus points to graph theory methods. The steps of the production processes and their hierarchy with respect to the product are shown in figure 1. The first two production steps are the delivery of the milk to the dairy and the separation of the fat. Afterwards the product stream is divided into cream, which needs to be cooled, and process milk, which runs through the short-time heating unit. For the production both the cream and the process milk need to be deployed. Note that all energy relevant processes are shaded grey.

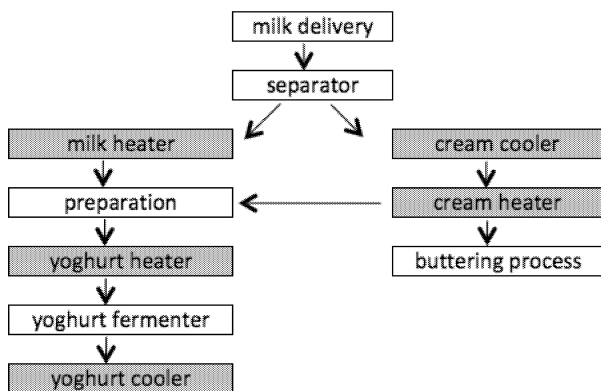


Figure 1: Hierarchy of the production process (energy relevant processes are shaded in grey)

Another way to show the structural and temporal dependencies is demonstrated in figure 2. The sequencer shows the filling and fruit dosage, which follows the yoghurt cooling. Hence, this is a subsequent step of the diagram in figure 1. Note, that the blocks are working steps with the necessary time period to complete the preceding working step at the connecting edges.

The paper outlines one possible approach for the production plan optimization. It is organized as follows (figure 3):

The section material and methods cover the description of the available production data, defines possible criteria to benchmark and shows a framework for the optimization. Hence, a heuristic for the described approach is applied to a dataset from a real yoghurt production in a dairy. The results of the analysis are used for a first algorithmic description of an optimization method. Note that the goal of the present work is a heuristic approach rather than a formal mathematical description.

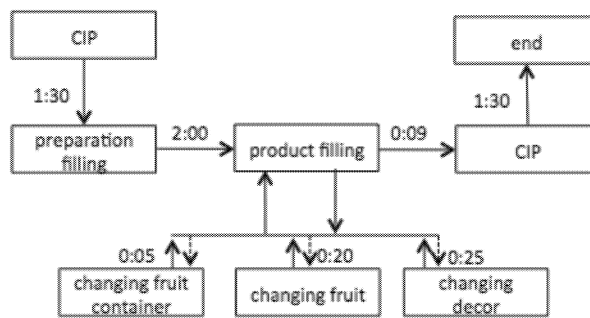


Figure 2: Structural dependencies with respect to time

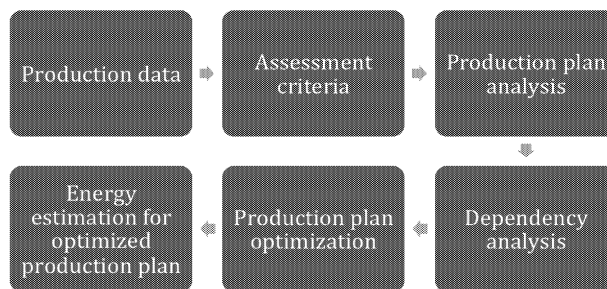


Figure 3: Stepwise procedure of this approach

MATERIALS AND METHODS

Production data

The production data has been recorded both manually and automatically. The manual data has been recorded by hand-written reports from the dairy. The manually collected data has been imported to a database. The reports contain the product type, the amount that has been produced as well as start and stop times. The automatically recorded data is based on the controlling database of the dairy. This data only includes the rough planning and no details about the daily production are included. For validation purpose this overview data can be compared to the manually recorded ones. Therefore, in this work the focus is on the manually documented production plans as the more relevant information. In the following, the data from an arbitrarily chosen month has been used as an example.

Since the same process units are used for different products the data is merged using e.g. the percentage of fat or other characteristics. This yields a more structured dataset and is therefore helpful for the analysis.

Assessment criteria of production plan

The production plan can be assessed using many different criteria. However, this work is focused on four common criteria, which are directly or indirectly connected

to the energy consumption. This connection to the energy consumption will be established for each criterion below. The production plans can be assessed using different criteria (Junge (2007), Kletti (2005)):

- Capacity utilization rate
- Product fragmentation
- Throughput
- Energy consumption

The capacity utilization rate is defined as the quotient of the effective production time and the processing time. Hence this key indicator is used to identify idle times. Note, that idle times in a heating process mean that either heater (or cooler) has to be kept on a specified temperature level and thus energy is wasted or that a heater cools down and a surplus of energy is again needed to reach the working temperature. So a difference in idle times is proportional to different amounts of energy used depending on the idle status.

Product fragmentation is defined by one minus the ratio of the number of starts for one product and the total number of products per day. In case of a dairy production, the product fragmentation is related to the capacity utilization rate. Due to a great number of product changes the same number of intermediate cleaning processes are required. This also means a loss of product resulting in a loss of energy. Thus, a less fragmented production plan uses less energy, since less starting and cleaning processes are needed, which have been caused by product changes.

The throughput is the produced amount of product per processing time. Although in the case of a dairy, the produced amount of milk is measured in tons, the throughput is proportional to a power stream and thus an indicator for balanced energy consumption. The latter is desirable because power peaks need a greater amount of energy supply kept in advance.

The energy consumption for a specific production plan is the most obvious way to benchmark a production plan. At the same time the criteria stated above can be used as explanatory variables for high energy consumption. This relationship makes the use of key performance indicators feasible. These energy performance indicators may be defined by e.g. the average energy used per 1 kg of product (Franke et al. (2012), Kessler (1988)).

For the energy consumption a calculation tool has been developed using MATLAB. The input variables of the calculation tool are the energy performance indicator(s), the product quantity and the production states. Furthermore, since the starting and cleaning processes are standardized procedures in the dairy under study, a fixed amount of energy could be added for each starting and cleaning process, respectively.

Dependency analysis

For the production plans the dependencies between production steps are important, since some production steps require other proceeding steps, as shown in figure 2. These dependencies can be analyzed and assessed using network analysis methods (Schwarze 2006). The idea of the network analysis is to depict the step-by-step dependencies of the processes. Hence, for every step the enabling condition as well as the subsequently enabled process units and produced intermediate products have to be traced. To visualize the dependencies as well as the enabling conditions sequencer diagrams are used (Unbehauen 2008). For the optimization of the production plans the enabling conditions and the dependencies are the constraints. Using networks to visualize the dependency structure allows to use critical path methods in terms of graph theory as a network analysis method.

The dependencies as well as the delay for each step are shown in a network block diagram. Using this representation the critical paths of the process can be determined. If the process of the critical path is delayed the whole system will be delayed. One block has the information of the earliest and the latest start as well as the stop time, the process time and the buffer time for e.g. intermediate products.

Since the production is only considered in discrete time steps, each production step is a vertex with properties described above. The dependencies are expressed by the edges, which are connecting the vertices. In this case the graph is directed since there is a distinction between two vertices respectively the two production steps.

For a detailed time dependent analysis of the production data Gantt charts are used. To identify the products, different colors are used for different products. Hence, the Gantt chart is utilized to detect idle times between the productions. Since each vertex is connected with its neighbors, the edge also represents an energy stream to or from a vertex. In thermodynamics and process technology, this scheme is known as Sankey diagram. The Sankey diagram is used for the visual representation of the energy flow in the system. The thickness of the arrows is proportional to the amount of energy transferred between the steps.

Optimization approach

The goal of the work is to find optimization methods for the production plan, which allow minimizing the energy consumption of a production and/or to maximize the energy efficiency (Elfner and Verein Deutscher Ingenieure and Universität Kaiserslautern 1998). To overcome the complexity and to include as many different enabling conditions and dependencies as possible, a heuristic in pseudo-code syntax will be presented and then it will be applied to an arbitrarily (Siedersleben 2003) chosen production. To formalize the heuristic approach,

it is written down in an algorithmic way. These results cover the interfaces by describing the dependencies and make thus an easy implementation in the future possible. Note that for the production plan optimization not only the minimization of energy, but also of time, costs and raw material usage may be suitable goals.

Apart from this, another useful quality function is the overall mean variance of the energy consumption. A small overall variance means a balanced and thus smooth time dependent energy consumption avoiding surplus heating and cooling. Hence, by smoothing the energy demand with respect to the capacity utilization rate, product fragmentation and peaks in throughput and energy consumption can be avoided (Martin et al. 2008). This means that in some dairies for example steam generators could be removed, which prior to that were needed to supply energy during peaks. Moreover, some system components have a higher efficiency for a specific production level. Thus applying the production plan methods helps to develop a suitable system design. The method which will be later used to implement the algorithm is the binary integer programming. The idea is to rewrite the dependencies in matrices to achieve the form which can be solved using binary integer programming. In this work the binary integer programming is not discussed since it is only a different way of representing the same problem and to solve it with a different algorithmic approach.

RESULTS

Production plan analysis

As a first step the production plan was analyzed using the defined key indicators capacity utilizing rate and throughput. For each day of a two-week period those indicators were calculated to compare the production days. The results are depicted in table 2. Note that the presentation of the results asks for a product specific measure for the variance of the capacity utilizing rate, which is currently not available due to lack of data. The range of the capacity utilizing rate of the whole period is between 98 % and 42 %. This indicator is rather wide spread. The means are for both weeks about 78 %. With a value of 21 %, the second week shows the double standard deviation of the first week. It is also reasonable to assume that an overall higher capacity utilizing rate is possible since for some days a value of more than 95 % was observed.

Hence, already at this point it is obvious, that the production plan has a high optimization potential regarding the capacity utilizing rate. On the other hand, the capacity utilizing rate does not have a direct impact on the energy usage, but it is only indirectly connected to the energy consumption of the process. With a higher capacity utilizing rate the idle time is reduced and therefore the fixed energy consumption can be utilized more

efficiently.

Weekday	Utilization rate		Throughput	
	1. week [%]	2. week [%]	1. week [kg/min]	2. week [kg/min]
Monday	70	98	297	265
Tuesday	84	76	237	548
Wednesday	68	59	206	195
Thursday	74	74	224	247
Friday	96	95	309	356
Saturday	86	97	314	317
Sunday	74	42	132	253
Mean	79	77	246	312
Deviation	10	21	66	125

Table 2: Capacity utilization rate and throughput for two subsequent weeks recorded in the dairy under study

The throughput of the unit is in the range between 132 kg/min and 548 kg/min. The standard deviation of the first week is with 65kg/min considerably lower than the standard deviation of the second week.

Analysis of network systems

To give an overview for the energy analysis a sequencer Sankey diagram, see figure 4, is used to visualize the mass and energy flows in the system (Hesselbach 2012). The dark grey colored streams are used for the mass flow and the light grey for the energy. Note that the width of the edges is proportional to the energy or mass that is transported (Schmidt (2006)). However, the sequencer Sankey diagram is only depicting energy and product flows as well as the basic structure of the process dependencies and thus it is incomplete in the sense of mass and energy conservation. The reason is that due to the consistency with the network block diagrams only the relevant energy and mass flows are considered since later for the optimization the focus is on the dependencies and the step enabling conditions and so the use of network block diagrams is feasible. This doesn't mean that the Sankey diagram is not viable, but both the network block diagram and the Sankey diagram are showing different aspects of the system. Therefore, for a detailed analysis both diagrams are needed.

In figure 5 the step enabling condition is the time. The legend of the block used in sequencer diagram is shown in the following table 3. Here for the production of the yoghurt both milk and cream are needed. Hence, considering the times of each discrete process step the whole system will be delayed if one of those ingredients is missing.

Since the time needed for the cream production is approximately 29+17 minutes compared to just 4 minutes for the milk, the critical path of this production is the cream. Appropriate methods for storing the cream will speed up the production.

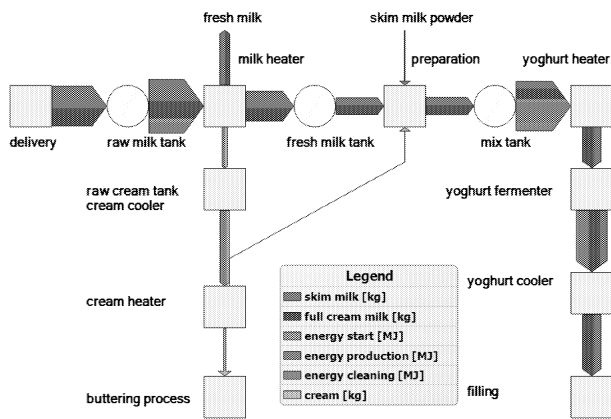


Figure 4: Sequencer Sankey diagram for process

Earliest start	Longest duration	Earliest stop
Name		
Latest start	Buffer time	Latest stop

Table 3: Legend of one block in the network

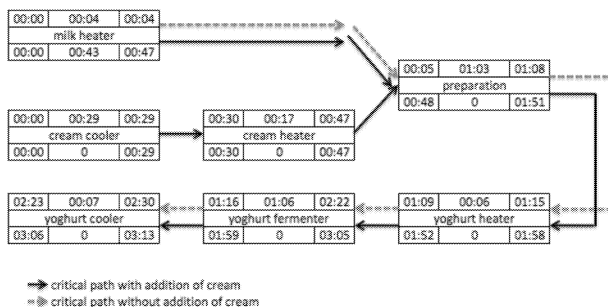


Figure 5: Network block diagram with critical paths

Note that for different products the critical paths might change. For the reduction of both the idle times and the number of starting and cleaning processes there are basically two possible approaches. The first is optimizing the intra day distribution of the production, the second from a more management orientated view will be discussed later. For the first approach the Gantt chart is a suitable visualization. In the first line of figure 6 (labelled 03/07/11) a fragmentation of milk (black) can be detected. It would be more energy efficient to process the milk without interrupts to reduce starting and cleaning processes. Besides, the time schedule of the production appears to be rather random with no clear pattern comparing the different days of one week. Therefore, it can be stated that there is an optimization potential which can be exploited by distributing the production more equally over the whole week as well as by merging processing sequences of the same product.

The alternative is a more general approach to look a specific schedule of a weekly production and shift production between different days. The main difference is

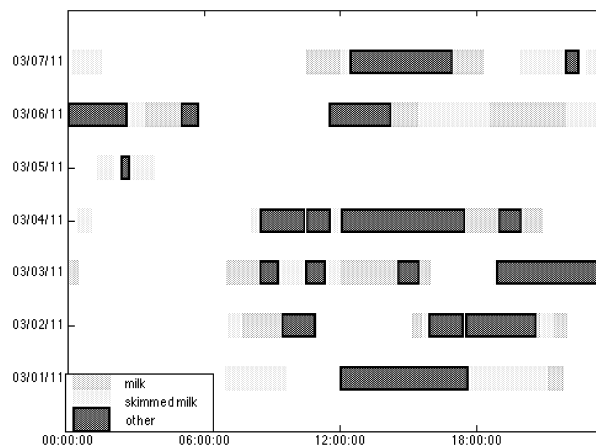


Figure 6: Gantt chart of the temporal analysis on a daily basis

that for the more general approach the daily structure is not considered. Moreover, only the total production quantities per day and not the intra-day distribution regarding the time are taken into account. The goal is to smoothen the production level on a weekly base. The second point of view is to consider only the total amount of product per day and neglecting the temporal distribution of one day. As an example for the second optimization approach a Gantt chart with product units produced per day is shown in figure 7. It depicts the specified amounts for daily production and thus the total amounts of product per week. The different colors are used for different products. As it can be seen easily, the production is also fragmented on a weekly basis. Like shown below (figure 7) it can be recognized that some rather short production periods could be moved to a different day reducing the fragmentation of the production. Hence, there might be problems because of delivery deadlines or buffer tank capacity. Both are taken into account wherever possible. The lack of data makes a full description of deadlines and buffer tanks almost impossible. However this lack of data is compensated by adding expert knowledge. Furthermore, the quantity of the production on a weekly base is varying. Hence, the production quantities could be smoothed over the weekdays to achieve a similar energy consumption for all weekdays. As a result, the energy which needs to be provided would be more balanced on a weekly base keeping in mind that Friday and Saturday might be exceptions because of different consumer behavior at weekends or weekly cleaning.

Pseudo-code optimization

For the optimization an algorithm using pseudo-code syntax has been developed which has a given production plan as an input and an optimized production plan as output. The algorithm uses the constraints which

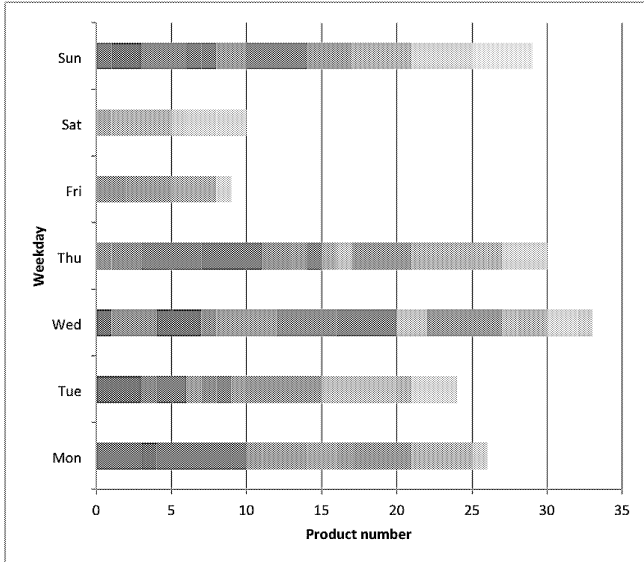


Figure 7: Gantt chart with product units on a weekly basis (each product in a different grey scale)

have been discovered in the production plan analysis. The use of pseudo-code is a convenient way to describe the optimization steps of the algorithm formally. Below there is an exemplary pseudo-code of the algorithm which is reducing the fragmentation of the production and at the same time it is reducing the idle times as well as energy by avoiding not necessary starting and cleaning processes.

Algorithm 1 Production plan optimization

Require: prodplan (day, milk heater, milk1)

- 1: **for all** element in prodplan(day) **do**
- 2: **if** element \neq milk1 **then**
- 3: **function** SEARCH(milk1, prodplan(day))
- 4: success = 0
- 5: **if** milk1 found in prodplan(day) **then**
- 6: success = 1
- 7: **end if**
- 8: **end function**
- 9: **if** success = 1 **then**
- 10: **function** SWAP(element,milk1)
- 11: **end function**
- 12: **end if**
- 13: **end if**
- 14: **end for**

The pseudo-code above has to be read as follows:

- Take the production plan from a given day for a specific unit and product.
- Check whether the specified product is on the production plan for that day
 - If so, search for the next occurrence that day
 - * If search succeeded, swap the found element with the initial

The effect of the changes for one product is, that the production periods of a chosen product are merged and thus the fragmentation on a daily base is lowered. The table 4 shows the fragmentation as a criterion. The fragmentation of an observed production plan is compared to an optimized production plan that has been obtained by applying the merging strategy as outlined above heuristically in pseudo-code for all products. It can be observed that the average of the fragmentation after the optimization is 10 % and was raising from the initial value of 42 %. This has also an impact on the energy usage since additional cleaning and starting processes can be avoided. Note that the optimized production plan might not always be usable due to constrains as mentioned above.

	Fragmentation [%] real-world	Fragmentation [%] simulated
Monday	41	19
Tuesday	45	0
Wednesday	37	16
Thursday	56	0
Friday	44	0
Saturday	50	31
Sunday	34	3
Mean	42	19

Table 4: Fragmentation benchmark before and after optimization

Table 5 shows that based on real-world production plans the energy consumption of the yoghurt-processing production line can be in average reduced by 314kWh/day (considering the energy consumption of the processes mentioned in the introduction, figure 1) using the described algorithm to lower the product fragmentation. The energy used for the starting process is reduced for 22%. The energy for the cleaning process is reduced by 7%. The energy which is used for the production has not been reduced in this scenario. However there might be less raw material losses which could not be measured. In total the thermal energy consumption is reduced by 3%. This may appear small, but it must be pointed out, that, apart from an analysis of available data, neither additional expenses nor additional equipment are necessary. Furthermore, the production plan optimization yields also indirect optimization effects. For example, the production rate as well as the used energy is distributed more equally in the whole system and the system is driven mainly at the same production and energy level.

Keeping in mind that the efficiency for each system is dependent on the production rate, an equally distributed production will be helpful if the system is designed correctly to keep the efficiency at a high level and may, as a consequence, also lead to lower aging and wearing of the equipment. As mentioned above, the optimized

Thermal energy	real-world [kW/day]	simulated [kW/day]
start	906	703
production	8943	8943
cleaning	1489	1378
total	11338	11024

Table 5: Energy consumption of real-world and simulated production

production plan might not be usable due to others, not yet considered constraints. However, it points out weaknesses of the current production plan and it can be used as a suggestion for further improvements.

DISCUSSION/CONCLUSIONS

With regard to rising cost for resources and energy in the future, the aim of this work is to show ways to increase the efficiency of the yoghurt production process and moreover to save material, time and energy.

With the help of Gantt charts the processes and their workflow could also be considered time dependent. Thereby possible overlapping or short pauses between identical products as well as savings of start-up or cleaning processes can be identified. The critical path analysis was used to obtain the total processing time required for a product. With the help of the analysis methods, which have been discussed, weaknesses of an existent production plans could be discovered.

The introduction of pseudo-code algorithms has additionally given the possibility of developing abstract optimization methods for an existent production plan that not only detect weaknesses but also suggest an optimized production plan. Exemplarily by applying the algorithm to an existent production plan the product fragmentation could be lowered. This yields a reduction of the starting as well as the cleaning processes and thus the energy consumption.

A further step of this approach could be the integration in a manufacturing execution system. This would result in a better linkage between the needed data and the optimization methods shown in this approach. A more detailed approach would also include reductions in product losses as created by reductions of starting and stopping procedures. To achieve this goal, the database has still to be improved by gathering more related data from the production of our industrial partners.

Note that the presented methodological approach in the framework of a dairy can also be applied to all kind of production processes with strong dependencies. Summarizing, the presented approach shows applicable ways for process industries to increase the energy efficiency and points out the necessity of the consistent collection of production plan data.

The work is funded by the Bayrisches Staatsministerium für Wissenschaft, Forschung und Kunst in the Foreta program.

REFERENCES

- Altrogge G., 1994. *Netzplantechnik*. Oldenbourg, München; Wien.
- Elfner P. and Verein Deutscher Ingenieure and Universität Kaiserslautern, 1998. *Ein Beitrag zur Effizienzsteigerung der Datenanalyse und-aufbereitung für Simulationssysteme*. Fortschritt-Berichte // VDI. VDI-Verlag.
- Franke S.; Höfler J.; Osterroth I.; Voigt T.; Langowski H.C.; and Petermeier H., 2012. *Simulation based Energy Management Tools for the Food Processing Industry*. Submitted.
- Hesselbach J., 2012. *Energie- Und Klimageeffiziente Produktion: Grundlagen, Leitlinien Und Praxisbeispiele*. Vieweg Praxiswissen. VIEWEG.
- Junge M., 2007. *Simulationsgestützte Entwicklung und Optimierung einer energieeffizienten Produktionssteuerung*. Kassel University Press.
- Kessler H., 1988. *Lebensmittel-Verfahrenstechnik, Schwerpunkt Molkereitechnologie*. Kessler.
- Kletti J., 2005. *MES- Manufacturing Execution System: Moderne Informationstechnologie zur Prozessfähigkeit der Wertschöpfung*. VDI-Buch. Springer.
- Martin L.; Hesselbach J.; Thiede S.; Herrmann C.; Lüdemann B.; and Detzer R., 2008. *Energieeffizienz durch optimierte Abstimmung zwischen Produktion und technischer Gebäudeausrüstung. GI eV, Arbeitsgemeinschaft Simulation in der (Herausgeber): ASIM*.
- Schmidt M., 2006. *Der Einsatz von Sankey-Diagrammen im Stoffstrommanagement*. Beiträge der Hochschule Pforzheim. Hochsch. Pforzheim.
- Schwarze J., 2006. *Projektmanagement mit Netzplantechnik*. NWB-Studienbücher Wirtschaftswissenschaften. Verlag Neue Wirtschafts-Briefe.
- Siedersleben J., 2003. *Softwaretechnik: Praxiswissen für Softwareingenieure*. Software, design & management. Hanser.
- Unbehauen H., 2008. *Regelungstechnik I: Klassische Verfahren Zur Analyse Und Synthese Linearer Kontinuierlicher Regelsysteme, Fuzzy-Regelsysteme*. Studium Technik. Vieweg+Teubner Verlag.

EFFECT OF ELECTRON BEAM IRRADIATION DOSES IN ANTIOXIDANT ACTIVITY AND PHENOLICS CONTENT OF PORTUGUESE CHESTNUTS

Márcio Carocho¹

Lillian Barros¹

Albino Bento¹

Isabel C.F.R. Ferreira¹

¹CIMO-ESA - Instituto Politécnico de Bragança, Portugal;
Email:iferreira@ipb.pt

Amílcar L. Antonio^{1,2,3}

²GTRPP/Unidade de Física e Aceleradores, ITN, Sacavém, Portugal.

³Departamento de Física Fundamental, Universidad de Salamanca, Spain

Iwona Kaluska⁴

⁴Centre for Radiation Research and Technology, Institute of Nuclear Chemistry and Technology, Warsaw, Poland

KEYWORDS

Irradiated chestnuts, Electron beam irradiation, Antioxidant activity, Phenolics

ABSTRACT

The objective of this study was to analyse the effect of electron beam irradiation (0.5, 1 and 3 kGy) on the antioxidant activity of Portuguese chestnuts (*Castanea sativa* Mill.) using different *in vitro* assays, such as the 2,2-diphenyl-1-picrylhydrazyl (DPPH) radical-scavenging activity, reducing power, inhibition of β -carotene bleaching and inhibition of lipid peroxidation using thiobarbituric acid reactive species (TBARS). Total phenolics were determined by spectrophotometric assays. Irradiated samples seemed to preserve phenolics content and revealed higher antioxidant activity than the control sample. The most indicated dose to maintain antioxidants content, and to increase reducing power and lipid peroxidation inhibition was 1 kGy.

INTRODUCTION

Sweet chestnut (*Castanea sativa* Mill.) woodland covers more than 2.5 million hectares in Europe, with a distribution area ranging from the Southern Mediterranean to Central, Atlantic and Eastern Europe (Díaz-Varela et al. 2011). Portugal is one of the most important chestnut producers with nearly 25% of European production. Trás-os-Montes region represents 75.8% of Portuguese chestnut crops and 84.9% of chestnut orchards area (23,338 ha). The best development conditions are found at altitudes higher than 500 m and winter low temperatures, as in the “Terra Fria Transmontana” region (Northeast of Portugal) in which 12,500 ha are used for chestnut cultivation. Due to the high economic value of chestnuts, it is important to develop conservation methodologies that allow the complete maintenance of their properties and also to fulfil the phytosanitary international regulations for exported products. The previously applied methods included mainly low temperature, controlled atmosphere storage and fumigation with methyl bromide (MeBr) for insect disinfestation. Methyl bromide was the most widely used fumigant for chestnuts post-harvest disinfestation, but induces the depletion of the ozone layer and has deleterious effects on health, so it was banned after the Montreal Protocol. In the European Union its use is forbidden since March 2010. Other conservation techniques such as hot

water dip, still represent low efficiency, affect chemical composition and may induce mould growth. Irradiation may represent a breakthrough on this issue, since it has been used with promising results (Antonio et al. 2011; Fernandes et al. 2011; Kwon et al. 2004). As far as we know, electron beam irradiation was only tried on chestnuts once, aiming to kill larvae (Todoriki et al. 2006). Electron beam radiation might be a clean, environment friendly, comparatively cheap procedure and an effective phytosanitary treatment. Nevertheless, it must be studied in detail since results may vary with fruit species, exposure time and beam intensity.

Chestnuts are important sources of polyphenolic antioxidants that have high free radical scavenging properties being associated to protective effects against coronary heart disease, cancer, neurodegenerative diseases and osteoporosis. Our research group has already determined the antioxidant properties of non-irradiated *Castanea sativa* Mill. (Barreira et al. 2008) and in samples exposed to gamma-radiation (Antonio et al. 2011).

Herein, we describe the influence of the electron beam irradiation process (at three different doses 0.5, 1 and 3 kGy) in antioxidant properties (radical-scavenging activity, reducing power, inhibition of β -carotene bleaching and inhibition of lipid peroxidation using thiobarbituric acid reactive species) and phenolics content of chestnuts immediately after irradiation.

MATERIALS AND METHODS

Samples and samples irradiation

Chestnuts samples (*Castanea sativa* Mill., Judia variety) were obtained directly from a local producer of Trás-os-Montes, Northeast of Portugal. They were divided in four groups to be exposed to different radiation doses (0, 0.5, 1 and 3 kGy) with 27 units per group (about 0.5 kg) placed into polyethylene plastic bags, being 0 kGy the non-irradiated, control samples. To estimate the dose during the irradiation process three types of dosimeters were used. A standard dosimeter, a graphite calorimeter, and two routine Gammachrome YR and Amber Perspex dosimeters, from Harwell company (U.K.).

After irradiation, 3 fruits from each group were separated from the skins and lyophilized (Labconco, FreeZone, Missouri, USA), reduced to a fine dried powder (20 mesh), and mixed to obtain a homogenate sample and analyzed.

Antioxidant activity assays

The sample (1.0 g) was extracted twice with methanol (30 mL) for 1 h. After filtration and evaporation of the methanol, the extracts were re-dissolved in methanol at a concentration of 50 mg/mL and analysed for phenolics and flavonoids content, DPPH (2,2-diphenyl-1-picrylhydrazyl) radical-scavenging activity, reducing power inhibition of β -carotene bleaching and inhibition of lipid peroxidation using thiobarbituric acid reactive species.

Determination of antioxidants content

For phenolics, an aliquot of the extract solution (0.5 mL) was mixed with *Folin-Ciocalteu* reagent (5 mL, previously diluted with water 1:10 v/v) and sodium carbonate (75 g/L, 4 mL). The tubes were vortexed for 15 s and allowed to stand for 30 min at 40 °C for colour development. Absorbance was then measured at 765 nm (AnalytikJena 200 spectrophotometer). Gallic acid was used to calculate the standard curve ($9.4 \times 10^{-3} - 1.5 \times 10^{-1}$ mg/mL), and the results were expressed as mg of gallic acid equivalents (GAE) per g of extract.

DPPH radical scavenging activity

This methodology was performed using an ELX800 Microplate Reader (Bio-Tek Instruments, Inc.). The reaction mixture in each one of the 96-wells consisted of one of the different concentrations of the extracts (30 μ L) and aqueous methanolic solution (80:20 v/v, 270 μ L) containing DPPH radicals (6×10^{-5} mol/L). The mixture was left to stand for 30 min in the dark. The reduction of the DPPH radical was determined by measuring the absorption at 515 nm. The radical-scavenging activity (RSA) was calculated as a percentage of DPPH discoloration using the equation: % RSA = $[(A_{\text{DPPH}} - A_{\text{S}}) / A_{\text{DPPH}}] \times 100$, where A_{S} is the absorbance of the solution when the sample extract has been added at a particular level and A_{DPPH} is the absorbance of the DPPH solution.

Reducing power

The different concentrations of the extracts (0.5 mL) were mixed with sodium phosphate buffer (200 mmol/L, pH 6.6, 0.5 mL) and potassium ferricyanide (1% w/v, 0.5 mL). The mixture was incubated at 50 °C for 20 min, and trichloroacetic acid (10% w/v, 0.5 mL) was added. The mixture (0.8 mL) was poured in the 48 wells, as also deionised water (0.8 mL) and ferric chloride (0.1% w/v, 0.16 mL), and the absorbance was measured at 690 nm in the Microplate Reader described above.

Inhibition of β -carotene bleaching

A solution of β -carotene was prepared by dissolving this compound (2 mg) in chloroform (10 mL). Two mL of this solution were pipetted into a round bottom flask. After the chloroform was removed at 40 °C under vacuum, linoleic acid (40 mg), Tween 80 emulsifier (400 mg), and distilled

water (100 mL) were added to the flask with vigorous shaking. Aliquots (4.8 mL) of this emulsion were transferred into different test tubes containing different concentrations of the extracts (0.2 mL). The tubes were shaken and incubated at 50 °C in a water bath. As soon as the emulsion was added to each tube, the zero time absorbance was measured at 470 nm. β -carotene bleaching inhibition was calculated using the following equation: (Absorbance after 2 h of assay/Initial Absorbance) \times 100.

Inhibition of lipid peroxidation using thiobarbituric acid reactive species

Porcine (*Sus scrofa*) brains were obtained from officially slaughtered animals, dissected, and homogenized with a Polytron in ice cold Tris-HCl buffer (20 mM, pH 7.4) to produce a 1:2 (w/v) brain tissue homogenate which was centrifuged at 3000 g for 10 min. An aliquot (0.1 mL) of the supernatant was incubated with the different concentrations of the sample solutions (0.2 mL) in the presence of FeSO₄ (10 mM; 0.1 mL) and ascorbic acid (0.1 mM; 0.1 mL) at 37 °C for 1 h. The reaction was stopped by the addition of trichloroacetic acid (28%, w/v, 0.5 mL), followed by thiobarbituric acid (TBA, 2%, w/v, 0.38 mL), and the mixture was then heated at 80 °C for 20 min. After centrifugation at 3000g for 10 min to remove the precipitated protein, the colour intensity of the malondialdehyde (MDA)-TBA complex in the supernatant was measured by its absorbance at 532 nm. The inhibition ratio (%) was calculated using the following formula: inhibition ratio (%) = $[(A - B) / A] \times 100\%$, where A and B were the absorbance of the control and the sample solution, respectively.

Statistical analysis

Three replicates of each sample were used and all the assays were carried out in triplicate. The results are expressed as mean values and standard deviation (SD). The results were analyzed using one-way analysis of variance (ANOVA) followed by Tukey's HSD Test with $\alpha = 0.05$. This analysis was carried out using SPSS v. 18.0 program.

RESULTS AND DISCUSSION

Irradiated samples seemed to preserve phenolics since these samples present higher concentrations of the mentioned compounds than the control sample (non-irradiated) (Table 1). Moreover, all the irradiated samples (0.5, 1 and 3 kGy) revealed higher antioxidant activity (lower EC₅₀ values) than control sample in all the assayed methods. The most indicated dose to maintain antioxidants content, and to increase reducing power and lipid peroxidation inhibition was 1 kGy. It was possible to correlate DPPH scavenging activity and reducing power with phenolics content ($R^2=0.5607$ and 0.9138 , respectively). Nevertheless, these antioxidants are not correlated with the results obtained using lipid peroxidation inhibition assays (β -carotene bleaching inhibition and TBARS assays, Table 2, $R^2 < 0.45$). This could be due to the lipidic environment in which these methods take place. Therefore, other

antioxidants rather than phenolics are certainly responsible for the antioxidant activity observed.

Table1. Antioxidant activity (EC₅₀ values^a) and phenolics content in irradiated and non-irradiated chestnuts.

	EC	E 0.5	E 1	E3
Phenolics (mg GAE/g extract)	3.61 ± 0.57 ^d	4.06 ± 0.93 ^c	8.16 ± 0.34 ^a	5.60 ± 0.50 ^b
Flavonoids (mg CE/g extract)	2.34 ± 0.25 ^a	0.40 ± 0.05 ^b	0.31 ± 0.06 ^c	0.24 ± 0.06 ^c
DPPH scavenging activity (mg/ml)	25.12 ± 1.11 ^a	23.27 ± 2.61 ^b	15.93 ± 0.71 ^c	13.81 ± 1.67 ^d
Reducing power (mg/ml)	7.05 ± 0.96 ^a	6.31 ± 0.59 ^b	2.81 ± 0.10 ^d	5.36 ± 0.27 ^c
β-carotene bleaching inhibition (mg/ml)	6.00 ± 0.43 ^b	2.54 ± 0.37 ^c	1.94 ± 0.20 ^d	6.95 ± 1.09 ^a
TBARS inhibition (mg/ml)	10.63 ± 1.72 ^a	4.06 ± 1.28 ^c	1.66 ± 0.41 ^d	7.82 ± 2.77 ^b

^a EC₅₀: Extract concentration corresponding to 50% of antioxidant activity (for DPPH, β-carotene linoleate and TBARS assays) or 0.5 of absorbance (for reducing power assay).

Table2. Correlations established between phenolics and antioxidant activity EC₅₀ values of irradiated and non-irradiated chestnuts.

	EC ₅₀ value (mg/ml)	Phenolics (mg GAE/g)	Flavonoids (mg CE/g)
DPPH scavengin g activity	Linear equation	Y=- 0.2793x+10.811	Y=0.1151x-0.429
	R ²	0.5607	0.4290
Reducing power	Linear equation	Y=- 1.0581x+11.051	Y=0.2956x-0.7705
	R ²	0.9138	0.3211
β-carotene bleaching inhibition	Linear equation	Y=- 0.3511x+6.8859	Y=0.1494x+0.169 6
	R ²	0.1747	0.1424
TBARS inhibition	Linear equation	Y=- 0.2988x+7.1625	Y=0.154x-0.1106
	R ²	0.3738	0.4472

CONCLUSIONS

Overall, irradiated samples seemed to preserve phenolics content and revealed higher antioxidant activity (lower EC₅₀ values) than the control sample. The most indicated dose to maintain antioxidants content, and to increase reducing power and lipid peroxidation inhibition was 1 kGy

ACKNOWLEDGEMENTS

ON.2/QREN/EU Project 13198/2010 financial support; FCT grants: SFRH/BPD/4609/2008 (L. Barros) SFRH/PROTEC/67398/2010 (A. Antonio). Prof. A. Chmielewski, Director of the Inst. Nuclear Chem. and Technol. Warsaw, Poland, for allowing e-beam irradiations.

REFERENCES

- Díaz-Varela R.; Álvarez P.; Varela E.; Iglesias S. 2011. "Prediction of Stand Quality Characteristics in Sweet Chestnut Forests in NW Spain by Combining Terrain Attributes, Spectral Textural Features and Landscape Metrics". *Forest Ecology and Management*, 261, 1962-1972.
- Antonio A.L.; Fernandes A.; Barreira, J.C.M.; Bento A.; Botelho, M.L.; Ferreira, I.C.F.R. 2011. "Influence of Gamma Irradiation in the Antioxidant Potential of Chestnuts (*Castanea sativa* Mill.) Fruits and Skins." *Food and Chemical Toxicology*. 49, 1918-1923.
- Fernandes, A.; Barreira, J.C.M.; António, A.; Bento, A.; Botelho, M.L.; Ferreira I.C.F.R. 2011. "Assessing the Effects of Gamma Irradiation and Storage Time in Energetic Value and in Major Individual Nutrients of Chestnuts." *Food and Chemical Toxicology*. 49, 2429-2432.
- Kwon, J.; Kwon, Y.; Byun, M.; Kim, K. 2004. "Competitiveness of Gamma Irradiation with Fumigation for Chestnuts Associated with Quarantine and Quality Security." *Radiation Physics and Chemistry*, 71, 41-44.
- Todoriki, S.; Hasan, M.; Miyanoshta, A.; Imamura, T.; Hayashi. T. 2006. "Assessment of Electron Beam-Induced DNA Damage in Larvae of Chestnut Weevil, *Curculio sikkimensis* (Heller) (Coleoptera: Curculionidae) Using Comet Assay." *Radiation Physics and Chemistry*, 75, 292-296.
- Barreira, J.C.M.; Ferreira, I.C.F.R.; Oliveira, M.B.P.P.; Pereira, J.A. "Antioxidant Activities of the Extracts from Chestnut Flower, Leaf, Skins and Fruit." 2008. *Food Chemistry*, 107, 1106-1113.

AUTHOR BIOGRAPHIES

MÁRCIO CAROCHO research interests are in chestnuts irradiation. E-mail: mcarocho@gmail.com

AMILCAR L. ANTONIO research interests are related to food irradiation. E-mail: amilcar@ipb.pt

LILIAN BARROS research interests are related to food chemistry. E-mail: lillian@ipb.pt

ALBINO BENTO research interests are related to pest control. E-mail: bento@ipb.pt

IWONA KALUSKA research interests are related to food and medical devices irradiation; dosimetry. E-mail: i.kaluska@ichtj.waw.pl

ISABEL C.F.R. FERREIRA research interests are related to food chemistry. E-mail: iferreira@ipb.pt

COMPARTMENT MODELLING IN DRYING OF GAMMA IRRADIATED CHESTNUT FRUITS

Amilcar L. Antonio^{1,2,3}

Elsa Ramalhosa¹

Albino Bento¹

¹CIMO-ESA - Instituto Politécnico de Bragança, Bragança, Portugal

E-mail: amilcar@ipb.pt

Mauro Trindade⁴

Guillermo Sanchez⁵

⁴Departamento de Radioterapia, Centro Hospitalar de Trás-os-Montes e Alto Douro, Vila Real, Portugal.

⁵ENUSA – Industrias Avanzadas S.A., Salamanca, Spain.

M. Luisa Botelho²

Begoña Quintana³

²GTRPP/Unidade de Física e Aceleradores, ITN, Sacavém, Portugal.

³Departamento de Física Fundamental, Universidad de Salamanca, Spain

KEYWORDS

Chestnut fruits; Gamma irradiation; Drying; Compartment modelling.

ABSTRACT

The main objective of this work was to understand how irradiation processing influences the drying of chestnut fruits. Herein, based on the fruit characteristics and Computational Tomography (CT) images, we proposed a compartment-model for the kinetic drying curves. The preliminary results seemed to indicate that one-compartment modelling gives good fitting results for the modelization of the drying curves. In this way, this model could be a good approach to the drying process.

INTRODUCTION

Food irradiation is a non-thermal processing technology for food preservation, to increase shelf-life, for disinfection (insects elimination) or sterilization. Irradiation appears in chestnut fruits as a possible phytosanitary treatment, to meet the international trade laws, without affecting significantly the nutritional value (Antonio et al. 2011; Fernandes et al. 2011; Kwon et al. 2004). In these fruits one of the main problems is water loss, causing loss of weight, with changes of some physical characteristics, like texture, affecting the incomes of the producers. Otherwise, the drying itself is another food industry process available to obtain other sub-products, like flour for cooking and for bakery products. In this way, understanding how irradiation processing influences the drying of this fruit is an important goal.

Herein, based on the fruit characteristics and Computational Tomography (CT) images, we proposed an alternative approach, compartment-modelling for the drying kinetics. This kind of modelization is used in different areas, namely in pharmacokinetics for modeling drugs administration in the human body (Sanchez 2007). This modelization consists in dividing the human body, seen here as the sample, in compartments that interact between each other transferring matter, in this case water.

Herein, we had considered the initial concentration of water in the fruit similar as one intake of a drug.

MATERIALS AND METHODS

Samples

Chestnuts samples (*Castanea sativa* Mill., Judia variety) were obtained directly from a local producer of Trás-os-Montes, in the northeast of Portugal. They were divided in four groups to be exposed to different radiation doses (0, 1, 3 and 6 kGy) with 27 units per group (about 0.5 kg) placed into polyethylene bags, being 0 kGy the non-irradiated samples (control).

Irradiations

The irradiation of the samples were performed in a Co-60 experimental chamber with four sources, with a total activity of 267 TBq (6.35 kCi) in November 2011. The dose rate for the positions of irradiation was estimated using an ionization chamber dosimeter (model FC60-P, from IBA dosimetry company). During the irradiation processing 4 routine dosimeters were used for each group, in the corners of the sample bag (Amber Perspex dosimeters, from Harwell company, U.K.). The samples were rotated up side down (180°) at half of the time, to increase the dose uniformity. The dosimeters were read in a UV-VIS Spectrophotometer (model Specord 200, from Analytik Jena) at 603 nm, two readings for each, to estimate the dose according to a previous calibration curve.

Drying process

In order to determine the moisture contents of chestnuts subjected to different irradiation doses, three chestnuts from each group were triturated and dried in an oven at 105 °C till constant mass. Another group of samples (four for each dose) were dried in an air forced oven at 50 °C measuring the fruits mass along time, till 29 h (Fig. 1).

The water content per dry matter (W) is

$$W = (\text{mass of water}) / (\text{mass of dry matter}) \quad (1)$$



Fig. 1: Chestnut samples used in the present work.

Modelization

To model the drying of the fruits, a one-compartment model was used (Fig. 2), that interacts with the exterior transferring matter, in this case water. The initial water content in the fruit, b_0 , was considered similar as one intake of a “drug” and its behaviour along the time (drying process), corresponded to the water loss by the fruit. The equation that describes this model is

$$dq_1(t) / dt = -k_{10} q_1(t) \quad (2)$$

The k_{10} , elimination constant, is the transferring coefficient from the compartment 1 (fruit) to compartment 0 (outside).

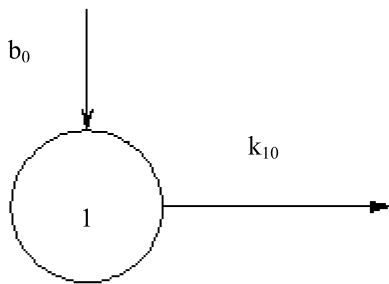


Fig. 2: One-compartment model.

The solution of this equation, used for fitting the drying process is:

$$q_1(t) = b_0 e^{-k_{10} t} \quad (3)$$

For determining the elimination constant, k_{10} , for each group of samples the *Mathematica* software was used, version 8 (from Wolfram company).

Computed tomography (CT) images

CT images of the fruit were taken in a Philips machine (model Brilliance CT Big Bore, from the Philips company), at 120 kV, 50 mA and 2.1 seconds of exposition.

RESULTS AND DISCUSSION

The estimated doses, after photometric reading of the dosimeters, were 1.0 ± 0.1 , 3.2 ± 0.7 , 6.3 ± 0.9 kGy.

For simplicity, from now on, in the graphs we considered the values 1, 3 and 6 kGy.

The dose rate was 2.5 ± 0.1 kGy h^{-1} and the average dose uniformity ratio (D_{max}/D_{min}) was 1.4 ± 0.3 .

As could be seen from the CT images the fruit had some inhomogeneities, inner and outer skins, and some inside heterogeneity (Fig. 3).

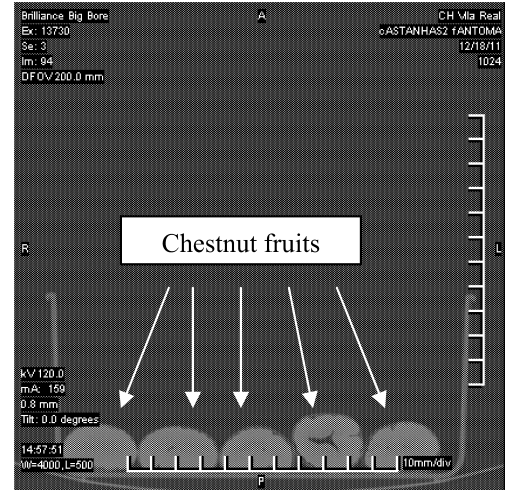


Fig. 3: Computed tomography image of chestnut fruits.

Good fits with the one-compartment model were obtained, with R squared values higher than 0.996 (Fig.4).

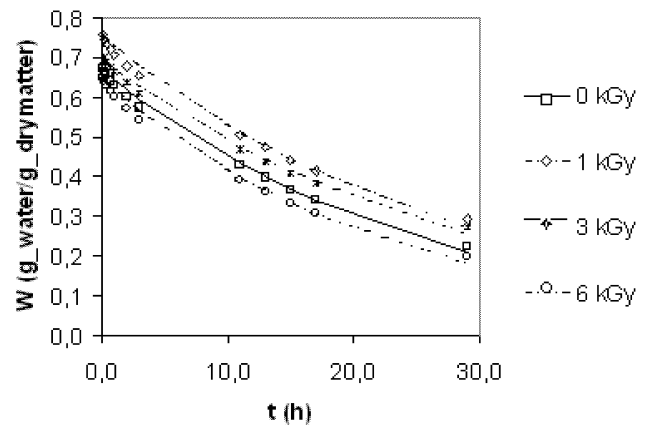


Fig. 4: Drying experimental data and fitting curves for one-compartment model.

The drying curves for the different doses followed a similar behavior, including control (non-irradiated samples).

CONCLUSIONS

The drying curves for the irradiated samples were similar to the non-irradiated chestnuts, up to 6 kGy. The results also indicated that one-compartment modelling gave a good description of drying process. In the near future we intend to compare these results with those obtained in a multi-compartment model, in order to take into account the inhomogeneities of this fruit.

ACKNOWLEDGEMENTS

ON.2-QREN-EU Project nº 13198/2010 for financial support; A.L. Antonio grant SFRH/PROTEC/67398/2010. Dr. Carlos Vaz, General Director of Centro Hospitalar de Trás-os-Montes e Alto Douro, for allowing CT images.

REFERENCES

- Antonio A.L.; Fernandes A.; Barreira, J.C.M.; Bento A.; Botelho, M.L.; Ferreira, I.C.F.R. 2011. "Influence of Gamma Irradiation in the Antioxidant Potential of Chestnuts (*Castanea sativa* Mill.) Fruits and Skins." *Food and Chemical Toxicology*. 49, 1918-1923.
- Fernandes, A.; Barreira, J.C.M.; Antonio, A.L.; Bento, A.; Botelho, M.L.; Ferreira I.C.F.R. 2011. "Assessing the Effects of Gamma Irradiation and Storage Time in Energetic Value and in Major Individual Nutrients of Chestnuts." *Food and Chemical Toxicology*. 49, 2429-2432.
- Kwon, J.; Kwon, Y.; Byun, M.; Kim, K. 2004. "Competitiveness of Gamma Irradiation with Fumigation for Chestnuts Associated with Quarantine and Quality Security." *Radiation Physics and Chemistry*, 71, 41-44.
- Sanchez, G. 2007. "Fitting Bioassay Data and Performing Uncertainty Analysis With Biokmod". *Health Physics* 92(1), 64-72.

AUTHOR BIOGRAPHIES

AMILCAR L. ANTONIO research interests are related to food irradiation. E-mail: amilcar@ipb.pt

ELSA RAMALHOSA research interests are related to food engineering. E-mail: elsa@ipb.pt

ALBINO BENTO research interests are related to pest control. E-mail: bento@ipb.pt

MAURO TRINDADE research interests are related to different radiotherapy techniques and medical physics. E-mail: MAUROPT@chtmad.min-saude.pt

M. LUISA BOTELHO research interests are related with microbiology, ionizing radiation and development of radiation applications for industry: environment, healthcare, pharmaceutical and others. E-mail: mlb@itn.pt

GUILLERMO SANCHEZ research interests are related with Nuclear Safety, Health Physics, Radioprotection, Environmental and Radiological Engineering, Planning, and Computer Modelization. E-mail: guillermo@usal.es

BEGOÑA QUINTANA research interests are related with Radiation Protection mainly in the field of environmental surveillance, Monte-Carlo simulations and Gamma spectrometry with Ge detectors. E-mail: quintana@usal.es

FOOD CONTAMINATION AND SAFETY MEASURES

AFM1 EXPOSURE IN THE FRENCH POPULATION VIA MILK PRODUCTS CONSUMPTION USING MONTE CARLO SIMULATIONS

Nathalie Wesolek and Alain-Claude Roudot
LERCCO (Laboratoire d'évaluation du risque chimique pour le consommateur)
Université de Bretagne Occidentale
6 av Victor Le Gorgeu
29238 Brest, CS 93837,
France
E-mail : nathalie.wesolek@univ-brest.fr

KEYWORDS

Probability exposure, aflatoxin, distribution fitting, sampling.

ABSTRACT

Population exposure assessments to food contaminants are used to determine if there is a threat for human health. Exposure is calculated by multiplying for each individual the consumption by the contamination level and dividing by the body weight. Aflatoxin M1 exposure is calculated thanks to a probability method based upon the Monte Carlo technique. Contrarily to a deterministic approach, it enables to generate probability density functions of exposure levels. The Monte Carlo technique is used to estimate the effect of variability on the outputs of models which use a variety of input parameters. We found a mean exposure range of 0.02-0.03 ng/kg of body weight per day, with 95% of the population having an exposure level inferior to 0.07-0.09 ng/kg b.w./d.

INTRODUCTION

Aflatoxins may occur in concentrates, like cereal grains, as well as in silage, dairy cows are fed. These mycotoxins are mainly produced by two species of *Aspergillus* fungi: *A. flavus* and *A. parasiticus*. As ubiquitous fungi, they colonize plants in the field, mainly in tropical or subtropical regions, usually in case of drought. On the contrary, after harvest, they thrive in case food is not stored under dry conditions or when cereals are not properly dehydrated. After ingesting feed contaminated by Aflatoxin B1 (AFB1), cows excrete Aflatoxin M1 (AFM1) in their milk (Van Egmond, 1991; Wood, 1991). Raw milk is transformed into dairy products for human consumption which lead to human AFM1 exposure. The European and international bodies have not set an acceptable daily intake (ADI) for aflatoxins. These substances have genotoxic carcinogenic effects, with no threshold, and the only realistic approach is to reduce exposure to as low a level as possible following the ALARA (As Low As Reasonably Achievable) principle. In order to evaluate the AFM1 exposure of the French adult population, we chose to use the Monte Carlo technique. It consists of a simulation method enabling us to take into account the whole range of variability of the variables. The Monte Carlo technique is more and more used in food contaminant exposure assessment (see Leblanc *et al.* 2002 and Paulo *et al.*, 2005). It has been applied to exposure assessments of food additives too, as per example in Gilsenan *et al.* 2003.

The objective of this study is to compare two methods, which both use the Monte Carlo technique. The first method is based upon summarized consumption data per age group (with mean and standard deviation), whether the second one is carried out from individual raw consumption data. Another target is to observe whether a consumers' typology can be revealed thanks to individual raw consumption data.

DATA USED AND METHODS

Dairy Products Consumption Data Origin

Dairy products consumption data were provided by the second "Individual and National Study on Food Consumption", INCA2 survey carried out by the French Food Safety Agency, AFSSA (2009), now renamed ANSES. The study was conducted in three fieldwork phases between December 2005 and April 2007 in order to cover seasonal variations. There were 2,624 adults aged 18-79 years old included in the survey, on the basis of one adult per household. They had been selected using a three stage random probability design stratified by region of residence, size of urban area and anniversary date. Each respondent had to complete a seven-day food diary as well as other questionnaires on anthropometric and socioeconomic factors. The diary was filled in thanks to the book of photographs SUVIMAX which enabled the identification of food items and portion sizes. The dairy products content of compound foods (recipes, compound dishes) was evaluated. Only normal-reporters, i.e. individuals whose energy needs are covered by the declared consumptions, were considered for this study. Therefore a normal-reporter sample of 1,918 adults was used for the analysis. The ANSES calculated sampling weights for each surveyed individual, representing its frequency in the entire French population. This was achieved in order to ensure an appropriate sample's representativeness at a national level. We used both public data and raw data (personal communication) from the INCA2. We split raw data into the same categories as for public data: for each sex, consumers are classified into three age groups (18-34; 35-54; 55-79 years old). For raw data, the mean daily consumptions of each individual, who fulfilled the diary completely (7 days reporting), are calculated for each dairy food category, namely "Milk", "Cheese", "Other dairy products, butter excluded". For public data, for each sex and age group, global daily consumption values for each dairy food category are given

under the form of percentage of consumers, mean, standard deviation and median.

Consumers' Typology

Raw consumption data from the INCA2 are examined using discriminant function analysis in an attempt to improve separation between the age groups for each sex. This is achieved using Statgraphics Plus 5.1 software (StatPoint Inc.), after having transformed all consumption values into values corresponding to an individual at the average body weight of each group.

Aflatoxin M1 Contamination Data Origin

Contamination data used for AFM1 French contamination level of milk are official analysis data. Indeed, the DGCCRF (2005) achieved a French national monitoring plan in collaboration with the Ministry of Agriculture. However, due to the very high amount of censored data (below the Limit of Detection: LOD or the Limit of Quantification: LOQ), these results can not be used for distribution fitting. For this reason, a publication from Blanco *et al.* (1988) was used in order to fit a parametric distribution to AFM1 concentration in milk Probability Density Functions (PDFs). As Bakirci (2001) found no statistical differences between AFM1 contents of bulk milk, pasteurised milk, skim milk, and yoghurt manufactured at the same dairy plant, we considered that the two dairy food categories: "Milk", and "Other dairy products, butter excluded" have the same AFM1 level. Data for cheese contamination are derived from the data for milk, knowing that cheese is about three times more contaminated (per weight unit) than the milk it is made from (Rubio *et al.*, 2011; Cattaneo *et al.*, 2008).

Exposure Evaluation Principle

The basic model of exposure assessment calculated for each individual of the sampled panel is (Equation 1):

$$y_i = \frac{\sum_{k=1}^p (x_{ik} c_{ik})}{w_i} \quad (1)$$

Where y_i is the intake by individual i per day (in ng AFM1 per kg body weight per day), x_i is the consumption by individual i per day of the dairy food category k (in kg per day), c_{ik} is the concentration of AFM1 in commodity k eaten by individual i (in ng per kg) and w_i is the body weight of individual i (in kg). Finally, p is the number of dairy food categories considered. This theoretical calculation is usually not directly usable in practice due to the fact that we do not have contamination data for each specific food consumed by each individual. Food analysed only consist of a few samples because it appears that it is impossible to analyze each one of the foods consumed by each one of the individuals.

Monte Carlo Technique using @Risk

The @Risk software is a Monte Carlo software for risk analysis and risk assessment using Monte Carlo random simulations. It is used to determine how often specified events may occur thanks to the generation of Probability

Density Functions (PDFs). This probability risk analysis approach is opposed to the deterministic risk analysis calculation. Indeed, when achieving a deterministic risk evaluation, values are assigned for discrete scenarios to see what the outcome might be in each. Traditionally, this kind of evaluation, when applied to exposure assessment, has been done without regard for variability, that is, by multiplying average consumption by average concentration for all commodities. On the contrary, in a probability risk evaluation, values are given to all the possible scenarios, taking into account their probability of occurrence. It is used to estimate the effect of variability on the outputs of models which use a variety of input parameters. Monte Carlo simulation is the replication of a procedure with input data drawn randomly from a parametric distribution. However, Monte Carlo simulation can be used with two different sampling types under @Risk: the Monte Carlo (MC) and the Latin Hypercube (LH) sampling types. The LH sampling is a particular MC sampling: more precisely it is a constrained MC (i.e. random) sampling scheme, involving a stratification of the input distribution. For exposure assessment, the variables can be consumption and contamination levels. The constraint refers to the way each variable is sampled: the statistical cumulative distribution is split in n equally probable intervals on the cumulative probability scale, and then a random value is selected within each interval. The number of n equally probable interval is equal to the number of iterations of the Monte Carlo simulation. A simulation with 500 iterations, per example, would split the probability into 500 segments, each representing 0.2% of the total distribution. For the first segment, a number would be chosen between 0.0% and 0.2%. For the second segment, a number would be chosen between 0.2% and 0.4%. This number would be used to calculate the actual variable value based upon its distribution. Once each variable has been sampled using this method, a random grouping of variables is selected for each Monte Carlo calculation. Independent uniform selection is done on each of the variable's generated values. Each value must only be used once. LH sampling would create a more representative sampling of the distribution, ensuring that tail samples of the input distributions are drawn (e.g. for 1000 iterations, exactly one value above the P99.9 would be drawn, whereas for MC sampling either none, one or several samples may be drawn). So, LH sampling can be used to force the sampling of tails of distributions, along with a great number of iterations. This is why, in this study, thanks to the @Risk 5.7 software (Palisade Corp.), PDFs are modeled, using Monte Carlo simulations with 10,000 iterations under the LH sampling type.

Modelling of Exposure Assessment: Two methods

When achieving a Monte Carlo probability exposure assessment, the calculation of all possible exposure scenarios is enabled. These scenarios go from the lowest exposures with low consumers and low contaminations to the highest exposures with high consumers and high contaminations. This assessment gives exposure levels with their probabilities, thanks to calculations with @Risk. The objective of this exposure assessment study is to compare two calculation methods, both using the Monte Carlo technique. The first method consists of using consumption

public data published in the INCA2. Thus, combined consumptions of each dairy food category are not known. For this reason, exposure PDFs are calculated for each dairy food category, by multiplying consumption PDF by contamination PDF, further divided by the body weight PDF given by Tanguy *et al.* (2007) who calculated it from raw data from the INSEE (2002-2003). Then these exposure PDFs are added up, in order to obtain a global exposure PDF due to dairy products. These results have to be compared to the ones obtained thanks to another method using raw consumption data from the INCA2. With this second method, individual exposure PDFs are calculated by multiplying consumption values by contamination PDF, further divided by the body weight. Then the exposure PDFs for each food category are added, in order to obtain individual exposure PDFs due to total dairy products. The global exposure PDF for each individual is multiplied by its sampling weight. Finally, all the distributions are added up and divided by the sum of the sampling weights for each group considered. The result is an exposure PDF for the population group.

RESULTS

Consumers' Typology

Eigenvalues and canonical correlations are very small, suggesting that there is no possible further separation between the groups. This result is supported by the fact that when, for one sex and age group, consumptions of one dairy food category are plotted against consumption of another dairy food category, no correlations can be found.

Consumption Distribution Fitting

Consumption distribution fitting is only achieved for the first method of exposure calculation. Public consumption data from the INCA2 are fitted to parametric distributions. A key advantage of the use of parametric distributions is that they can provide estimates of the tails of a distribution beyond the range of observed values. This is of particular importance for food chemical exposure assessments which tend to focus on distribution tails. Furthermore, we choose to exclude the non-consumers of foods (which resulted in a large peak at zero). This is achieved in order to enhance the ability to fit a parametric distribution to food consumption data (Murray and Burmaster 1994; US EPA, 2000). In order to fit consumption excluding non-consumers, mean and SD (Standard Deviation) for each group and category are recalculated to correspond to the values for consumers only. More precisely, the SD of the population is decomposed, using the following formula of the variance (the SD being the square root of the variance s^2) and recalculated for consumers only with the same formula (Equation 2):

$$s^2 = \frac{\sum_{i=1}^n (x_i^2)}{n} - \left(\frac{\sum_{i=1}^n x_i}{n} \right)^2 \quad (2)$$

The PDF of food intake amongst consumers only is simulated with the corresponding mean consumption and SD as inputs of the lognormal distribution, using @Risk.

The choice of the lognormal distribution is made because it is classically used for food consumption modeling with right-skewed data. The distribution of the probability of being a consumer is a binomial distribution used to calculate the final PDF of food intake, using a conditional function. As the median obtained with the simulation is in good accordance with the one given in the survey, fitting is validated.

Contamination Distribution Fitting

The WHO (GEMS-Food Euro 1995) recommended, in case the level of censored data is at least equal to 60%, to calculate an Upper Bound (UB) value. Under the UB hypothesis, values inferior to the LOD, are placed at the LOD and the values between the LOD and the LOQ are put equal to the LOQ. So, when using the data from the DGCCRF, considering the UB hypothesis, the mean value amounts to 7.63 ng/L (SD equal to 7.14). Moreover, data from Blanco *et al.* were used to draw a PDF. The Kolmogorov-Smirnov test shows that the lognormal distribution can not be rejected at a 5% risk level. The lognormal distribution can be used hereafter for fitting AFM1 contamination data. The PDF for "Milk" or "Other dairy products, butter excluded" contamination is simulated with the UB mean contamination and SD values as inputs of the lognormal distribution, using @Risk. Furthermore, the PDF for "Cheese" is calculated by multiplying by three the PDF obtained for "Milk" with @Risk.

Modelling of Exposure Assessment: Two methods

The Monte Carlo technique applied to INCA2 public consumption data is called "Method No 1" whereas the same technique applied to raw data from the INCA2 is referred to as "Method No 2". Results, given in Table 1 enable to observe that the two methods are equivalent in our case. This strengthens our observations as regards consumers' typology results: quantities consumed for a dairy product as function of another dairy product are totally random. Such an observation might facilitate exposure assessments to other contaminants via dairy products consumption. Indeed, Method No 1, which is based upon consumption distributions for each dairy product category that are subsequently randomly associated in order to obtain exposure distributions due to the global dairy food consumption, is easier to carry out than Method No 2. Furthermore, results show that the AFM1 health risk is low for the adult population. We observe that the sex and age group having the highest exposure level is the one of women aged 35-54 years old. For this population category, the exposure PDF obtained thanks to Method No 1 is in Figure 1, whereas Figure 2 gives the distribution calculated via Method No 2.

Table 1: Exposure PDFs Values for Each Sex and Age Group: Comparison of the Two Methods (exposure values are given in ng of AFM1 per kg of body weight per day).

Method used	Exposure PDF values	Men [18-34]	Men [35-54]	Men [55-79]	Women [18-34]	Women [35-54]	Women [55-79]
Method No 1	Mean	0.0209	0.0285	0.0279	0.0213	0.0324	0.0299
	50 th Percentile	0.0105	0.0179	0.0181	0.0130	0.0228	0.0210
	95 th Percentile	0.074	0.090	0.084	0.0694	0.0928	0.085
	Mode	0	0	0	0	0	0
Method No 2	Mean	0.0301	0.0287	0.0286	0.0321	0.0331	0.0298
	50 th Percentile	0.0220	0.0209	0.0209	0.0234	0.0242	0.0218
	95 th Percentile	0.0809	0.077	0.077	0.086	0.0890	0.080
	Mode	0.0114	0.0112	0.0112	0.0125	0.0126	0.0113

DISCUSSION

Comparison to Data from the FTDS2

Exposure data obtained in this study can be compared to official exposure data for France reported in the FTDS2 (French Total Diet Study) by the ANSES (2011). The FTDS2 is based upon raw food consumption data from the INCA2, but specific analyses have been achieved to obtain contamination data. Each analysis result consisted of the contamination result of a composite sample. Each composite sample consisted of 15 samples joined together. Indeed, each sample bought at supermarkets was mixed in a composite sample representative of the consumption and shopping basket for the 8 inter-regions analyzed. There were 38 composite samples for milk, 17 for cheese and 14 for a mix of other dairy products (butter excluded). Such a sampling strategy drives to a dilution of the contamination, especially for contaminants found at a low incidence. However, it is recommended by the WHO for international comparisons in order to get general background levels as regards consumer exposures. In the FTDS2, the LOD was equal to 1 ng/kg for milk composite samples and 10 ng/kg for the other dairy composite samples. Due to low contamination levels, the amount of censored data (AFM1 undetected or not quantifiable) was equal to 100%. No positive samples were found (all values below the LOD), so, as recommended by the WHO (GEMS-Food Euro 1995), UB values were set at the LOD. The AFM1 exposure was calculated for each individual using the contamination value equal to the LOD and consumptions reported for each day. Then, the AFM1 exposure values of the population (mean and 95th percentile) were determined using the sampling weights corresponding to each individual. AFM1 exposure results for the adult population due to dairy products are the following: mean at 0.017 ng/kg b.w. per day and 95th Percentile inferior to 0.05 ng/kg b.w. per day. These results are slightly lower than the ones found in our study. Finally, the comparison of our results with the ones of the FTDS2 enables us to question the position which consists in mixing samples of different origins before analysis. This practice can cause dilution problems in low incidence contaminant cases, like AFM1, in lowering mean exposure. Furthermore, the relevance of the 95th Percentile is in question, as it is not going to reflect high consumer exposure due to high contamination levels but high consumer exposure due to medium contamination levels.

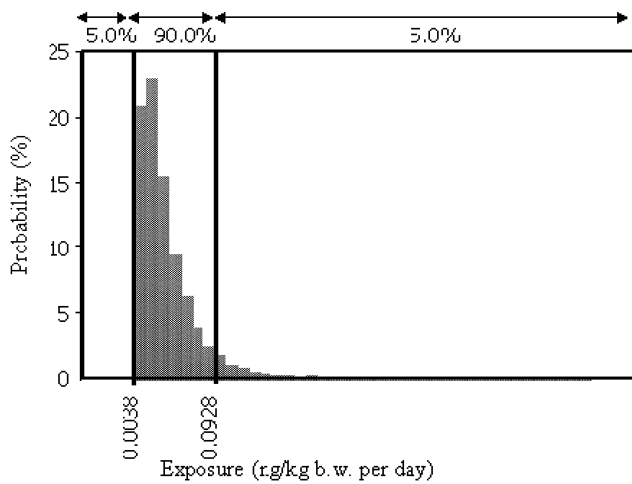


Figure 1: Exposure PDF for women aged 35-54 years old obtained via Method No 1

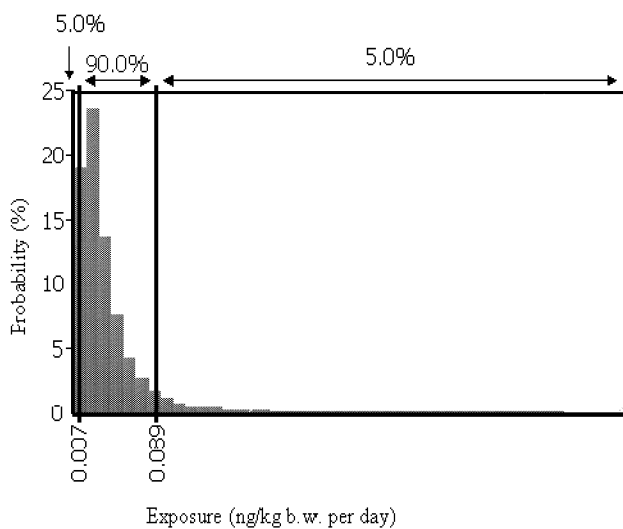


Figure 2: Exposure PDF for women aged 35-54 years old obtained via Method No 2

Relevance of Testing Only AFM1

As yet, Aflatoxin M1 has been considered to be the major metabolite excreted with milk in dairy cows. However, recent data show that Aflatoxicol (AFL) is also excreted in cow milk, as well as Aflatoxin B1 (Carvajal et al., 2003): 10% of samples taken in Mexico tested above 0.5 µg/L for AFM1, and 8% of samples were above 0.5 µg/L for AFL. AFL is a more potent toxin than AFM1, which can reconvert with AFM1 becoming AFL M1. So, AFM1 is the most abundant aflatoxin and the risk increases when the AFL contamination in milk is added.

CONCLUSION

Our results validate the use of the Monte Carlo technique upon consumption distribution data for each dairy food category. They thus show that it is not necessary to have raw individual consumption data, making in this way exposure calculations easier. However, it appears important to us to use contamination data for samples analyzed individually and not put together in case they do not come from the same batch. Furthermore, we observe that dairy products consumptions are random, that is to say that there is no link between consumptions of different dairy product categories. AFM1 exposure data for adults show that the values are rather low for the population, but it could be worth evaluating the exposure to other aflatoxins found in dairy products, such as aflatoxicol, in a future work. Indeed, the health risk might be preoccupying when AFL and AFM1 are considered together, so it could be interesting to evaluate this co-exposure.

REFERENCES

- Bakirci, I. (2001). A study on the occurrence of aflatoxin M1 in milk and milk products produced in Van province of Turkey. *Food Control*, Vol. 12, No. 1, p. 47-51
- Blanco, J.L., Domínguez, L., Gómez-Lucía, E., Garayzabal, J.F., García, J.A., Suárez, G. (1988). Presence of aflatoxin M1 in commercial ultra-high-temperature-treated milk. *Applied and Environmental Microbiology*, Vol. 54, No. 6, p. 1622-1623.
- Carvajal, M., Rojo, F., Mendez, I., Bolanos, A. (2003). Aflatoxin B1 and its interconverting metabolite aflatoxicol in milk: the situation in Mexico. *Food Additives and Contaminants* 20: 1077-1086
- Cattaneo, T.M.P., Monti, L., Panarelli, E.V., Francolino, S., Bertuzzi, T., Pietri, A. (2008). Fate of aflatoxin M1 during production and storage of crescenza cheese. *Italian Journal of Food Science*, No.4, Vol.20, p. 463-470.
- GEMS-Food Euro (1995). Report on a workshop in the frame of the GEMS-Food Euro, EUR/HFA target 22. Second workshop on reliable evaluation of low-level contamination of food. 26-27 May 1995. Kulmbach, Federal Republic of Germany.
- Gilsenan, M.B., Lambe, J., Gibney, M.J. (2003). Assessment of food intake input distributions for use in probabilistic exposure assessments of food additives. *Food Additives and Contaminants*, Vol. 20, No. 11, p. 1023-1033.
- Kuilman, M.E., Maas, R.F., Fink-Gremmels, J. (2000). Cytochrome P450-mediated metabolism and cytotoxicity of aflatoxin B(1) in bovine hepatocytes. *Toxicology In Vitro*, 14: 321-327.
- Leblanc, J.C., Malmauret, L., Delobel, D., Verger, P., (2002). Simulation of the exposure to Deoxynivalenol of French consumers on organic and conventional foodstuffs. *Regulatory Toxicology and Pharmacology*, 36, p. 149-154.

- Murray, D.M., and Burmaster, D.E., 1994. Estimated distributions for average daily consumption of total and self-caught fish for adults in Michigan angler households. *Risk Analysis*, 14, 513-519.
- Paulo, M.J., van der Voet, H., Jansen, M.J.W., ter Braak, C.J.F., van Klaveren, J.D. (2005). Risk assessment of dietary exposure to pesticides using a Bayesian method. *Pest Management Science*, 61, p. 759-766.
- Rubio, R., Moya, V.J., Berruga, M.I., Molina, M.P., Molina, A. (2011). Aflatoxin M1 in the intermediate dairy products from Manchego cheese production: distribution and stability. *Mljekarstvo* 61 (4), p. 283-290.
- Tanguy, J., Zeghnoun, A., Dor, F. (2007). Description du poids corporel en fonction du sexe et de l'âge dans la population française. *Environnement, Risques & Santé*, Vol. 6, No. 3, p. 179-187
- US EPA (Environmental Protection Agency), 2000. Options for Development of Parametric Probability Distributions for Exposure Factors (Washington, DC: US EPA).
- Van Egmond, H.P. (1991). Mycotoxins Inter. Dairy Fed. Special Issue, 9101, 131-145.
- Wood, G.E. (1991). Aflatoxin M1. In R.P. Sharma & D.K. Salunkhe, *Mycotoxins and phytoalexins* (pp. 145-163). (chapter 6). London: CRC Inc.

WEB REFERENCES

- AFSSA, French food safety agency (2009). "INCA2 (2006-2007), Available on line: www.anses.fr/PN8901.htm
- ANSES, French food safety agency (2011). Available on line: www.anses.fr/Documents/PASER2006sa0361Ra2.pdf
- DGCCRF (2005). « Contamination des laits de consommation par l'aflatoxine M1 : résultats du plan de surveillance 2004 ». Available on line : www.minefe.gouv.fr/fonds_documentaire/dgccrf/02_actuallite/brev/es/brv0505i.htm?ru=02
- INSEE (2002-2003). Enquête décennale santé. <http://www.insee.fr>

AUTHOR BIOGRAPHY

NATHALIE WESOLEK was born in Strasbourg, France and after a technical degree in Food engineering and Biology at a College of Advanced Technology, she moved to Brest in order to graduate at a Microbiology and Food Safety Engineering School: ESMISAB. Since the end of 2009, she has been recruited at the Université de Bretagne Occidentale (UBO) in Brest, on sampling schemes performance evaluation for chemical contaminants in food and exposure assessment. She is now beginning a PhD on the application of Bayesian methods as a mean of evaluating mycotoxins sampling schemes in tree nuts.

SOFTWARE TOOL FOR ASSESSMENT OF FOOD CONTAMINATION AND FOOD BANS REGULATIONS

Petr Pecha
Radek Hofman
Institute of Information Theory and Automation of ASCR
Pod Vodarenskou vezi 4
182 08 Prague 8, Czech Republic
E-mail: pecha@utia.cas.cz

Emilie Pechova
Nuclear Research Institute Řež, Division EGP
Vyskočilova 3/741
140 21 Prague 4
E-mail: pechova@egp.cz

KEYWORDS

Irradiation, ingestion pathway, countermeasures, food bans.

ABSTRACT

Dynamic food chain model INGMODEL of radioactivity transport inside a human body is briefly described. Proposed methodology and corresponding user-friendly software enable estimating the consequences arising from ingestion of contaminated foodstuffs. The model is connected with interactive subsystems for entering of input data and graphical presentation of results. An effectiveness of some protective actions introduced in the ingestion pathway on population protection can be tested. The areas contaminated above the permissible limits can be presented directly on the map backgrounds and immediately used for decisions related to launching of the food bans regulations. Simulation of time and space evolution of committed doses from ingestion pathway enables estimate the risk for persons living for a long time in the polluted areas. Architecture of the INGMODEL subsystem was designed with the intention to facilitate examinations of influence of variability of input data. The sensitivity analysis and worst-case assessment can be accomplished as well. An example related to the variability of soil-plant transfer factors is given in the conclusion.

PROPAGATION OF RADIOACTIVITY THROUGH THE LIVING ENVIRONMENT

After the radioactive material is released from a source the admixtures are incorporated into the plume and drift in the downwind direction. The polluted plume expands horizontally and vertically due to turbulent diffusion in the atmosphere. The radionuclides in the plume are bound in a certain physical-chemical forms (aerosols, elemental form, organically bound) and during dispersion are removed from the plume due to several removal mechanisms. The most important are radioactive decay (including daughter products build-up process), dry deposition (gravitational setting and deposition due to contact of the contaminated plume with the ground, vegetation or urban structures) and wet deposition – removal by rainout (precipitation formation process inside of the plume) or by washout (interaction between falling drops and admixtures).

Advection and diffusion transport of pollution are based on the standard Gaussian solution. Further segmentation of the plume into consecutive one-hour segments ensures an accounting for the real situation. A basic idea insists in syn-

chronization of available short-term meteorological forecast (hourly forecast for the next 48 hours provided by the Czech meteorological service) with the time evolution of radioactivity discharges released into the atmosphere. The real dynamics of the accidental release is transformed into an equivalent number G of consecutive homogeneous segments with 1 hour duration. The movement of each segment of pollution is driven by a short-term meteorological forecast for the corresponding hours (phases) of further propagation. SGPM (Segmented Gaussian Plume Model) acronym is used for these approach (more detailed description in (Pecha et al. 2007)). Many effects have to be taken into account approximately such as the thermal structure of the atmosphere (here Pasquill-Gifford notation), surface roughness and other land cover characteristics, orography of the terrain, reflection from the ground and top of the mixing layer or inversion layers, the effect of initial plume rise due to vertical momentum and buoyancy, recirculation in the wake region of the near standing buildings. The effects are usually expressed by semi-empirical expressions derived from experimental results. In the final stage the activity dispersed in the air and deposited on the ground enters into food chains causing a certain contamination of the foodstuffs and fodder. The following radiological consequences from possible pathways of radionuclide transport through the living environment are estimated:

- Exposure to external irradiation from the passing cloud (photons and electrons).
- Exposure to external irradiation from deposited radionuclides (photons and electrons).
- Internal irradiation caused by inhalation of radionuclides from the passing cloud.
- Internal irradiation from inhalation of resuspended radionuclides originally deposited on the ground.
- Internal irradiation resulted from activity intake from the contaminated foodstuffs.

Effective and equivalent doses and/or corresponding committed doses on organs or tissues (gonads, red bone marrow, lung, thyroid, upper large intestine, skin) are evaluated for each of six human age groups.

INTERNAL INTAKE OF RADIOACTIVITY FROM THE INGESTION PATHWAY

Transport of radionuclides through the food chains is treated in relationship to the exposure scenarios. Methodology for chronic long-term releases occurring during nor-

mal operation of a nuclear power plant were adopted from the fundamental code PC-CREAM (Simmonds et al.2010). A new algorithm is proposed in (Pecha et al. 2002). The ecosystem surrounding the NPP is assumed to be continuously submerged into the contaminated environment where customary agricultural practices are applied. An evolution of root and foliar transport of radioactivity into the plants is modelled day by day. Each partial pollution in a day is taken as an adequate portion from the given total annual routine emission. The final consequences are weighted by annual weather statistics.

Short-term accidental releases attended by the radioactive fallout can occur unexpectedly in an arbitrary day in a year. An experience from significant European ingestion models ECOSYS (Müller et al. 1993) and FARMLAND (Brown and Simmonds 1995) has been utilised. Valuable knowledge has been obtained by our participation on customisation of the RODOS project (final report see Müller et al. 2003) for the Czech territory (Raskob et al. 2000), our own contribution is summarized in (Pecha et al. 1999).

In this report we shall concentrate in brevity on description of the ingestion pathway model. Its applications will be presented in more detail. Two different mechanisms of the nuclides uptake into edible parts of the plants are considered:

Foliar uptake of radionuclides: Radioactivity is deposited on leaves and other aerial parts of plants. It depends on the stage of development of the plant canopy which is usually characterized by the actual leaf area index (LAI). Growing functions for each plant during its vegetation period should be determined. The initial deposited activity is decreased due to weathering effects (wind, rain), radioactive decay and tissue ageing (growth dilution effect). Furthermore, the fraction of activity infiltrating into other parts of the plant should be taken into account. This translocation from leaves to the edible parts of the plant is approximately simulated. Proposed dynamical model must distinguish between plants which are used totally (e.g. leafy vegetables, grass) and plant of which only a special part is used (cereals, potatoes).

Root uptake of radionuclides: In general, the root uptake of activity is calculated from the concentration of activity in soil using equilibrium transfer factors which give the ratio of activity concentration in plants (fresh or dry weight) to soil (dry soil). Vertical migration of elements and their fixation in root zone depend on physical-chemical form of an element and on various soil properties. Accumulation of activity in crops is strongly dependent on type of the soil. For example the differences in transfer factors for sand and clay soil types are two orders of magnitude (these variability will be estimated here in the further chapters). The time evolution of activity deposited on the ground is important for consequence assessment in the late stages of an radiation accident. Various magnitudes for migration and fixation recommended for strontium and caesium by a particular expert could be entered into the calculations directly through the subpanel “Radioactivity transport in soil” (see Figure 1). Total time integrated intake of activity $I\mathcal{E}_{TOT}^{a,n}(t)$ (in Bq during the time period t , normalised to the unit deposition of nuclide \underline{n}) for age category \underline{a} due to both direct consumption of edible parts of plants and consumption of contaminated animal products is schematically written as:

$$I\mathcal{E}_{TOT}^{a,n}(t) = \sum_{(l)} I\mathcal{E}_l^{a,n}(t) + \sum_{(b)} \left\{ \sum_{p(b)} I\mathcal{E}_{p(b)}^{a,n}(t) \right\} \quad (1)$$

Here \underline{l} denotes the plant products, \underline{b} means the animal products (milk, meat, eggs). From the products \underline{b} are produced various foodstuffs $\underline{p}(\underline{b})$ (for example from commodity milk are produced the foodstuffs \underline{p} : fresh milk, cream, cheese, milk dry, milk condensed, curd, others – with various specific time delays for consumption). The Czech local age-dependent consumption basket and local dynamic parameters are implicitly included. Substituting $t=1 \text{ year}$ into Equation (1), the terms on the right side represent the total annual activity intake of radionuclide \underline{n} (normalised to the unit deposition rate 1 Bq.m^{-2}) from direct consumption and from consumption of contaminated animal products. Resulting activity intake $I_{ing}(Drate_{gr}^n(x,y))$ is found by multiplying the normalised values from Equation (1) by the real distribution of radioactivity deposited on the ground $Drate_{gr}^n(x,y)$ related to the day of fallout. The distribution of $Drate_{gr}^n(x,y)$ values on terrain with coordinates (x,y) are determined by the dispersion and deposition calculations. The final committed ingestion doses are assessed as a product of the I_{ing} and tabulated conversion factors.

INTERACTIVE INPUT SUBSYSTEM INGMODEL

We have proposed a user friendly subsystem INGMODEL which enables interactive input of the basic parameters of the ingestion calculations. Structure of ingestion panel consists of sequence of separate subpanels that can be called from the basic menu illustrated in Figure 1. A dynamic model is customized for the average Czech conditions using experience from significant European codes ECOSYS (Müller et al. 1993), FARMLAND (Brown and Simmonds 1995) and PC-CREAM (Smith and Simmonds 2008). The dynamical models take into account local consumption habits in dependence on season and human age categories. Agricultural production scheme, average agro-climatic conditions and phenologic characteristics of the plants are determined in direct relation to the specific day of fallout in a year. Many other food chain specific features can be selected interactively such as feeding diets of animals, time delays during processing, transport and storage of foodstuffs and feedstuffs.

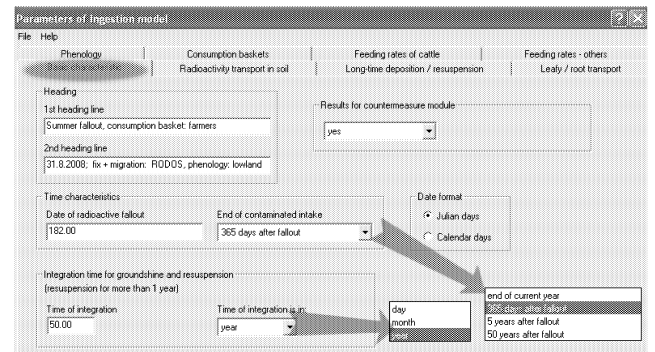


Figure 1: Basic input panel of the INGMODEL subsystem

An attempt for partial differentiation according to so called “radioecological regions” is included in several options from Figure 1: “Consumption habits” (see in Figure

2), “Feeding practices” or “Phenology” (implicit subsets for lowland or highland are offered for selection and, possibly, for additional modifications). The architecture of the module ensures fast examination of influence of variability of the input parameters. It enables to perform effectively the sensitivity analysis and the worst-case assessment. Furthermore, a user can select options for alternative semi-empirical formulae used for particular transport effects. These options can be activated through the entries “Leafy/root transport”, “Radioactivity transport in soil” or “Long-time deposition/resuspension” (see Figure 1). It facilitates markedly the variability examinations and sensitivity analysis of the crucial resulting quantities mentioned above.

Basic characteristic: Phenology		Radioactivity transport in soil: Consumption baskets		Long-time deposition / resuspension: Feeding rates of cattle		Leafy / root transport: Feeding rates - others	
Average year consumption (kg(Bq)/t(kg)) for 6 age categories; DT/konz - delay from harvest to consumption (d)							
Implicit values		Consum. basket: local		Consum. basket: local		DT/konz	
		Consum. basket: global		Consum. basket: global		DT/konz	
		Austrian consum. typical		Austrian consum. typical		DT/konz	
foodstuff	<1year	1-2	2-7	7-12	12-17	adults	DT/konz
Leafy/vegetables	0.84	1.30	1.70	2.00	2.50	2.70	1.00
Leafy/autumn veget.	3.40	5.30	6.90	8.10	10.20	11.00	1.00
Root vegetables	3.20	5.10	6.70	7.80	9.80	10.60	1.00
Fruit vegetables	5.30	8.20	10.90	12.70	15.90	17.20	1.00
Cereals-winter wheat	1.20	3.40	5.40	8.00	11.10	12.30	105.00
Potatoes - autumn	1.70	9.30	16.50	20.00	30.50	31.60	1.00
Extra consumption for critical groups of inhabitants							
foodstuff	<1year	1-2	2-7	7-12	12-17	adults	DT/konz
Forest berries	0.33	0.81	1.20	1.50	1.90	1.50	1.00
Mushrooms	0.00	1.10	1.80	2.20	2.30	2.50	1.00
Fishes	0.00	0.00	0.00	0.00	0.00	0.00	0.00
Game	0.01	0.04	0.07	0.13	0.16	0.32	30.00
Sheep milk	0.06	0.07	0.09	0.09	0.07	0.06	1.00

Figure 2: Consumption baskets selection. Predetermined options: Czech Local, Global and Farmers, Austrian typical

ILLUSTRATION OF CAPABILITY FOR RISK ASSESSMENT IN INGESTION PATHWAY

Proposed INGMODEL code is demonstrated here for two cases of hypothetical accidental releases of radioactivity. A more complex scenario labeled in Table 1 as *case 1* accounts for the real meteorological data archived for March 5, 2009. The hypothetical release was assumed to start at 20.00 CET. Just after two hours the release was assumed to finish.

Table 1: Parameters of examined hypothetical scenarios

	<i>Basic characteristics of hypothetical release</i>
case 1	Real meteorological conditions: from archive for March 5, 2009, 20.00 CET, local rain, stability class D, discharge (Bq per 2 hours): $^{90}\text{Sr}: 1.00\text{E}+14$, $^{131}\text{I}: 1.00\text{E}+14\text{Bq}$, $^{137}\text{Cs}: 1.00\text{E}+15$; Segmented Gaussian Plume Model (SGPM) used; the day of fallout for ingestion calculations: summer, July 1 st .
case 2	Discharge of radioactivity (Bq per 6 hours): $^{90}\text{Sr}: 5.00\text{E}+12$, $^{131}\text{I}_{\text{organic}}: 5.00\text{E}+13$, $^{131}\text{I}_{\text{elemental}}: 9.00\text{E}+14$, $^{131}\text{I}_{\text{aerosol}}: 5.00\text{E}+13$, $^{137}\text{Cs}: 3.00\text{E}+13$, $^{140}\text{Ba}: 1.00\text{E}+14$; Model of straight-line Gaussian propagation used in direction South-East, stability class D, wind speed $3\text{m}\cdot\text{s}^{-1}$, intensive rain $10\text{mm}\cdot\text{h}^{-1}$, with modification of wet interception on leaves, summer day of fallout: July 1 st .

Each of these two one-hour consecutive segments of the plume was driven in the successive 24 hours by meteorological conditions given for each particular hour of the propagation. The real meteorological situation from March 5, 2009 was rather unusual. The radioactivity release with two hours duration was subjected to this atypical (but real) meteorolog-

ical sequence. At 20.00 CET the wind blew around direction WNW and speed about $2.5\text{m}\cdot\text{s}^{-1}$. Prevalent category D of the atmospheric stability according to Pasquill classification with rain was observed. The drifting continued with small changes of wind direction and speed until hour 12 of the propagation. Then the meteo-situation started to change. Situation with low wind speed arose and during the next 6 hours the plume turned nearly to the opposite direction and local atmospheric precipitation again occurred. Each of the 3 nuclides escaping during 2 hours interval from the source were drifting in subsequent 24-hours around the source. The trace of radioactivity was disseminated on terrain. The deposition distributions have entered the ingestion calculations.

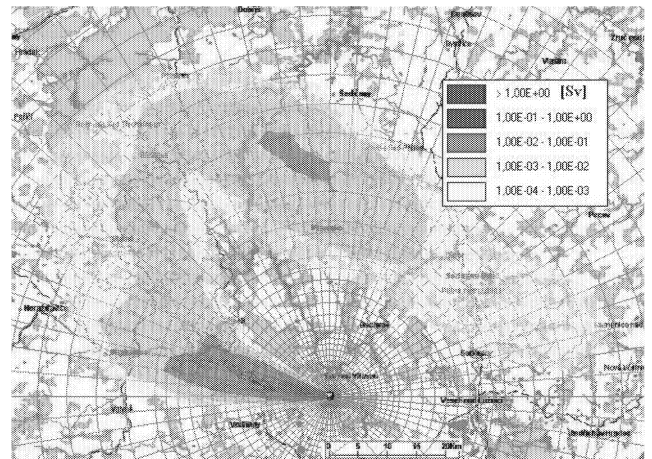


Figure 3: Total effective committed doses for adults – scenario “case 1” from Table 1.

The total annual effective committed doses for adults illustrated in 2-D representation in Figure 3 include the pathways of cloudshine, groundshine, inhalation and ingestion. The ingestion is assumed to be caused by annual radioactivity intake in the first year (year of fallout, summer fallout in July 1 is considered). The effect of local rain caused intensive wet removal of radioactivity and higher deposition on the ground (see Figure 3 - red “rain eye” to the north). More detailed results for scenario “case 1” are in Figure 4. The progression is drawn for the West-North-West straight line according to Figure 3. A person permanently living here and consuming here contaminated foodstuffs will suffer these expected doses after the first year, after the 5th year in total and after the 50th year in total.

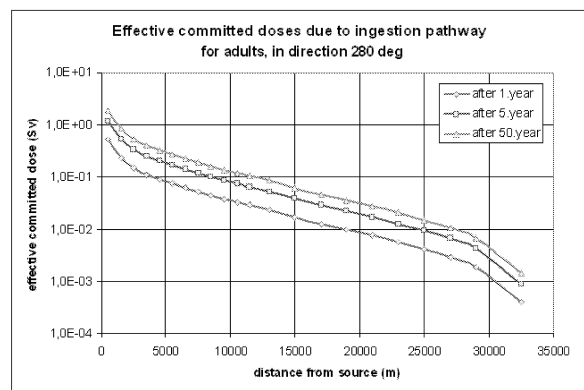


Figure 4: Effective ingestion doses for adults from long term activity intake during 1, 5, 50 years - “case 1”.

Capability to estimate 2-D distribution of the specific activity concentration of ^{137}Cs in the cereals grains is drawn in Figure 5. Depletion of specific activity in the grains at harvest time in the future years is anticipated taking into account effects of Cs migration and fixation in the soil.

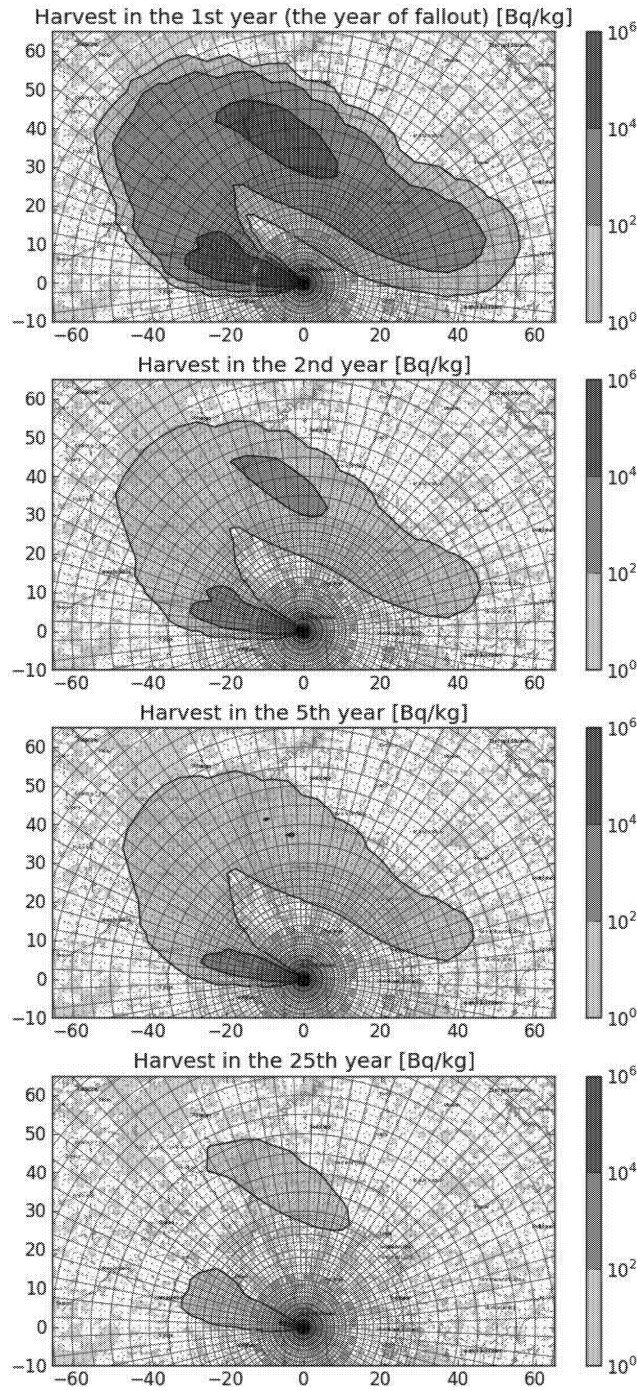


Figure 5: Depletion of specific activity of ^{137}Cs ($\text{Bq}\cdot\text{kg}^{-1}$) in grains of harvested cereals in horizon of 25 years after the fallout - scenario “case 1” from Table 1.

Another illustration of the miscellaneous functions of the countermeasure subsystem associated with the INGMODEL product is given in Figure 6. We consider the harvest in the 2nd year (1 year after the fallout). Limit for cereal grains contamination by ^{137}Cs according to (SONS 2002) is 1250 Bq/kg . Considering the limit for consequences of the scenario “case 1” from Table 1, the restricted area with specific

concentrations above the limit has red colour. The crop harvested in these areas should not be distributed.

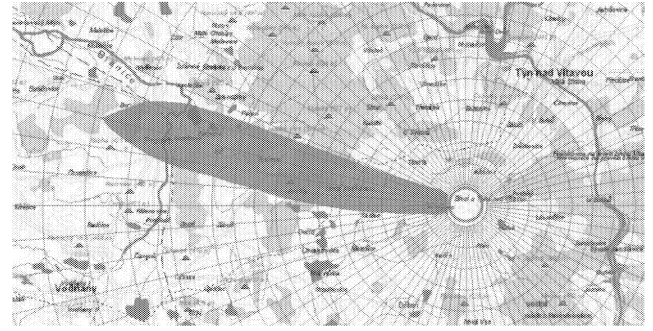


Figure 6: Restricted area for harvest of cereals in the 2nd year after the fallout, given limit of ^{137}Cs in grains is 1250 Bq/kg - scenario “case 1” from Table 1.

PRELIMINARY STUDY OF SENSITIVITY OF INGESTION DOSES ON VARIABILITY OF TRANSFER FACTORS

We should make a distinction between the variability and uncertainty concepts in a risk management. *Variability* reflects changes of a certain quantity over time, over space or across individuals in a population. Variability represents diversity or heterogeneity in a well characterized population. The true variability does not disappear with better measurement. The term *uncertainty* covers stochastic uncertainties, structural uncertainties representing partial ignorance or incomplete knowledge associated with poorly-characterized phenomena and uncertainties of input data. We can only reduce the uncertainties by obtaining the better information.

Let mention the influence of variability of soil types on root uptake of radionuclides in agricultural ecosystems. Root uptake of activity normalized to the unit deposition of radionuclide n [$\text{m}^2 \text{kg}^{-1}$] into the plant l and related to the harvest day t_{skl} can be expressed as:

$$\text{Root } \mathcal{E}_l^n(t_{skl}) = (1 - f^l) \cdot \exp[-(\lambda_2 + \lambda^n) \cdot (t_{skl} - t_{spd})] \cdot \text{BV}_1^n / \text{PH}_l \quad (2)$$

f^l is interception fraction of foliar deposition, t_{spd} is a day of fallout, λ^n , λ_2 represent radioactive decay and removing by environmental effects, PH is density of root zone [kg m^{-2}]. BV_1^n is equilibrium soil to plant transfer factor [$\text{Bq}\cdot\text{kg}^{-1}$ plant / $\text{Bq}\cdot\text{kg}^{-1}$ soil]. Thorough search was accomplished in (IAEA Technical Report Series 2010) which represents an extensive long-lasting study following the consequences of the nuclear weapons testing. Several selected values are recorded in Table 2.

Table 2: Soil to plant transfer factors for pasture [$\text{Bq}\cdot\text{kg}^{-1}$ plant / $\text{Bq}\cdot\text{kg}^{-1}$ soil] (all soil types), (IAEA TRS2010).

element	mean value	minimum	maximum
Cs	2.50E-01	1.00E-02	5.00
I	3.70E-03	9.00E-04	5.00E-01
Sr	1.3	5.60E-02	7.3

At the same time the activity transfer to animals due to ingestion of contaminated feedstuffs were selected and recorded in Tables 3 and 4. This equilibrium factors express the rate of daily activity intake which remains in one kilogram or liter of the animal product.

Table 3: Equilibrium transfer factor to cow milk [d.L⁻¹].

element	mean value	minimum	maximum
Cs	4.6E-03	6.0E-04	6.8E-02
I	5.4E-03	4.0E-04	2.5E-02
Sr	1.3E-03	3.4E-04	4.3E-03

Table 4: Equilibrium transfer factor to beef [d.kg⁻¹].

element	mean value	minimum	maximum
Cs	2.2E-02	4.7E-03	9.6E-02
I	6.7E-03	2.0E-03	3.8E-02
Sr	1.3E-03	2.0E-04	9.2E-03

Geometric mean is given in the tables. Statistical analysis depends on number of observed values. In some cases only limited data are available and reported data should be used with caution. The values in Table 2 are recommended for a certain representative mixture of soil types. More precise treatment should include the discrimination by soil type categories *sand*, *loam*, *clay* and *organic*. The maximum values in Table 2 are close to the sand category, whereas minimum values come near to the clay items. The results in Figure 7 can be perceived as a sensitivity examination of the ingestion pathway on the variability in soil types.

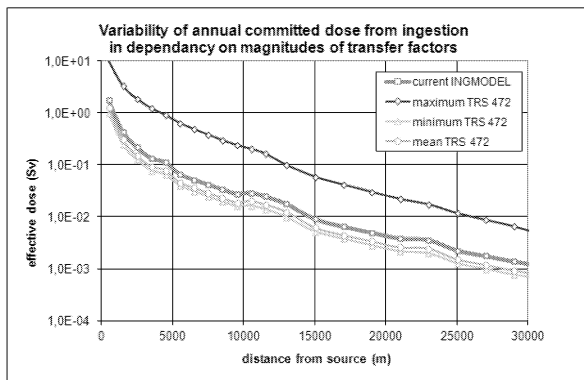


Figure 7: Sensitivity of ingestion doses on variability of transfer factors (TRS 2010)- scenario “case 2” in Table 1.

CONCLUSION

The proposed dynamic ingestion system is briefly described and various capabilities are demonstrated using graphical output subsystem. This article summarizes a wide range of deterministic calculations of the radiological consequences of a hypothetical accidental release of radionuclides into the living environment. A step towards sensitivity examinations is finally mentioned. The INGMODEL development continues in direction of probabilistic risk evaluation when more informative answers can be generated on assessment questions. Our first results covering the late stage of radiation accident were published in (Pecha and Pechova 2005). From that time onwards an effort for advancing a proper software

tool for assimilating of model predictions with the field measurements is in a systematic progress.

ACKNOWLEDGEMENTS

This activities are supported by the project No. VG20102013018 provided by the Ministry of the Interior of the Czech republic.

REFERENCES

- Brown, J. and J.R. Simmonds. 1995. “FARMLAND-A Dynamic Model for the Transfer of Radionuclides through Terrestrial Foodchains.” Research Report NRPB-R273, Chilton, Didcot,UK.
- International Agency for Atomic Energy. 2010. Handbook of Parameter Values for Predictions of Radionuclide Transfer in terrestrial and Freshwater Environments. IAEA Technical Report Series TRS No. 472, Vienna.
- Müller, H. and G. Pröhl. 1993. “ECOSYS’87: A Dynamic Model for Assessing Radiological Consequences of Nuclear Accidents.” *Health Physics*, Vol. 64, No. 3, March 1993.
- Müller, H., F. Gering and G. Pröhl. 2003. “Model Description of the Foodchain and Dose Module Terrestrial in RODOS PV6.0”. Technical report RODOS(RA3)-TN(03)-06.
- Pecha, P., P. Kuca and P. Nedoma. 1999. “Foodchain and Dose Module Terrestrial Customization for the Czech Republic”. Technical report RODOS(WG3)-TN(98)-14 – final version 1999.
- Pecha, P. and E. Pechova. 2002. "Application of Multi-Pathway Transport Model for Regulation of Normal Atmospheric Radioactive Discharges from Nuclear Facilities". In *Proc. of the 8th Int. Conf. on Harmonisation within Atmospheric Dispersion Modelling* (Sofia, Bulgaria), paper No. A94rep.
- Pecha, P. and E. Pechova. 2005. “Modeling of random activity concentration fields in air for purposes of probabilistic estimation “. In *Proc. of the 10th Int. Conf. on Harmonisation within Atmospheric Dispersion Modelling* (Sissi, Greece), paper No. H11-069.
- Pecha, P., R. Hofman and E. Pechova. 2007. “Training simulator for analysis of environmental consequences of accidental radioactivity releases”. In *Proc. of the 6th EUROSIM Congress on Modelling and Simulation* (Ljubljana, Slovenia, Sept. 9-13, 2007), 18 pp., Conference CD– ISBN 978-3-901608-32-2.
- Raskob, W. ed., A. Kerekes, A. Dvorzak, O. Slavik and P. Pecha. 2000. "Documentation on the Two INCO Working Programs: Review of the Adequacy of the Present Foodchain and Dose Calculations and Collection of the Data Required for Each Radioecological Region and their Integration into RODOS". Technical report RODOS (WG3) – TN(99)-40, 180 pages.
- Smith, J.G. and J. R. Simmonds. 2008. The Methodology for Assessing the Radiological Consequences of Routine Releases of Radionuclides to the Environment Used in PC-CREAM 08. Research Report HPA-RPD-058, Health Protection Agency, Chilton, Didcot,UK.
- State Office for Nuclear Safety (SONS). 2002. *Regulation No. 307/2002 on Radiation Protection: Annex No. 8: Maximum Permissible Levels of Radioactive Contamination of Foodstuffs*. SONS Governmental Document of the Czech Republic No. 307/2002, Prague.

COMBINED EFFECTS OF γ -IRRADIATION AND STORAGE TIMES ON SUGARS COMPOSITION OF *Lactarius deliciosus*: COMPARISON THROUGH LINEAR DISCRIMINANT ANALYSIS

Ângela Fernandes^{1,2}
João C.M. Barreira^{1,2}
Anabela Martins¹
Isabel C.F.R. Ferreira¹

¹CIMO-ESA - Instituto Politécnico de Bragança, Portugal; Email: iferreira@ipb.pt

M. Beatriz P.P. Oliveira²
²REQUIMTE/Departamento de Ciências Químicas, Faculdade de Farmácia, Porto, Portugal

Amilcar L. Antonio^{1,3}
³GTRPP/Unidade de Física e Aceleradores, ITN, Sacavém, Portugal.

KEYWORDS

Lactarius deliciosus, shelf-life, gamma irradiation, sugars

ABSTRACT

The effects of gamma irradiation on *Lactarius deliciosus* (L. ex Fr.) S. F. Gray sugars were evaluated in samples submitted to different storage periods (0, 4 and 8 days) at 4 °C. The irradiations were performed in a ⁶⁰Co experimental equipment. Changes in sugars were determined by analyzing the results obtained by high performance liquid chromatography coupled to refraction index detection (HPLC-RI) through a 2-way analysis of variance and a linear discriminant analysis. Mannitol was by far the most abundant sugar in the analyzed samples. Regarding sugars profile, storage time proved to have higher influence than irradiation dose, mainly reflected in the decrease of fructose and mannitol in stored samples.

INTRODUCTION

The special place held by mushrooms in human food is well illustrated by the statistic data regarding world production of mushrooms and truffles which in 2007 reached a volume of 3 414 392 metric tons (USDA 2009). Their global economic value is now staggering, and the reason for the rise in consumption is a combination of their value as food (Kalač 2009) and their medicinal or nutraceutical properties (Ferreira et al. 2010).

In Europe, mushrooms are highly consumed (*L. deliciosus* is among the most consumed wild species) due to their high contents of digestible proteins, carbohydrates, vitamins and fibers. Nevertheless, mushrooms are one of the most perishable products and tend to lose quality right after harvest. The short shelf-life of mushrooms (1-3 days at room temperature) is an obstacle to their distribution and marketing as fresh products. Mushrooms may suffer spoilage during storage due to bacteria, moulds, enzymatic activity, or biochemical changes. Despite the immense popularity of this food in the Northeast of Portugal (one of the European regions with the highest mushrooms biodiversity) and its increased exportation to foreign countries (particularly Spain, France and Italy), data regarding technologies to enlarge their shelf-life is still scarce. Irradiation emerges as a possible conservation technique that has been tested successfully in several food products (regulated in the European Union by Directive 1999/2/EC). Studies reporting the use of ionizing radiation

on mushrooms are available mainly in cultivated species such as *Agaricus bisporus*, *Lentinus edodes* and *Pleurotus ostreatus*.

In the present study the effects of gamma irradiation on the sugars profile of *L. deliciosus* are analyzed considering samples submitted to different storage (4 °C) times (0, 4 and 8 days).

MATERIALS AND METHODS

Samples and samples irradiation

L. deliciosus specimens were collected in the Northeast of Portugal (November 2011) and divided in three groups with eighteen units per group: non irradiated samples (control), samples exposed to 0.5 kGy and samples exposed to 1.0 kGy, at a dose rate of 2.2 kGy h⁻¹.

To estimate the dose rate it was used a chemical solution sensitive to ionizing radiation, the Fricke dosimeter, prepared and measured as described by one of us (Antonio et al. 2011). Irradiations were performed on ⁶⁰Co gamma chamber (Precisa 22, Graviner Manufacturing Company Ltd) with four sources, and total activity of 267 TBq (7.2 kCi) in November 2010. After irradiation, mushroom samples were analyzed promptly and after 4 and 8 days of storage at 4 °C. After that time, the samples were lyophilized (FreeZone 4.5 model 7750031, Labconco), reduced to a fine dried powder (20 mesh), mixed to obtain a homogenate sample and kept at -20 °C until further analysis.

Analysis of free sugars

Free sugars were determined by HPLC-RI (Barros et al. 2007), using raffinose as internal standard (IS). The equipment consisted of an integrated system with a pump (Knauer, Smartline system 1000), degasser system (Smartline manager 5000), auto-sampler (AS-2057 Jasco) and a RI detector (Knauer Smartline 2300). Data were analysed using Clarity 2.4 Software (DataApex). The chromatographic separation was achieved with a Eurospher 100-5 NH₂ column (4.6 × 250 mm, 5 mm, Knauer) operating at 30 °C (7971 R Grace oven). The mobile phase was acetonitrile/deionized water, 70:30 (v/v) at a flow rate of 1 mL/min. The compounds were identified by chromatographic comparisons with authentic standards. Quantification was performed using the internal standard method and sugars content was further expressed in g per 100 g of dry weight (dw).

Statistical analysis

An analysis of variance (ANOVA) with Type III sums of squares was performed using the GLM (General Linear Model) procedure of the SPSS software, version 18.0 (SPSS, Inc.). All dependent variables were analyzed using a 2-way ANOVA, being the main factors the “irradiation dose (ID)” (0.0, 0.5 and 1.0 kGy) and the “storage time (ST)” (0, 4 and 8 days). Since a statistical significant interaction effect (ID×ST) was found in all tests, the two factors were evaluated simultaneously by plotting the estimated marginal means for all levels of each factor. In addition, a linear discriminant analysis (LDA) was used as a technique to classify the irradiation doses as well as the storage times according to the detected sugars profiles. A stepwise technique, using the Wilks’ λ method with the usual probabilities of F (3.84 to enter and 2.71 to remove), was applied for variable selection. To verify which canonical discriminant functions were significant, the Wilks’ λ test was applied. A leaving-one-out cross-validation procedure was carried out to assess the model performance. The LDA statistical analysis and the other statistical tests were performed at a 5% significance level using the SPSS software mentioned above.

RESULTS AND DISCUSSION

Mannitol is by far the major individual sugar, followed by trehalose and fructose. This is in agreement with the results reported by us in a previous study with the same mushroom species (Barros et al. 2007).

Table 1 presents the mean value of each irradiation dose (ID) over the different storage times (ST) as well as mean value of the assayed ST within each irradiation dose. The interaction effect among ST and ID was significant in all cases; thereby no multiple comparisons could be performed. Nevertheless, ST seemed to exert more evident changes in sugars profile than irradiation dose (please see LDA discussion below).

Table 1: Effect of storage time (days) and γ -irradiation doses (kGy) in sugars contents (g/100 g dw) of *Lactarius deliciosus*.

		Fructose	Mannitol	Trehalose
ST	0 days	0.18±0.03	12±2	1.4±0.5
	4 days	0.15±0.04	9±2	1.1±0.2
	8 days	0.06±0.03	8±1	1.2±0.4
	<i>p</i> -value	<0.001	<0.001	<0.001
ID	0.0 kGy	0.13±0.05	11±1	0.77±0.04
	0.5 kGy	0.1±0.1	8±2	1.7±0.5
	1.0 kGy	0.15±0.04	11±3	1.1±0.2
	<i>p</i> -value	<0.001	<0.001	<0.001
ST×ID	<i>p</i> -value	<0.001	<0.001	<0.001

The differences found for each effect (ST or ID) were reflected in the results obtained for LDA. In fact, ST conducted onto the formation of three well individualized clusters (corresponding to the three assayed periods) (Figure 2A). The model showed a very satisfactory classification performance allowing to correctly classifying

100.0% of the samples for the original groups as well as for the cross-validation procedure. Regarding ID, the discriminant scores were not clearly separated (Figure 2B), especially those belonging to non-irradiated and 1.0 kGy dose irradiated samples, proving that ST had higher influence over sugars profile of *L. deliciosus* (88.9% of the samples for the original groups and 86.1% for the cross-validation procedure correctly classified cases).

Both discriminant models defined two significant ($p < 0.001$ for the Wilks’ λ test) functions, which explained 100.0% of the variance of the experimental data (Figure 2).

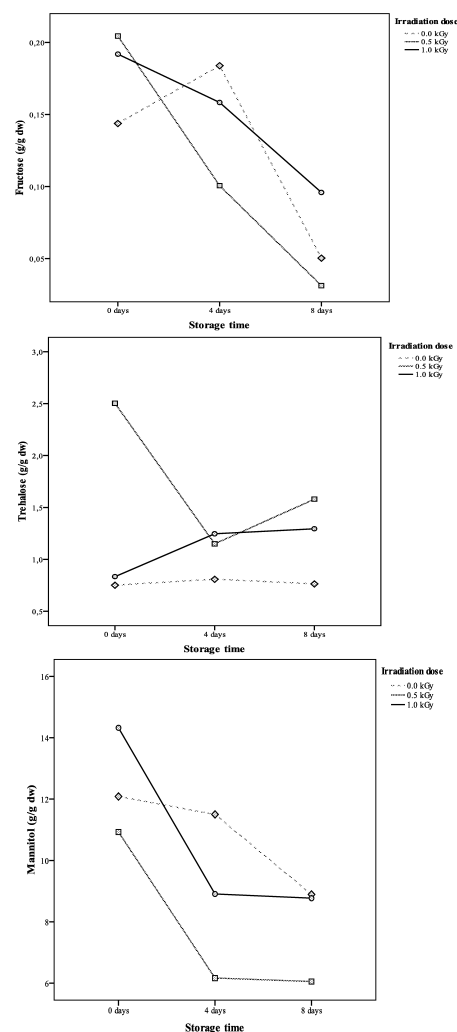


Figure 1A: Interactions between irradiation dose effects and storage times on *L. deliciosus* individual sugars.

In order to better comprehend of the evaluation of sugars profile along the time-line for each ID, the estimated marginal means obtained in the GLM are presented in Figures 1A and 1B. In these outputs, some particular tendencies could be detected: trehalose was lower for non-irradiated samples, while mannitol was lower in samples irradiated with 0.5 kGy. On the other hand, fructose and mannitol were lower after 8 days of storage. In the particular case of trehalose, a non-reducing sugar, the effect of ST is less observable due to its lower susceptibility to oxidation. Regarding ID effects, it seemed that trehalose was preserved in irradiated samples, while it decreases in non-irradiated samples.

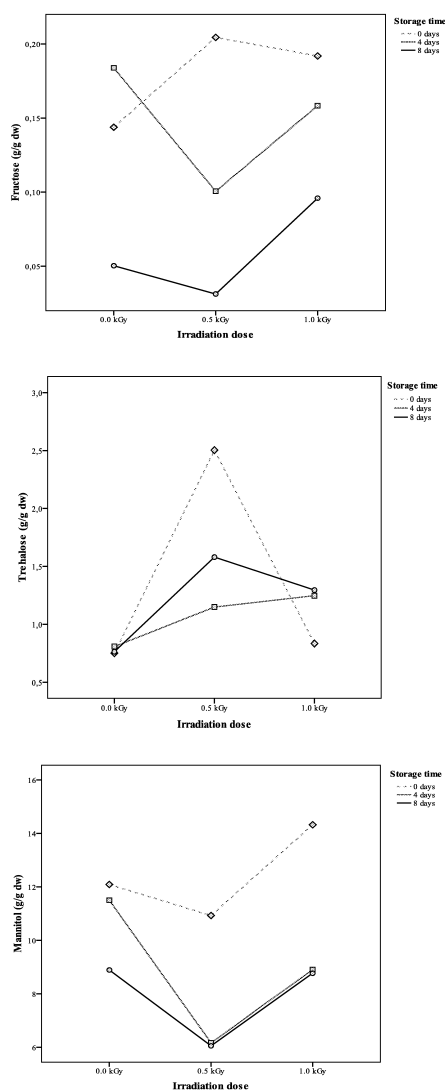


Figure 1B: Interactions between storage time effects and irradiation doses on *L. deliciosus* individual sugars.

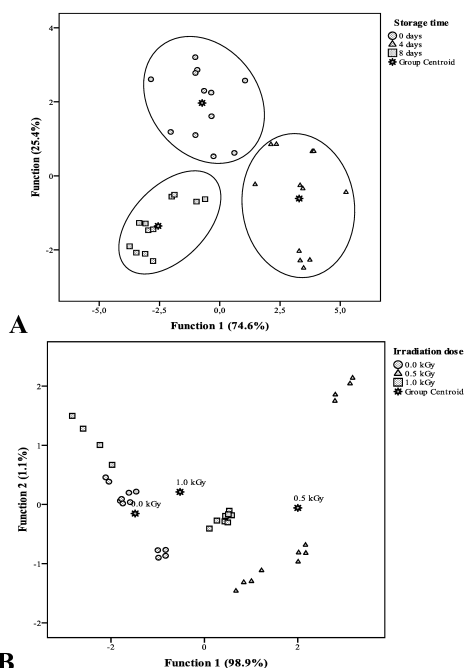


Figure 2. Discriminant scores defined by canonical analysis of sugars profile for ST (A) and ID (B).

CONCLUSIONS

Irradiation could be an alternative to ensure the quality and extend the life of mushrooms. In fact, sugars profile is known for being a reliable indicator of adequate conservation technology. In this study, the results seemed to indicate that the effect provoked by storage time overcame the influence of irradiation, highlighting this technique as promising conservation methodology in food products. In fact, it became clear that it is easier to conclude if a mushroom sample was stored than if the same sample was irradiated, due to the dominant effects of storage over irradiation.

ACKNOWLEDGEMENTS

FCT and COMPETE/QREN/EU: Project PTDC/AGR-ALI/110062/2009 and BD/76019/2011 to A. Fernandes.

REFERENCES

- USDA - Economic research service. Mushroom Industry Report 94003, 2009.
- Kalač, P. Chemical composition and nutritional value of European species of wild growing mushrooms: A review. *Food Chemistry*, 2009, *113*, 9-16.
- Ferreira, I.C.F.R., J.A. Vaz, M.H. Vasconcelos, A. Martins. Compounds from wild mushrooms with antitumor potential. *Anti-cancer Agents in Medicinal Chemistry*, 2010, *10*, 424-436.
- Antonio, A.L., A. Fernandes, J.C.M. Barreira, A. Bento, M.L. Botelho, I.C.F.R. Ferreira. Influence of gamma irradiation in the antioxidant potential of Chestnuts (*Castanea sativa* Mill.) fruits and skins. *Food and Chemical Toxicology*, 2011, *49*, 1918-1923.
- Barros, L., P. Baptista, D.M. Correia, J.S. Morais, I.C.F.R. Ferreira. Effects of conservation treatment and cooking on the chemical composition and antioxidant activity of Portuguese wild edible mushrooms. *Journal of Agricultural and Food Chemistry*, 2007, *55*, 4781-4788.

AUTHOR BIOGRAPHIES

ÂNGELA FERNANDES is working in the evaluation of the effects of ionizing radiation on mushrooms chemical composition. afeitor@ipb.pt

AMILCAR L. ANTONIO research interests are related to food irradiation. amilcar@ipb.pt

JOÃO C.M. BARREIRA research interests are related to chemical composition and bioactivity of wild mushrooms and plants. jbarreira@ipb.pt

ANABELA MARTINS research interests are in the plant and fungi biotechnology domains. amartins@ipb.pt

M. BEATRIZ P.P. OLIVEIRA research interests are related to chemical composition of food products. beatoliv@ff.up.pt

ISABEL C.F.R. FERREIRA research interests are related to chemical composition and bioactivity of wild mushrooms, plants and chestnuts. iferreira@ipb.pt

A META-ANALYTICAL ASSESSMENT OF THE VARIABILITY BETWEEN ABATTOIRS IN THE EFFECT OF CHILLING ON THE *SALMONELLA* INCIDENCE ON PIG CARCASSES

Ursula Gonzales-Barron, James Sheridan, Francis Butler
UCD School of Biosystems Engineering
University College Dublin
UCD Belfield
Ireland
E-mail: ursula.gonzalesbarron@ucd.ie

Vasco Cadavez
Food Safety and Technology Group
CIMO Mountain Research Centre
Polytechnic Institute of Braganza
Portugal
E-mail: vcadavez@ipb.pt

KEYWORDS

Pig, slaughterhouse, meta-analysis, chilling, *Salmonella*.

ABSTRACT

The aim of this study was to estimate the overall effect of chilling on the *Salmonella* occurrence on pig carcasses during pork processing. Meta-analyses were conducted on the outcomes of research studies conducted in 32 abattoirs. A random-effects model was applied, and the between-abattoir variability ($\tau^2=0.548$) was significant ($p<0.001$). Results also showed that publication bias is unlikely. Thus, this meta-analysis allowed the generalisation that chilling reduces the *Salmonella* incidence by a factor of 1.62 (95% CI: 1.09-2.41). However, a multilevel meta-analysis showed that the 'number of sampling visits', within abattoir, significantly ($p<0.05$) affected the chilling effect size, accounting for 40% of the between-abattoir variability. Thus, the beneficial effect of chilling only became apparent in a consistent way when at least two sampling visits took place in an abattoir.

INTRODUCTION

Meta-analysis concerns the statistical summarisation of the results of a large collection of independently conducted primary studies on one specific research question (Glass 1976). Thus, meta-analysis aims to explain differences in study outcomes by coding study characteristics such as research design features, data collection procedures or type of subjects sampled (Hox and de Leeuw 2003). In a fixed-effects model, the studies are regarded as simple replications of each other. This assumption considers that the possible differences between study outcomes are due to sampling error. However, heterogeneity in primary study outcomes is expected as different studies employ different experimental manipulations or measure the effects with different methodologies. To address this heterogeneity, a random-effects model is the best choice as it assumes that study outcomes vary not only because of random sampling effects (within-study variations), but also because of real differences between studies. If heterogeneity among primary studies is present, the next goal is then to identify the study characteristics or moderators that explain the differences between study outcomes. For this, an original new analytic direction was taken by Raudenbush and Bryk (1985), who

argued that a meta-analysis could be regarded as a special case of *multilevel analysis* using hierarchical linear models, with subjects between studies at the first level and studies at the second level. The major advantage of using multilevel analysis instead of classical meta-analysis methods is its flexibility as it is simple to include moderators as explanatory variables in the model (Hox and Leeuw 2003).

In food safety research, meta-analysis may be conducted to address a broad range of research questions such as disease incidence, consumer practices, prevalence of microorganisms, effect of interventions pre- and post-harvest, etc. Performing a meta-analysis, Gonzales-Barron et al. (2008) confirmed that chilling has a significant effect on the reduction of pathogenic *Salmonella* occurrence in pig carcasses. However, the effect size of chilling was estimated using only pooled numbers of positive and tested carcasses per primary studied; being a case of a classical meta-analysis integrating only summarised outcomes. As other primary studies became available, it was realised that, for most of the studies, the *Salmonella* occurrence data of pigs pre and post chill could be broken down by abattoir. Thus, the objectives of this research were (i) to revise the effect size of chilling on *Salmonella* occurrence on pig carcasses considering the results of new primary studies; (ii) to quantify the between-abattoir variability in the effect of chilling; and (iii) to demonstrate the use of simple multilevel meta-analysis to attempt to explain the heterogeneity in the primary study outcomes.

METHODOLOGY

As indicated by Sargeant et al. (2005), to perform a meta-analysis, three important facets are to be considered: population, intervention or treatment and measured outcome. The problem statement in this study was the estimation of the overall effect of chilling on the prevalence of *Salmonella* on pig carcasses during slaughterhouse processing. The *population* was specified as eviscerated pig carcasses after veterinarian inspection in abattoirs. The *treatment* is represented by the chilling stage during carcass/pork processing, which includes cooling and cold storage (18 to 24 h) at ~ 5 C. The *measured outcome* is the detection of *Salmonella* on the pig carcass surface. Following the systematic review protocol presented by Sargeant et al. (2005), and after assessing all the

Table 1: Occurrence of *Salmonella*-Positive Pig Carcasses By Abattoir Before and After Chilling as Detected in Eleven Primary Studies

Primary study	Coded study	Coded Abattoir (j)	Number of visits (Nv)	Pre-chill group (Control)		Post-chill group (Treated)	
				s_C	n_C	s_T	n_T
Booteldorn et al. (2003)	1	1	2	14	55	9	55
		2	1	2	30	3	20
Bouvet et al. (2003)	2	3	2	6	60	3	60
		4	2	1	62	3	62
		5	2	1	60	0	60
Cutter (2003)	3	6	1	0	23	4	23
		7	1	0	30	2	30
		8	1	2	45	2	45
		9	1	0	30	0	40
		10	1	1	30	0	15
		11	1	1	15	0	15
Davies et al (1999)	4	12	1	0	15	0	15
		13	1	7	25	3	25
Dugan et al. (2010)	5	14	4	1	66	1	61
		15	3	12	50	2	47
		16	2	3	29	1	23
		17	3	2	30	1	30
Minvielle (unpublished data)	6	18	2	4	60	0	60
		19	2	8	60	4	60
		20	2	4	60	16	60
Oosterom et al. (1985)	7	21	NS ¹	19	64	9	64
		22	NS	4	71	2	71
		23	NS	4	75	1	75
Epling et al (1993)	8	24	NS	61	188	72	188
Algino et al. (2009)	9	25	NS	10	112	25	112
De Busser et al. (2011)	10	26	2	0	39	0	39
		27	2	2	43	0	43
		28	2	23	51	4	51
		29	2	5	44	1	44
		30	2	1	49	0	49
Arguello et al. (2011)	11	31	3	118	311	31	310
		32	3	61	135	17	135

⁽¹⁾ Number of visits within each sampled abattoir not specified

information presented in every study, eleven primary studies were considered appropriate for inclusion in the meta-analysis models (Table1). Next, a parameterisation or measure unit of the intervention's effect size needs to be determined. The effect size (θ) refers to the degree to which the hypothetical phenomenon is present in the population. Relative risk (RR) was chosen as the effect size parameterization for being less susceptible to differences in study protocols (Gonzales-Barron et al. 2008). The outcome data were available on n_T pig carcasses in the post-chill group (treated group) and n_C pig carcasses in the pre-chill group (control group). The number of successes (*Salmonella*-positive carcasses) in the post-chill and pre-chill group are represented by s_T and s_C , respectively. Results in Table 1 are presented broken down by abattoir surveyed (j), and includes the study characteristic or moderating variable of number of sampling visits per abattoir (Nv). A fixed-effects, random-effects and a multilevel model with the moderating variable Nv were fitted. The fixed-effects and random-effects model were

fitted using the same data set presented in Table 1. However, as the number of visits per abattoir Nv were not available in Oosterom et al. (1985), Epling et al. (1993) and Algino et al. (2009), the results from these three primary studies were removed for the multilevel model.

Fixed-effects meta-analysis

In its simplest form, a fixed-effects approach can be carried out to make a *conditional inference* only about the j primary studies included in the meta-analysis (Hedges and Vevea 1998). On the other hand, a fixed-effects meta-analysis can also be conducted under the assumption that the possible differences between study results are only due to sampling variance. In any case,

$$\theta_j = \Theta + \varepsilon_j \quad (1)$$

with θ_j the observed effect size in the abattoir j , Θ the population effect size, and ε_j the residual error due to sampling variance. It is assumed that the ε_j have a normal distribution with mean zero and a true variance ξ^2 . In our particular case, the effect size θ_j refers to the natural logarithm of the relative risk (log RR). Apart from the values of θ_j from each abattoir, the standard error of the effect size $\sigma(\theta_j)$ are to be calculated.

$$\theta_j = \log RR = \log \frac{s_T/n_T}{s_C/n_C} \quad (2)$$

$$\sigma(\theta_j) = \sigma(\log RR) = \left(\frac{n_T - s_T}{n_T s_T} + \frac{n_C - s_C}{n_C s_C} \right)^{0.5} \quad (3)$$

To estimate the population effect size Θ , the observed size effects θ_j should be averaged. Because studies usually differ in the reliability of estimating the true effect size, for instance, due to differences in study size, a weighted average is preferred with weights w_j equal to the precision in estimating the population effect size. Because in this simple fixed-effects model, it is assumed that the deviation of the observed effect sizes from the population effect size is due to sampling error alone, the precision can be defined as the inverse of the (estimated) sampling variance. The estimated population effect size and its standard error would be,

$$\hat{\Theta} = \frac{\sum_j w_j \theta_j}{\sum_j w_j} \quad (4)$$

$$\hat{\sigma}(\hat{\Theta}) = \frac{1}{\left(\sum_j w_j \right)^{0.5}} \quad (5)$$

with $w_j = 1/\sigma^2(\theta_j)$. Because meta-analyses are performed retrospectively, in many situations studies may differ from each other due to differences in measuring protocols, in the population from which the sample is drawn, and in the kind of dose and treatment that is offered; all of these giving rise to heterogeneity. A popular homogeneity test is the Q statistic,

$$Q = \sum_j \frac{(\theta_j - \hat{\Theta})^2}{\sigma^2(\theta_j)} \quad (6)$$

When effect sizes across studies are homogeneous, Q follows a chi-square distribution with $(j-1)$ df. If the hypothesis is rejected, there is evidence that there are additional sources of variability other than within-study sampling error. It is then common practice to examine moderator variables; divide the studies in homogeneous

groups to perform separate meta-analysis; or to use a random-effects model.

Random-effects meta-analysis

One way to model the heterogeneity among the true effects measured by the primary studies is to treat it as purely random (Viechtbauer 2010). In contrast to the fixed-effects model, random models provide an *unconditional inference* about a larger set of studies from which the j studies included in the meta-analysis are assumed to be a random sample (Hedges and Vevea 1998). In a random-effects model, each study investigates its own true effect size Θ_j ,

$$\theta_j = \Theta_j + \varepsilon_j = \bar{\Theta} + v_j + \varepsilon_j \quad (7)$$

with $\bar{\Theta}$ the mean true effect size and v_j the deviation of the true study effect size from the mean true effect size. The values of v_j are normally distributed random effects with a mean of zero and a variance of τ^2 . In this approach, two sources of variation are distinguished: sampling variation (ε_j^2) and variation between true effect sizes (τ^2). By including τ^2 , the standard error in the effect size estimates represents random variability at both the subject level and the study level. As in the fixed-effects approach, a weighted method is also used to estimate the mean true effect size and its standard error. The inverse variance weight or precision of the primary studies should then be corrected (w_j^*) by addition of the between-study variability term τ^2 ,

$$w_j^* = \frac{1}{\sigma^2(\theta_j) + \tau^2} \quad (8)$$

with the variance τ^2 estimated from the Q -statistic,

$$\hat{\tau}^2 = \frac{Q - (j - 1)}{\sum_j w_j - \left(\sum_j w_j^2 / \sum_j w_j \right)} \quad (9)$$

The mean true effect size Θ and its standard error $\sigma(\Theta)$ are estimated with equations (4) and (5) using instead the corrected weights w_j^* .

Multilevel meta-analysis

A meta-analysis can be considered a special case of *multilevel analysis* using hierarchical linear models, with subjects between studies at the first level and studies at the second level. If the between-study variance is shown to be noteworthy, one or more moderators (study characteristics) can be added to the model to account for at least part of the heterogeneity in the true effects. In our model, the moderator Nv (number of sampling visits in an abattoir) was added,

$$\theta_j = \Theta_j + \varepsilon_j = \beta_0 + \beta_1 Nv_j + v_j + \varepsilon_j \quad (10)$$

This model treats the moderator effect β_1 as fixed and the v_j as random effects that distribute normally with a mean of zero and a variance of τ^2 . Yet, τ^2 now denotes the amount of residual heterogeneity among the true effects, or the variability among the true effects that is not accounted for by the moderators included in the model. To estimate the parameters, maximum likelihood estimation (MLE) procedures are the most frequently used. In MLE, residuals on both levels (v_j and ε_j of Equation 10) are assumed to be independently distributed. Meta-analysis models were fitted in R version 2.14.2 (R Development Core Team) using the 'metafor' package (Viechtbauer 2010), which provides functions for fitting the models described above.

RESULTS AND DISCUSSION

The fixed-effects model provided strong evidence that the chilling stage in pork processing has a decreasing effect on the occurrence of *Salmonella* on pig carcasses ($p < 0.001$). After taking the inverse of the exponential of the estimated overall effect size ($\Theta = -0.550$ in Table 2), it can be inferred that, on average, chilling reduces the *Salmonella* incidence by a factor of ~ 1.73 (95% CI: 1.49 – 2.02). Although there is evidence of heterogeneity by the significant Q statistic (Table 2), this fixed-effects model still provides valid inferences as long as they are restricted to the set of studies included in the meta-analysis (Viechtbauer 2010). The forest plot shown in Figure 1 highlights the variability in effect size estimates and precision between abattoir entries; and the marker size illustrates the contribution of each abattoir (weight) to the overall effect estimate for the fixed-effects solution. It should be noticed that weights are not only related to sample size, but instead to the number of successes or failures in proportion to the sample size. Analyzing the definition of the standard error of the Ln RR parameterization (Equation 3), inverse-variance weights will be small when the number of *Salmonella*-positive carcasses (successes) in either group (before or after chilling) is close to zero. For instance, abattoirs 26 and 30, with a reduced number of successes pre-chill and post-chill (Table 1) produced very low weights (Figure 1). In contrast,

weights will be large when the number of successes in both groups are high. In an extreme case, where there was no failure in both groups, the weights would be equal to infinity. That explains why abattoirs 24, 31 and 32 with the highest sample sizes and the highest proportion of successes (Table 1) produced the highest weights (Figure 1). Yet, small studies can still be given a large weight when they have relatively more successes. For instance, abattoir 1 with a sample size ($n_C = n_T = 55$) smaller than abattoir 5 ($n_C = n_T = 60$) was assigned a higher weight (Figure 1) since its number of successes in proportion to sample size was much higher than the latter (Table 1). Thus, the inverse-variance weighting permits the consideration of small but well-designed studies, that otherwise would have been disregarded because of their lack of statistical power to show a significant difference for the outcome of interest, had the weighting been based on sample size alone.

A visual examination of the forest plot (Figure 1) gives an idea of the discrepancy among abattoir entries, which is not surprising given the several sources of variability among studies and abattoirs such as sampling site, chilling equipment, cross contamination of carcasses, level of *Salmonella* infection at slaughterhouses, differences in the microbiological protocol, year and country, among others. In the random-effect model, the overall effect size is still significant although at a limiting p-value (Table 2). This occurred because the addition of the relatively high variability at abattoir level to the random variability at carcass level, produced an increase of the standard error of the overall effect size from 0.077 (fixed-effects) to 0.201 (random-effects; Table 2). The overall effect size is still significant but lower than the one estimated by fixed effects, and suggests that after chilling the *Salmonella* prevalence is reduced on average by a factor of ~ 1.62 ($\Theta = -0.485$ in Table 2). Accounting for the heterogeneity in the true log relative risks between abattoirs ($\tau^2 = 0.548$) led to a meta-analysis with better fit quality than the fixed-effects model, as indicated by the lower log-likelihood and Bayesian Information Criterion (BIC).

Table 2: Results of the Abattoir-Level Meta-Analysis Models for the Risk of *Salmonella* Prevalence on Pig Carcasses After Chilling Relative to Before Chilling

Model	Fixed-effects	Random-effects	Multilevel
Parameters			
Intercept (Θ , β_0)	-0.550 (0.077)***	-0.485 (0.201)*	0.607 (0.612) ^{ns}
# visits in abattoir (β_1)			-0.589 (0.273)*
Heterogeneity			
Q test	107.5 (df=31)***		
τ^2		0.548	0.331
I ²		68.3%	
H ²		3.15	
QM moderators			4.66 (df=1)*
QE residual heterog.			34.05 (df=25) ^{ns}
Goodness-of-fit			
Log-likelihood	-78.2882	-49.6887	-41.2337
BIC	160.0421	106.2453	92.1240

Significance codes: 0 '***' 0.001 '**' 0.01 '*' 0.05 '.' 0.1 ' ' Non-significant '^{ns}'

Other measures can be computed to facilitate the interpretation of the estimated amount of between-abattoir heterogeneity. The I^2 statistics or intra-class correlation estimates the proportion of between-study variance from the total variance. This is analogous to using the proportion of explained variance in standard regression models to indicate the importance of specific predictor variables. Hunter and Schmidt (1990) pointed out that with a large number of studies, the power of the significance test is high, and small variances will become significant. However, when the number of studies is small, lack of significance for τ^2 does not imply that the outcome are homogeneous. So, they propose a 25% rule of thumb; this is, if the intra-class variance is higher than 25% of the total variance, the variance between studies can be deemed as large enough to attempt to model it using available study characteristics. In our case, the intra-class correlation ($I^2=68.3\%$) underscored the presence of between-abattoir variance, and that consequently some study characteristics could be coded to attempt to explain such heterogeneity among the true

effects. The H^2 statistic is the ratio of the total amount of variability in the observed outcome to the amount of sampling variability (If $\tau^2=0$, then $H^2=1$). In this model, the H^2 ratio was 3.15 (Table 2). In contrast with the fixed-effects solution, the overall effect size – or incidence reduction ratio due to chilling (95% CI: 1.09 – 2.41) – obtained by the random-effects approach can be generalised beyond the specific set of abattoirs at hand, and this is also sustained by the unlikely presence of publication bias. This will be later discussed.

The power of multilevel meta-analysis becomes apparent when attempting to model the significant differences in the abattoir outcomes. We hypothesised that as an abattoir was visited more number of times (i.e., sampled more), the effect size of chilling on *Salmonella* occurrence became more clear and larger; and that at least part of the heterogeneity found between abattoirs may be due to the influence of the number of sampling visits (N_v) defined in the experimental design of the primary studies. The results of the multilevel

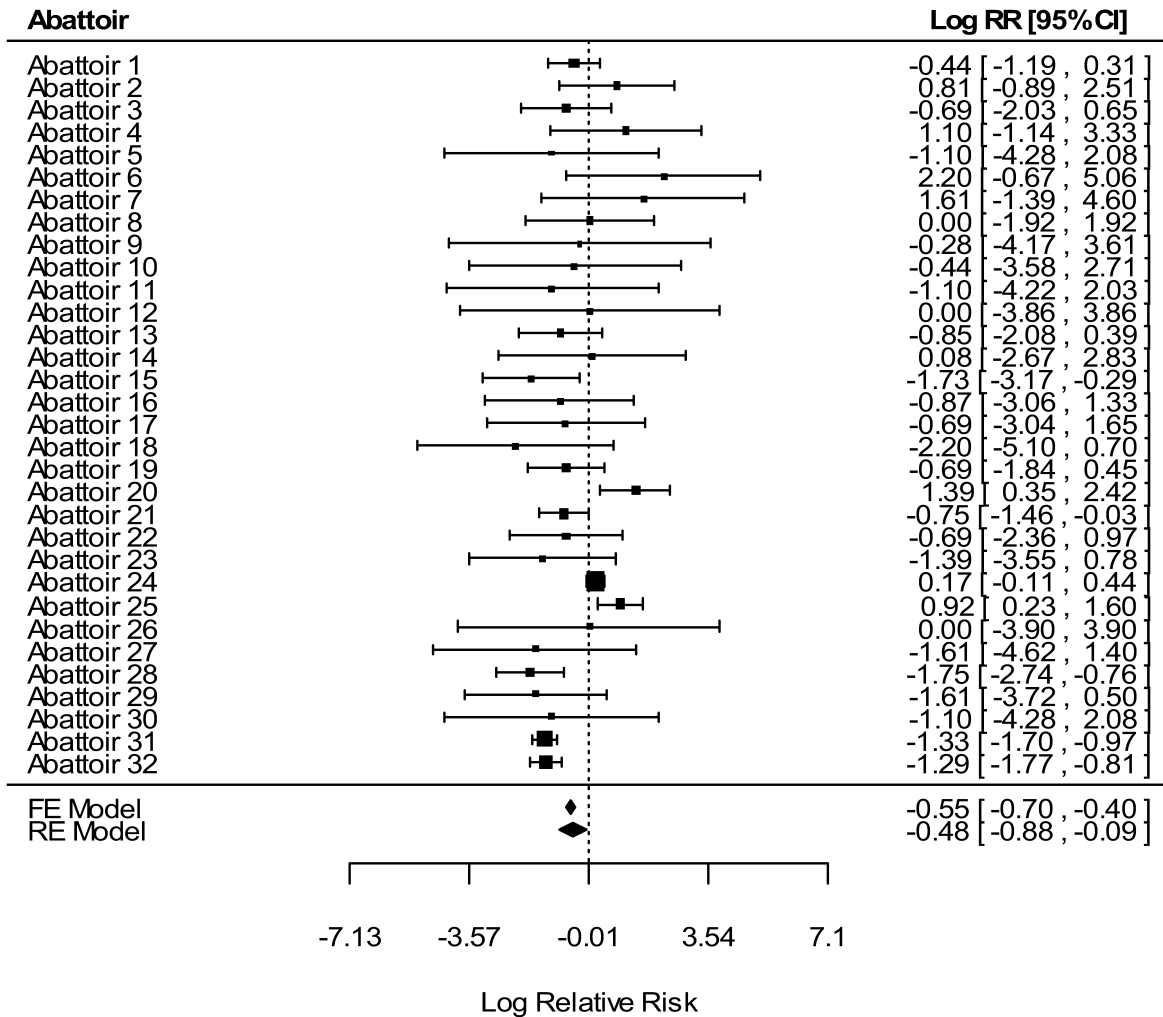


Figure 1: Forest Plot of the Risk of *Salmonella* Prevalence on Pig Carcasses After Chilling relative to Before Chilling. Primary Study Estimates and Overall Fixed and Random Effects are shown with 95% Confidence Intervals

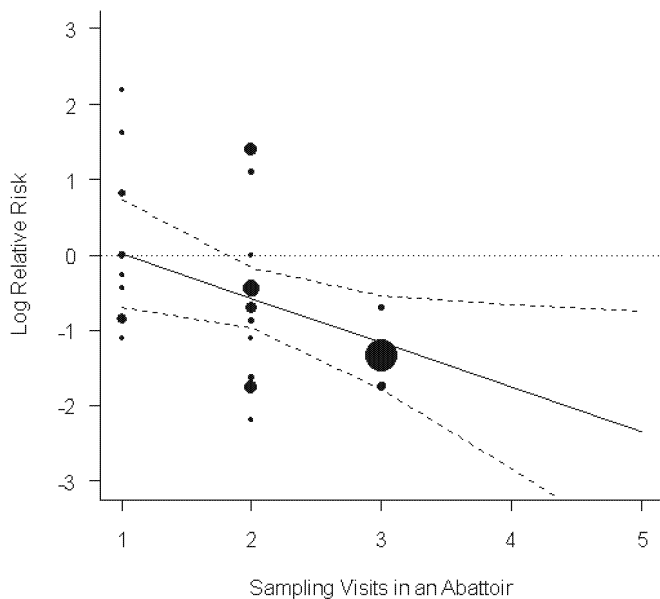


Figure 2: Effect of the Number of Sampling Visits in a Study Experimental Design on the Estimation of the Effect of Chilling on *Salmonella* Incidence on Pig Carcasses

model (Table 2) showed that, apparently, our estimate of the effect size of chilling is subject to the number of times an abattoir is visited. This is supported by the significant coefficient β_1 and the significant QM test for the moderating variable. In the multilevel model, the estimated amount of residual heterogeneity is $\tau^2=0.331$, suggesting that 39.6% $(0.548-0.331)/0.548$ of the total amount of heterogeneity between abattoirs can be accounted for by including the ‘number of sampling visits’ in the model. The QE statistic indicates that the residual heterogeneity is no longer significant. However, we can assume that the number of sampling visits per abattoir may be accounting for some of the between-abattoir variability, and that other non-coded study characteristics may be also noteworthy.

The value of the coefficient β_1 indicates that an increase in one sampling visit in abattoir corresponds to a change of -0.589 units in terms of the average log relative risk (Table 2). Because the abattoir outcome depends on the number of sampling visits, reporting an overall effect size does not convey the relevant information. To facilitate the interpretation of the moderator, predicted average log relative risks for different number of sampling visits can be reported. Figure 2 shows a plot of the log RR as a function of the number of sampling visits. The observed RR are drawn proportional to the weights, and predictions are shown with corresponding 95% confidence interval bounds. Results suggest that when an abattoir is sampled only once, the observation of an effect (either increasing or decreasing) is inconsistent, and therefore, on average no effect is observed (notice that on average the Log RR is zero when one sampling visit is performed). Seemingly, the decreasing effect of chilling on the *Salmonella* prevalence becomes noticeable (and significant) with at least two sampling visits. These interesting results may be explained by the fact that, although *Salmonella* viability has been proven, at least

at laboratory level, to be affected by both temperature (cold shock and refrigerated storage) and water activity (osmotic shock); still the efficacy of the chilling operation for the reduction of *Salmonella* is also affected by other equally important factors, related to chilling systems, abattoir logistics, cross-contamination, abattoir hygiene, etc. In addition, *Salmonella* cells are not homogeneously distributed on carcasses, which will greatly add to the *uncertainty* in the measured outcomes (i.e., although a pre-chill carcass may contain *Salmonella* cells, swabbing a *Salmonella*-free area will lead to a negative result). On the other hand, the pre-chill and post-chill measurements were most of the times performed on different carcasses, which adds extra randomness to the measured outcome. Thus, it is then expected that, with so many factors affecting the efficacy (and the measurement itself of the efficacy) of the chilling operation, results from only one abattoir visit made up of an average of 30 pig carcasses, will not be sufficient to consistently elucidate any effect. Results from the multilevel meta-analysis indicated that a significant reduction ratio (~ 1.77) of chilling on the *Salmonella* incidence on pig carcasses was observed with at least two sampling visits consisting of a total of 50 carcasses on average. A greater *Salmonella* incidence reduction ratio (~ 3.20) was noticed with data from three sampling visits (Figure 2). This meta-analysis model however is not supposed to be extrapolated for four or more sampling visits, as the number of sampling occasions is not a continuous variable but a categorical one.

An important problem in meta-analysis is the so-called file drawer problem or publication bias. The data for a meta-analysis are the results from previously published studies. Studies that find significant results may have a larger probability to be published. As a result, a sample of published studies can be biased in the direction of reporting large effects. An approach to investigate publication bias is by means of a funnel plot which is a plot of the effect sizes versus their standard errors. If the sample of available studies is ‘well behaved’, this plot should have the shape of a funnel. The outcomes from smaller studies (normally of higher standard errors) are more variable but estimate the same underlying population parameter. If large effects are found predominantly in smaller studies, this indicates the possibility of publication bias, and the possibility of many others insignificant small studies remaining unpublished (Hox and De Leeuw 2003). In the case of multilevel models with moderating variables, the funnel plot should not be based on the observed outcomes (i.e., effect sizes versus standard errors) because part of the variability in the plot could be due to the explanatory study characteristics. Thus, it is more appropriate to use a funnel plot after removing the covariate effects. Figure 3 shows a funnel plot of the effect size residuals against their corresponding standard errors, and does not suggest evidence of publication bias.

CONCLUSION

Both the fixed-effects and random-effects model confirmed the effect of chilling in decreasing *Salmonella* incidence; although the random-effects model was preferred to account

for the high variability observed among the 32 abattoirs surveyed in the 13 primary studies. As a funnel plot suggested no evidence of publication bias, it can be safely generalised that the chilling effect reduces the incidence of *Salmonella* by a factor of 1.62 (95% CI: 1.09 – 2.41) in relation to the occurrence in pre-chill pig carcasses. The heterogeneity in effect size between surveyed abattoirs ($\tau^2=0.548$), investigated by means of a multilevel model, revealed that the ‘number of sampling visits’ performed in an abattoir is a study characteristic that has a major influence on the estimated chilling effect. This moderating variable (covariant) explained 40% of the between-abattoir variability, and revealed that only one sampling visit – consisting of an average of 30 carcasses – was not sufficient to consistently elucidate any chilling effect; most likely because of the many factors influencing both the efficacy of the chilling operation (i.e., chilling systems, abattoir logistics, proximity between carcasses, cross-contamination, etc.) and the measurement itself (i.e., heterogeneous distribution of bacterial cells on carcasses; uncertainties associated with the different carcasses sampled before and after chilling; and with the microbial test protocol). The beneficial effect of chilling became only evident in a consistent way with at least two sampling visits per abattoir; this is with higher sample sizes that could surmount the different sources of variability and uncertainty affecting the efficiency of the chilling operation. Meta-analysis applications such as the one conducted in this study are of importance in the development of risk assessment models; in the design of future statistically-sound incidence surveys in abattoirs, and ultimately in the compilation and better understanding of the differing outcomes found by primary studies.

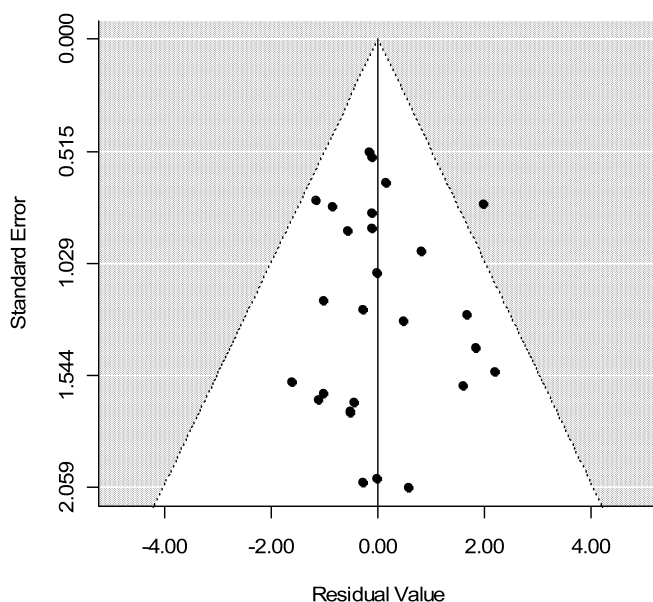


Figure 3: Funnel Plot of the Residuals of the Risk of *Salmonella* Prevalence on Pig Carcasses After Chilling relative to Before Chilling

REFERENCES

- Algino R. J.; G. A. Badtram ; B. H. Ingham; and S. C. Ingham. 2009. “Factors Associated with *Salmonella* Prevalence on Pork Carcasses in Very Small Abattoirs in Wisconsin”. *Journal of Food Protection* 72, No. 4 (Apr), 714-721.
- Arguello, H. ; A. Carvajal; J. A. Collazos; C. Garcia-Feliz; and P. Rubio. 2012. “Prevalence and Serovars of *Salmonella enterica* on Pig Carcasses, Slaughtered Pigs and the Environment of Four Spanish Slaughterhouses”. *Food Research International* 45. No. 2 (Mar), 905-912.
- Botteldoorn, N.; M. Heyndrickx; N. Rijpens; K. Grijspeerdt; and L. Herman. 2003. “*Salmonella* on Pig Carcasses: Positive Pigs and Cross Contamination in the Slaughterhouse”. *Journal of Applied Microbiology* 95, 891-903.
- Bouvet, J.; C. Bavai ; R. Rossel ; A. Le Roux ; M. P. Montet ; C. Mazuy ; and C. Vernozy-Rozand. 2003. “Evolution of Pig Carcass and Slaughterhouse Environment Contamination by *Salmonella*”. *Reviews Veterinary Medicine* 154, No. 12 (Dec), 775-779.
- Cutter, C. 2003. “Effects of Commercial Chilling Methods for Reducing Bacteria on Pork Carcasses”. In *Research Report Pork Safety*. National Pork Board, Des Moines, Iowa.
- Davies, R. H.; I. M. McLaren; and S. Bedford. 1999. “Distribution of *Salmonella* Contamination in Two Pig Abattoirs” In *Proceedings of the 3rd International Symposium on the Epidemiology and Control of Salmonella in Pork* (Washington DC, USA) 267-272.
- De Busser, E.V.; D. Maes; K. Houf; J. Dewulf; H. Imberechts; S. Bertrand; and L. De Zutter. 2011. “Detection and Characterization of *Salmonella* in Lairage, on Pig Carcasses and Intestines in Five Slaughterhouses”. *International Journal of Food Microbiology* 145, 279-286
- Duggan S. J.; C. Mannion; D. M. Prendergast; N. Leonard; S. Fanning; U. Gonzales-Barron; J. Egan; F. Butler; G. Duffy. 2010. “Tracking the *Salmonella* Status of Pigs and Pork from Lairage through the Slaughter Process in the Republic of Ireland”. *Journal of Food Protection* 73, No. 12 (Dec), 2148-2160.
- Epling, L. K.; J. A. Carpenter; and L. C. Blakenship. 1993. “Prevalence of *Campylobacter* spp. & *Salmonella* spp. on Pork Carcasses and the Reduction Affected by Spraying with Lactic Acid”. *Journal of Food Protection* 56 ,No. 6 (Jun), 536-537.
- Glass, G. V. 1976. “Primary, Secondary and Meta-analysis of Research”. *Educational Researcher* 5 (1, 3): 3-8.
- Gonzales Barron, U.; D. Bergin; and F. Butler. 2008. “A Meta-analysis Study of the Effect of Chilling on *Salmonella* Prevalence on Pork Carcasses”. *Journal of Food Protection* 71, No. 7 (Jul), 1330-1337.
- Hedges, L. V.; and J. L. Vevea. 1998. “Fixed- and Random-Effects Models in Meta-Analysis. *Psychological Methods* 3, 486-504.
- Hox, J. J.; E. De Leeuw. 2003. “Multilevel Models for Meta-Analysis”. In *Multilevel Modelling: Methodological Advances, Issues and Applications*, S.P. Reise and N. Duan (Eds.). Lawrence Erlbaum Associates, NJ, 90-111.
- Hunter, J. E; and F. L. Schmidt. 1990. „Methods of Meta-Analysis: Correcting Error and Bias in Research Findings”. Sage, Newbury Park, CA.
- Oosterom, J.; R. Dekker; G. J. A. de Wilde; F. van Kempen-de Troye; and G. B. Engels. 1985. “Prevalence of *Campylobacter jejuni* and *Salmonella* during pig slaughtering”. *Veterinary Quarterly* 7, No. 1 (Jan), 31-34.
- Raudenbush, S. W.; A. S. Bryk. 1985. “Empirical Bayes Meta-Analysis”. *Journal of Educational Statistics* 10, 75-98.
- Sargeant, J. M.; M. Amezcua; A. Rajic; and L. Waddell. 2005. “A guide to conducting systematic reviews in agri-food public

health". Food Safety Research and Response Network, Canada.

Viechtbauer, W. 2010. "Conducting Meta-Analyses in R with the 'Metafor' Package". Journal of Statistical Software 36, No. 3 (Aug), 1-48.

BIOGRAPHIES

Dr. URSULA GONZALES BARRON is a senior researcher at the School of Biosystems Engineering, University College Dublin (UCD), Ireland. Her expertise resides in the mathematical aspects of food safety such as risk assessment modelling and predictive microbiology. Other interests are the use of meta-analysis and Bayesian

statistics in food safety, zero-modified count data models for microbial counts, acceptance sampling and statistical process control for microbial load, as well as food traceability.

Dr. VASCO CADAVEZ is an Adjunct Professor at the Department of Animal Science of the Polytechnic Institute of Braganza (IPB), Portugal. His research interests include carcass and meat quality, with special emphasis on the development of mathematical models for the prediction of carcasses composition. Since 2009, he acts as Principal Investigator of the Food Safety and Technology Research Group at the Mountain Research Centre (CIMO), IPB.

FOOD PACKAGING

MODELLING AND NUMERICAL SIMULATION OF WATER VAPOUR SORPTION KINETICS IN HUMIDITY REGULATING POLYPROPYLENE FILMS CONTAINING SODIUM CHLORIDE

Solange Sanahuja
Oliver Miesbauer
Ellen Reichmann
Sven Sangerlaub

Department of Materials Development
Fraunhofer Institute for Process Engineering and Packaging (IVV)
Giggenhauser Strae 35
D 85354 Freising, Germany
E-mail: oliver.miesbauer@ivv.fraunhofer.de

KEYWORDS

Water vapour diffusion, Finite element method, Food packaging film, Humidity regulation, Sodium Chloride.

ABSTRACT

This study proposes a mathematical time-dependent model to examine the humidity sorption kinetics and the storage capacity of a porous packaging polymer material (PP) containing NaCl as hygroscopic substance. Water vapour pressure gradient was chosen as the principal driving force for the transport of water vapour in the film. Solving the diffusion equation numerically by the finite element method resulted in the evolution of water vapour contents calculated inside humidity regulating film specimens. The influence of the diffusion and the sorption coefficients of the polymer, and of the thickness and the NaCl content of the film on kinetics and capacity of the humidity regulating films could be determined. By comparison of the calculated amount of absorbed water vapour with experimental data, a good agreement between the predicted tendencies of the numerical and experimental results was found. The model was validated in a region of the salt's sorption isotherm above the deliquescence point of NaCl and significantly below the humidity at which the holes in PP are completely filled with water. The results permit to develop optimized humidity regulating films for individual food requirements. Application of this model could facilitate the development of these active films using different polymers and hygroscopic substances.

INTRODUCTION

One of the main functions of packaging is to protect the filling (Piringer 1993). Packed food's shelf life and quality are decisively affected by the air humidity within the packaging headspace (Hofstetter et al. 1991). To Abbas et al. (2009), reactions of food components involved in food spoilage occur above a certain food's water activity of about 0.3 for enzymatic reactions and 0.7 for microbial growth (mold, yeast, bacteria). Finally, a significant part of the waste could be avoided thanks to adequate packaging which can regulate humidity to the level ensuring optimal

preservation conditions of packed food. However, up to now, most of packaging materials are passive: they cannot regulate and stabilize the relative humidity in the packaging (Langowski et al. 2003; Sangerlaub et al. 2010). The amount of spoiled foodstuffs, resulting from inadequate relative humidity inside the packaging (Buchner 1999) could be drastically reduced by humidity regulating packaging systems.

CONCEPT OF HUMIDITY REGULATING FILMS

Within the project "Feuchteregulierende Verpackung zur Verbesserung der Qualitat und der Haltbarkeit von Lebensmitteln" (Bavarian Research Foundation), humidity regulating food packaging films were developed.

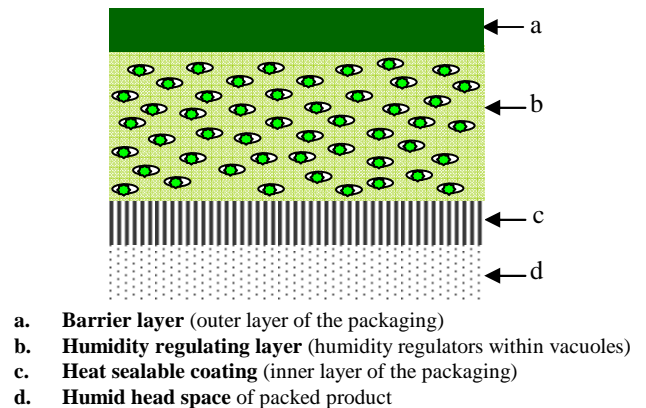


Figure 1: Design of the Humidity Regulating Multi-layer film. (Adapted from Sanahuja 2010)

The optimal relative humidity (r.h.) for fruits, vegetables, mushrooms and meat varies between 90 and 97%, or 85 to 95% particularly for tomatoes, or 75 to 85% for soft cheese (Gross 2004). Therefore the composition of the packaging material has to be adapted in order to reach the optimal humidity in food's atmosphere for the whole storage time, preventing moistening, but also drying-out of fresh food (Stehle 1989) and condensation. Adequate hygroscopic substances, dispersed into a polymer layer of the humidity regulating packaging film (Figure 1), are able to adsorb or

desorb water vapour when the humidity is modified until the equilibrium moisture content is reached. However, the polymer cannot store the whole aqueous solution obtained from the deliquescence of those crystals (Buchner 1999). Consequently, pores must be integrated into the polymer (Sangerlaub et al. 2011), by means of polymer processing techniques such as foaming, stretching or deep drawing the material containing such hygroscopic substances. By combination of these processes with coextrusion, coatings or lamination, it is possible to produce multi-layer films for the required packaging type. For example, multi-layer films for tubular bags or trays are appropriate packaging types for fruits and meat pieces. In this study, the hygroscopic substance chosen is sodium chloride (NaCl), because it is allowed by the food law, easily available and cheap. Further it can be well crushed, it is chemically inert and thermally stable. The sorption isotherm of NaCl (Figure 2) shows that it begins to absorb water vapour reversibly at a r.h. of 75.5% which is known as the deliquescent humidity at 23°C (Labuza et al. 1998). At this r.h. it absorbs up to 278 mass percent (m%) water without showing a change in its water activity while turning into aqueous solution. Thus it has the potential to regulate the ambient humidity at about 75-85%, which corresponds to the domain of optimal water activity for the preservation of several humid foods. This is true even if temperature fluctuates from 7 to 23°C during unadequate transports, as temperature has little influence on the sorption behaviour in the domain of 75.5 to 90% r.h..

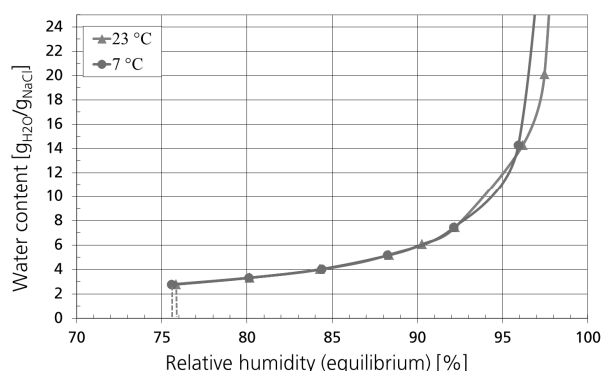


Figure 2: Sorption isotherm of sodium chloride. (Sangerlaub et al. 2011)

MODEL OF THE HUMIDITY REGULATING FILM

Modelling the water vapour transport behaviour is important to understand the phenomena of humidity regulation by porous packaging materials containing hygroscopic substances. The important kinetics of ab- and desorption of humidity and capacity of the film depend on several film geometry and material parameters. So, corresponding simulations are essential to improve the performance of those innovative films, permitting to find rapidly the optimal parameters to set for specific food packaging production.

Permeation Problem

When a polymeric film is in contact with different water vapour pressures at its both surfaces, water vapour permeates through it from the side with higher to the side

with lower value (Comyn 1994). This permeation process is divided into several steps (Langowski 2008): adsorption of vapour at the phase interface between the polymer and ambient air; then absorption and dissolution in the polymer; followed by diffusion through it and desorption at the other side. Temperature, polymer permeability to water vapour and gradient of its concentration influence the speed of permeation. In the model the polymer is characterized by two properties which are relevant for the transport of water in the material: the diffusion coefficient D and the sorption coefficient S .

Sorption Problem and Storage of Water Vapour

The considered model describes a film whose permeable inner sealable layer is in contact with the food headspace (Figure 1 & 3). At this interface exchange of water vapour between film and headspace sorption is possible, permitting humidity regulation. In order to eliminate the influence of the environment the film is isolated at the outer side of the packaging. As sorption processes happen very quickly in comparison to diffusion processes (Hanika 2004), the time needed for the adsorption and dissolution processes of water vapour in the matrix were neglected in the model (Reichmann 2010). The relation between the partial pressure of water vapour at the surface of a material and the concentration of water dissolved in the material is described by the sorption isotherm. For sorption of water vapour in polypropylene (PP), a semi-crystalline polymer which is considered in this paper, Henry's law is valid: concentration c is proportional to partial pressure (Langowski 2005).

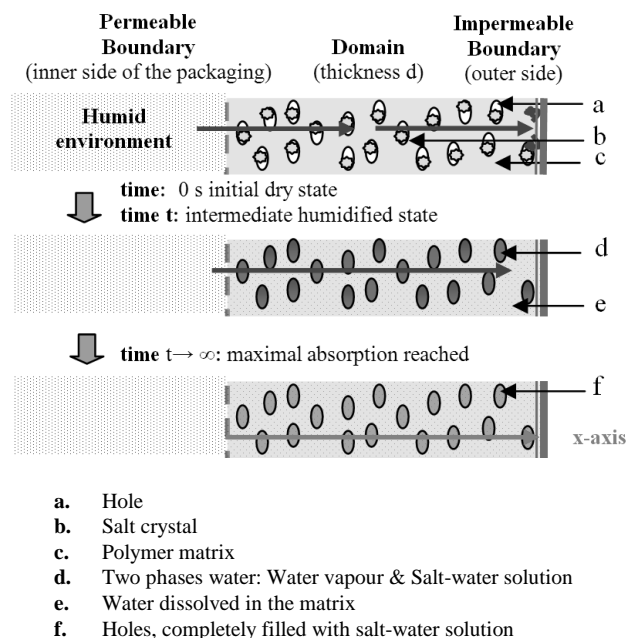


Figure 3: Geometric Model with representation of the 1-dimensional cut and evolution in time. (Adapted from Sanahuja 2010)

Diffusion Problem

According to Lindemann (1983), mass balance equations can be used to describe diffusion problems. Due to the flow processes, the concentration of water vapour changes

depending on time and space. As a consequence, this is also true for the concentration gradient $\text{grad}(c)$. In the case that Henry's law is valid, Fick's first law is the fundamental law of diffusion (Comyn 1994). It states that the flux density is proportional to $\text{grad}(c)$. Combination with the continuity equation which describes the conservation of the amount of diffusing substance gives Fick's second law of diffusion, describing well the non-steady state. This diffusion equation (1) simplifies to diffusion in one dimension (x) because the film is considered as homogeneous in y- and z-directions:

$$\frac{\partial c}{\partial t} = D \cdot \left(\frac{\partial^2 c}{\partial x^2} + \frac{\partial^2 c}{\partial y^2} + \frac{\partial^2 c}{\partial z^2} \right) \quad (1)$$

According to Peterlin (1985), equation (1) can be used for most polymers except for the case that the sorbent modifies the volume and the composition and hence the transport properties of the system. That is why an ideal behaviour of the polymer is supposed: D and S are independent of concentration of the diffusing substance, position and time. This assumption is fulfilled for the diffusion of water vapour in PP. In order to describe both the absorption of water vapour in the PP matrix and by NaCl within the holes, the dual-mode sorption model for the sorption of substances in micro porous glassy polymers like polyethylene terephthalate (PET) is adopted (Shigetomi et al. 2000). To Stern et al. (1990), this model (2) postulates that a substance like CO₂ dissolved in a glassy polymer consists of two distinct molecular populations which are in local equilibrium in two different morphological regions of the polymer. The total concentration c of the dissolved penetrant at given pressure and temperature is the sum of concentrations in the polymer matrix c_D obeying to Henry's law and in the holes c_H related to the Langmuir adsorption theory:

$$c = c_D + c_H \quad (2)$$

Different models were established for problems in relation to sorption of vapours or gases in porous media containing hygroscopic substances (Espinosa et al. 2008; Fan 2005). As the headspace atmosphere of packed products can be considered as static, convection at the permeable side is not taken into account in the study of humidity regulating films. Furthermore, no convection of air humidity through the film was considered, because it contains only small isolated pores (but no capillaries or fibres studied by Nield et al. 2006). Finally, no direct transport of water between adjacent holes is possible in the present model since these are assumed not to be connected with each other. Therefore the driving force for diffusion of water vapour in the material is the gradient only of c_D and so $\partial^2 c / \partial x^2$ in equation (1) does not include the term c_H for water in the holes. But as the total concentration of water vapour is the sum of both concentrations as inspired by the dual sorption model, the change of total concentration of water vapour in the film at time t is given by a new diffusion equation (3):

$$\frac{\partial c}{\partial t} = \frac{\partial c_D}{\partial t} + \frac{\partial c_H}{\partial t} = D \cdot \frac{\partial^2 c_D}{\partial x^2} \quad (3)$$

To make it possible to implement it in Femlab[®], it must be rewritten with only one unknown parameter: c_H is expressed as a function of c_D. Henry's law is valid in the polymer matrix for c_D's linear sorption isotherm (4) with the partial pressure of water vapour p and the material specific sorption coefficient S_{c_D}:

$$p = \frac{c_D}{S_{c_D}} \quad (4)$$

The pores and the humidity regulator NaCl therein are supposed to be homogeneously spread within the film, but they are not incorporated geometrically in the model. Instead of this, only the polymer matrix is modelled geometrically, and NaCl in the holes is included in the model by its sorption isotherm. As this one is non-linear, the sorption behaviour of the film depends strongly on the deliquescence humidity of NaCl. So, the sorption coefficient within the holes S_{c_H}(p) is not constant and depends on p (5):

$$p = \frac{c_H}{S_{c_H}(p)} \quad (5)$$

The sorption isotherm of the humidity regulating films is the sum (2) of the two sorption isotherms described by (4) and (5). To determine c_H (Figure 4) as a function of c_D equations (4) and (5) are combined:

$$c_H = p \cdot S_{c_H}(p) = \frac{c_D}{S_{c_D}} \cdot S_{c_H}(p) \quad (6)$$

The resulting diffusion equation (7) is then obtained by inserting (6) into (3):

$$\frac{\partial c}{\partial t} = \left(1 + \frac{\partial c_H / \partial p}{S_{c_D}} \right) \cdot \frac{\partial c_D}{\partial t} = D \cdot \frac{\partial^2 c_D}{\partial x^2} \quad (7)$$

The amount of salt is fixed for each simulation and implemented in the model through an effective sorption isotherm that describes the relation between c_H and p.

As the pores are dispersed quasi-continuously in the film, the porosity of the film (= holes' total volume V_H divided by the volume of the film V_{Film}) is independent of the position in the layer. The available volume for water accumulation has to be considered in the model, because c_H would increase to impossible values following an increasing concentration c_D if V_H was not limited. So, NaCl can absorb water vapour until the pores are completely filled with the salt solution. Therefore, the maximal possible concentration c_{Hmax} is reached for a particular volume fraction of holes in the film V_{H%}. After this maximal concentration for water in the holes is reached, it is presumed that the sorption isotherm continues as a linear function with the slope 0 (Figure 4). Thus, the concentration is constantly c_{Hmax} even if the water vapour pressure increases more. A more realistic model would respect the finite volume of the holes by combination of a Langmuir type sorption behaviour with the sorption isotherm (5) of the salt.

A phase change from gaseous to liquid occurs due to the absorption of water vapour by the salt crystals that dissolve in the aqueous phase (Figure 3). So, three fractions of absorbed water are in balance: water vapour dissolved in the polymer, and gaseous plus liquid water in the pores. The gaseous state was neglected because of its small density compared to the density of liquid water. But the phase change reaction takes time, which could influence the velocity of the sorption phenomenon.

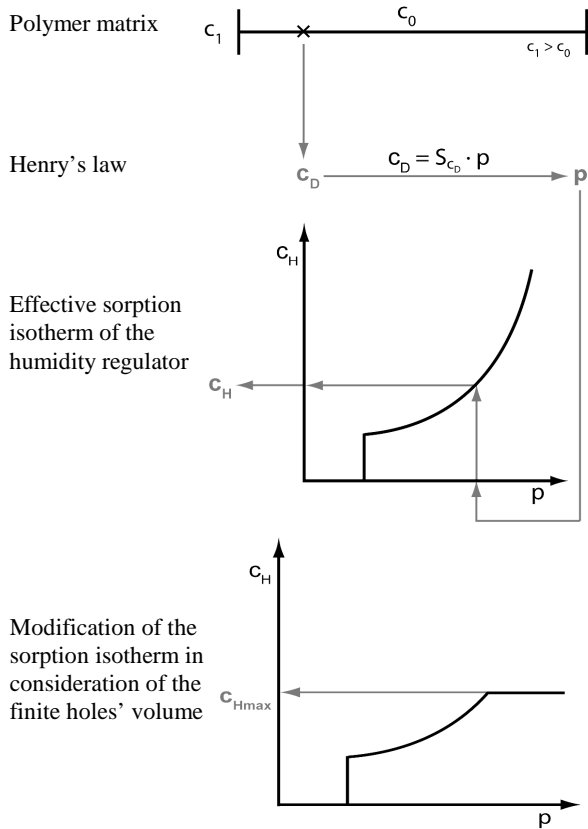


Figure 4: Procedure to determine c_H , with c_0 the concentration of water vapour in the film at the beginning and c_1 constant at the permeable side. (Reichmann 2010)

METHODOLOGY: FEM FOR SIMULATIONS

To estimate the time-evolution of present dynamic model, the non-linear differential equations are not analytically soluble but need numerical approximation (Lindemann 1983). The numerical calculation was based on the Finite Element Method (FEM) used by the software Femlab[®] from Comsol Multiphysics (Comsol AB 2001). It allows modelling based on Partial Differential Equations (PDE) in an interactive environment, Matlab[®]. The FEM discretises the geometry of a model, its equations, the boundary and subdomain conditions and, in parallel, the time. The one-dimension process occurs along the x-axis (cross section in Figure 3) which gives the coordinates through the film. Choosing adequate time stepping and mesh resolution permits to optimise the accuracy of the numerical solutions with the lowest possible computational time.

The modelled system was described by initial, boundary and subdomain conditions as well as diverse parameter values. Boundary settings were made according to equation (8) for a general diffusion model with the outward unit normal vector n , the flow vector Γ , the transpose T , the

Lagrange multiplier μ and the dependent variable u for which the system is resolved:

$$-n \cdot \Gamma = G + \left(\frac{\partial R}{\partial u} \right)^T \cdot \mu \tag{8}$$

The outer boundary of the humidity regulating film is supposed to be ideally impermeable to water vapour. Thus, the Neumann boundary settings are valid on this side. As there is no flow through the outer face, $-n \cdot \Gamma = 0$. R is fixed to be 0, so that $-n \cdot \Gamma = G$. As a consequence, $G = 0$. On the inner side of the film, Dirichlet boundary settings are valid. As water vapour pressure stays constant, the concentration is always c_1 at this side: $u = c_1$ so $R = c_1 - u$. Each parameter of equation (7) was defined in relation with the considered “General PDE Form” (9) of Femlab[®] for the subdomain settings with the pre-factor d_a (mass coefficient) and the source term F :

$$d_a \cdot \frac{\partial u}{\partial t} + \nabla \cdot \Gamma = F \tag{9}$$

The experimentally measured sorption isotherm of NaCl was interpolated with the flinterpl piecewise cubic spline function for consistent smoothing.

RESULTS OF SIMULATIONS AND DISCUSSIONS

Since the vertical part of the isotherm at the deliquescence point of NaCl at 75.5% r.h. cannot be described by the considered model, simulations were performed only at relative humidities above this value. Simulations considered water vapour sorption in a homogeneous PP-layer with NaCl in pores and isolated at the outer side.

Check of Model reliability

To check the validity of the model, graphical post-processing was permanently done. For example, the concentration of water vapour at the beginning is minimal in the whole layer, except at the permeable side (Figure 5). Then, concentration increases to the value of concentration at the permeable side, but more rapidly for points near to this boundary.

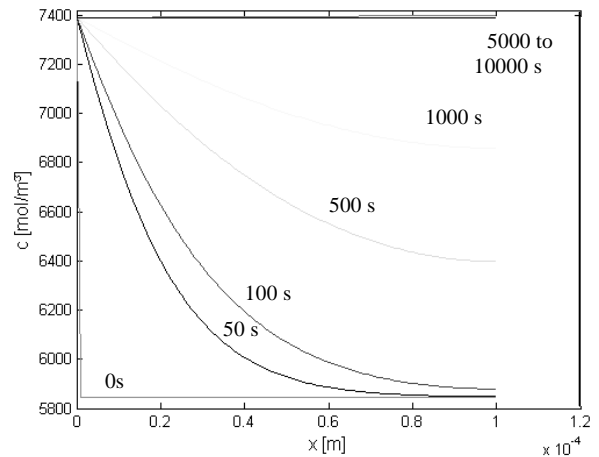


Figure 5: Example of evolution of the total concentration of water vapour in the film versus coordinates. (Adapted from Sanahuja 2010)

It could be shown that the amount of water stored in the film is clearly determined by the storage in the holes, as they contain about ten thousand times more water than the amount dissolved in the polymer matrix.

Simulations without consideration of the gaseous state of water in the holes give about the same results in kinetics (no significant change: 0.26% slower for a test with 5 m% NaCl, $V_{H\%}=15$ and an initial r.h. gradient between the film and head space of 80 to 85%) and nearly the same final capacity as with consideration of the gaseous state.

Influence of Material and Geometric Parameters

The influence of D , S , film-thickness (d) and NaCl content on storage capacity for water and sorption kinetics were studied and discussed within the possible limits of the model. The maximal capacity of the film, as well in the polymer matrix as in the holes, is not influenced by D , but the speed of absorption is proportional to D . The absorption phenomenon is also accelerated by higher S values, contrary to mono-material, because water vapour must go through the matrix to reach the individual pores. The maximal capacity of the matrix is proportional to S as it defines how much sorbent can be stored by the matrix, but not in the holes where it is the holes' volume and the salt content which determine the amount of stored water. The capacities of the water in the matrix and also in the holes are both proportional to the film thickness. Water capacity of the holes increases with the NaCl content, as far as the holes are not completely filled. However, even if the half-value times increase with thickness and salt content, the speed of sorption itself is not influenced by those parameters. In reality, it takes more time to store more water and reach the equilibrium.

Comparison of simulation with experimental results

Experimental results provide a possibility to verify and validate the developed model through comparisons with simulation results. Figure 6 shows the evolution in time of the mass percent of water absorbed in the film based on the film dry mass.

An absorption experiment was carried out with PP biaxially and simultaneously stretched with a factor 9 ($3*3$). The experiment was made at 23°C with totally dry films (0% r.h.) at the beginning in a constant 100% r.h. atmosphere where water vapour could enter on both sides of the samples to accelerate experimentation (Böhmer 2011). In contrast, simulations could only be run above 80% (i.e. above the deliquescence point of the salt). Moreover, since numerical errors were obtained due to the high slope of the isotherm and its sharp bend at that humidity where the holes are completely filled with aqueous salt solution, simulations were stopped at 85% and respectively 90% r.h.. Therefore, the initial r.h. of the film in the simulations is not 0% and sorption begins with about 10 m% absorbed water. So, due to the reduced gradient of water vapour partial pressure and to absorption that occurs at only one side, the sorption process is slower at the beginning for the simulations.

The experiment that could best fit to the possible simulation conditions was obtained with 3 m% NaCl and 9

m% calcium carbonate (CaCO_3), which is used as a filler material to create more holes while stretching. In fact, these holes are not supposed to contain NaCl and CaCO_3 should not absorb water, but canals may let those holes absorb the salt solution. Better imaging techniques could help determine to what extent capillary transfers could be an important factor for speed of sorption and final capacity. Finally, a film of thickness $d = 110 \mu\text{m}$ and with 18.65 volume percent of holes was obtained by stretching. Considering the error bars with 95% confidence level, the values with 3 m% NaCl and without CaCO_3 ($d = 110 \mu\text{m}$, $V_{H\%} = 6.38$) are not significantly different from those with filler material even if the samples with fewer holes should be filled faster and store fewer amount of solution. Considering the maximal humidity of 100% in contact with the samples, the film should absorb more than 60 m% water, but this was limited by the finite holes volume. Thus, the sorption process is about to be finished after 50 days with predictable 25 m% water in the samples with filler material. In the same way, considering a final humidity of 85% or 90%, simulations with 15 volume percent holes reach a maximal capacity of 13 and respectively 18 m% water.

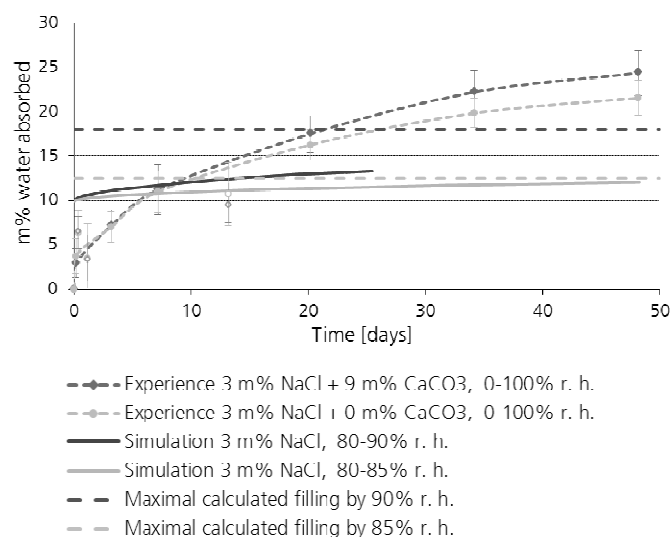


Figure 6: Comparison of experimental and simulation results. (Adapted from Sanahuja 2010)

SUMMARY

A model of water vapour sorption by a humidity regulating film from the head space inside a packaging was developed. In application, the film consists of a polymer (PP) layer with holes containing NaCl as hygroscopic substance and it is situated between a sealing layer at the inner side of the packaging and an outer barrier layer. In the model the sealing layer was not taken into account and the barrier layer was replaced by an ideal isolation against environment. Water vapour is absorbed by the salt above its deliquescence point resulting in a phase change to an aqueous solution. Thus, a thermodynamic equilibrium for three phases of absorbed water vapour was stated, which is present at the interface between polymer matrix and hole. The one-dimensional model considers the holes and the salt only by their sorption isotherms but not by a geometric

description. It examines the humidity transport within the film induced by a gradient of water vapour partial pressure and the humidity absorption by the polymer matrix and by the salt above its deliquescence point. The resulting diffusion equation was solved numerically using the finite-element method.

CONCLUSION

Simulations showed that the kinetics of humidity absorption and the capacity of the film depend on the dimensions of the packaging material, the amount of hygroscopic substances and pores in the polymer matrix, and the material characteristics of the polymer chosen. Results permit to optimise packaging design for the regulation of the humidity inside the multilayer polymer film systems according to the individual needs of fresh food products. The numerical results showed some deviation from the experimental ones, but they follow the same tendencies and give results in the same range, indicating that the model is satisfactory in the region of sorption isotherm of NaCl between its deliquescence point and a relative humidity which is significantly lower than that value where the holes are completely filled with aqueous salt solution. Application of this model could facilitate the development of these active films using different polymers and hygroscopic substances.

ACKNOWLEDGEMENTS

The authors wish to thank the Bavarian Research Foundation for the financial aid.

REFERENCES

- Abbas, K.A.; A.M. Saleh; A. Mohamed and O. Lasekan. 2009. *Journal of Food, Agriculture & Environment* 7(3&4): 86-90.
- Bavarian Research Foundation. "Feuchtereulierende Verpackung zur Verbesserung der Qualität und der Haltbarkeit von Lebensmitteln". AZ-737-07.
- Böhmer, M. 2011. "Untersuchung der Hohlraumbildung beim Recken regulatorhaltiger Kunststofffolien". Diploma thesis. Freising: Fraunhofer IVV, 74p.
- Buchner, N. 1999. "Verpackung von Lebensmitteln: Lebensmitteltechnologische, verpackungstechnische und mikrobiologische Grundlagen". Berlin: Springer Editor, 658p.
- Comsol AB. 2001. "Femlab® User's guide and introduction, Version 2.2"., Stockholm: COMSOL AB., 388p.
- Comyn, J. 1994. "Introduction to polymer permeability and the mathematics of diffusion", Chap. 1. In: Comyn, J. 1994. "Polymer permeability". Great Britain: Chapman & Hall Editor, 383p.
- Espinosa, R.M.; L. Franke; G. Deckelmann. 2008. *Construction and Building Materials*, 22: 1758-1773.
- Fan, J.T.; X.Y. Cheng. 2005. Part I & II, *Textile Research Journal*, 75(3): 187-196.
- Gross, K. C. (ed.). 2004. "The Commercial Storage of Fruits, Vegetables, and Florist and Nursery Stocks". USDA, Agriculture Handbook No. 66. (<http://www.ba.ars.usda.gov/hb66/contents.html>)
- Hanika, M. 2004. "Zur Permeation durch aluminiumbedampfte Polypropylen- und Polyethylenterephthalatfolien". Dissertation, Fakultät für Maschinenwesen, Lehrstuhl für Feststoff- und Grenzflächenverfahrenstechnik, TU München. Shaker Edition, 182p.

- Hofstetter, A.; E. Baumgartner; W. Blum et al.. 1991. "Wasseraktivität". Schweizerisches Lebensmittelbuch (SLMB) Kapitel 64, 15p.
- Labuza, T.P.; C.R. Hyman. 1998. *Trends in Food Science & Technology*, 9: 47-55.
- Langowski, H.-C.; G. Goldhan. 2003. *Kunststoffe*, German Plastics, 93(5): 70-74.
- Langowski, H.-C. 2005. *Vakuum in Forschung und Praxis*, 17(1): 6-13.
- Langowski, H.-C. 2008. "Permeation of gases and condensable substances through monolayer and multilayer structures". In: Piringer, O.G.; A.L. Baner. "Plastic packaging – Interactions with food and pharmaceuticals. 2". Weinheim: Wiley-VCH, 297-347.
- Lindemann, D. 1983. "Finite Berechnungsverfahren für instationäre Diffusionsprobleme". Düsseldorf: Fortschr.-Ber. VDI-Z Editor, Reihe 7 Strömungstechnik, 71, 151p.
- Nield, D.A.; A. Bejan. 2006. "Convection in porous media, 3rd. edition". New York: Springer Editor, 643p.
- Peterlin, A. 1985. *Colloid & Polymer Sci.*, 263: 35-41.
- Piringer, O.G. 1993. "Verpackungen für Lebensmittel - Eignung, Wechselwirkungen, Sicherheit". Weinheim: VCH Editor, 408p.
- Reichmann, E. 2010. "Numerische Simulation der Kinetik der Wasserdampfsorption in feuchtereulierenden Kunststofffolien". Bachelor thesis, Freising: Fraunhofer IVV, 92p.
- Sanahuja, S. 2010. "Modelling and numerical simulation of water vapour sorption kinetics in moisture regulating films". Diploma thesis, Freising: Fraunhofer IVV, 120p.
- Sängerlaub, S.; C. Hauser; K. Müller and K. Rieblinger. 2010. *Kunststoffe International*, 2: 28-30.
- Sängerlaub, S.; M. Böhmer; P. Singh; C. Stramm and H.-C. Langowski. 2011. "Humidity Regulating Packaging Materials". Tappi Place Conference Bregenz 2011, 6p.
- Shigetomi, T.; H. Tsuzumi; K. Toi; T. Ito. 2000. *Journal of Applied Polymer Science*, 76: 67-74.
- Stehle, G. 1989. "Lebensmittel verpacken". Remagen-Rolandseck: Milchwirtschaftler Fachverlag GmbH Editor, 519p.
- Stern, S.A.; S. Trohalaki. 1990. "Fundamentals of gas diffusion in rubbery and glassy polymers". Chap. 2, pp.22-59. In: Koros, W.J. 1990. "Barrier Polymers and Structures". Washington DC: the American Chemical Society, 406p.

AUTHOR BIOGRAPHIES

SOLANGE SANAHUJA was born in 1987 in France and went to the ENITIAA College, currently ONIRIS in Nantes, where she studied Food Science and Engineering and obtained her Diploma degree in 2010. Then she obtained her Master of Science degree for Food Technology and Biotechnology at the Technical University of Munich (TUM) in 2012.
Email: solange.sanahuja@gmx.de

OLIVER MIESBAUER studied Physics (Technical Physics) at the Technische Universität München (Diploma in 2002). Subsequently he studied Mathematics at the LMU Munich (Master of Science in 2005). Currently he is a scientist at the Fraunhofer Institute for Process Engineering and Packaging IVV where he works on the development of barrier materials for technical products and on the modeling of permeation mechanisms (Ph. D. Thesis).

ELLEN REICHMANN studied Packaging Technology (B.Eng. in 2010) at the Stuttgart Media University (HdM). Afterwards she graduated 2012 the Master's degree in Applied Surface and Material Sciences (M.Sc.) at the University Aalen and the University of Applied Sciences Esslingen. Since then she is working in Research and Development at the Robert Bosch GmbH, division Packaging Technology in Waiblingen.

SVEN SÄNGERLAUB, born in 1978, studied Packaging Technology at the Leipzig University of Applied Sciences (HTWK). He did a one year exchange programme at the Espoo-Vantaa-Institute of Technology, Helsinki, Finland. Since 2004, he is working at Fraunhofer IVV in the field of active and intelligent packaging.

PERMEATION THROUGH PASSIVE AND ACTIVE BARRIER MATERIALS – A CONTINUUM THEORETICAL APPROACH

Oliver Miesbauer
Department of Materials Development
Fraunhofer Institute for Process Engineering and Packaging IVV
Giggenhauser Straße 35
D-85354 Freising
Germany
E-mail: oliver.miesbauer@ivv.fraunhofer.de

KEYWORDS

Polymer, Barrier layer, Permeation, Diffusion, Sorption

ABSTRACT

A continuum theoretical model for the permeation of oxygen and water vapour through multilayer barrier structures will be presented. Permeation through polymers is described by the solution-diffusion model. Examples to be considered are the permeation through EVOH, the dual-mode sorption model and polymers containing inorganic particles. Afterwards it will be shown how passive and active barrier layers can be integrated into the model.

Oxygen permeation through nanoscale inorganic barrier layers is allowed only within defects. For water vapour also the inorganic matrix is defined as permeable. Some results obtained by the numerical simulation of oxygen and water vapour permeation through inorganic layers on polymers will be presented. It will be shown how the barrier properties can be further improved by the additional application of a polymeric layer.

Deliquescent substances dispersed within voids of a polymer can absorb a high amount of water vapour. A model for the permeation of water vapour through such materials was developed. Oxygen can be chemically bound by reaction with scavengers. Numerical simulation shows that such a layer has to be combined with a passive barrier layer.

INTRODUCTION

Products like food, pharmaceuticals and organic electronic devices contain components which are very sensitive to substances of the environment, especially to oxygen and water vapour (Robertson 2006; Baner and Piringir 2008; Lewis and Weaver 2004). Nutrients can be oxidized due to contact with oxygen; absorption of water vapour can enhance microbial growth in food (Robertson 2006). Since these processes result in reduced food quality, packaging must protect sensitive products against oxygen and water vapour in order to ensure a sufficient shelf life.

BARRIER MATERIALS

Polymeric films provide a solution for food packaging which is flexible and of low weight and can be produced in cost-efficient roll-to-roll processes (Langowski 2008; Nentwig 2006). However, for many applications the barrier properties

of these packaging materials to oxygen and water vapour are not sufficient (Langowski 2008).

Therefore the permeabilities of polymeric films have to be reduced by combining them with barrier materials. Passive barrier materials possess a high resistance to the transport of molecules (Langowski 2008; Nentwig 2006). These are either barrier polymers or inorganic materials which are deposited as layers or integrated into polymers as particles. In contrast, active barrier materials improve the barrier properties of films by physical absorption or chemical bonding of permeating molecules (Nentwig 2006; Day 2008).

In general, packaging films contain several layers of polymeric and possibly also inorganic materials in order to combine barrier properties with other functionalities like sealability (Nentwig 2006). The design of packaging films aims for an optimal ratio between barrier performance, material amount and costs. Numerical simulation of gas and water vapour permeation through multilayer films can help to understand the barrier properties of materials and therefore to reduce the number of experiments.

CONTINUUM VS. MOLECULAR MODELS OF PERMEATION

Molecular dynamics allows to study permeation mechanisms on an atomic level (Müller-Plathe 1993; Stern and Trohalaki 1990). Thus the equations of motion for the molecules permeating through a material are solved numerically. Transport coefficients can be derived from the trajectories calculated for the molecules. However, due to high computation times molecular dynamics simulations currently are limited to systems in nanometer scale (Müller-Plathe 1993). In order to study permeation phenomena this is especially suited for structures like surfaces and defects or for homogeneous systems which can be represented by a section in nanometer scale.

For packaging films which have a thickness in micrometer scale continuum models of permeation are more suitable. Such models are based on transport equations which describe how the spatial distribution of a substance within a material evolves with time. Material properties related to these transport processes are characterized by transport coefficients which are determined by experiments or molecular simulations.

In the following chapter a continuum theoretical model of gas and vapour permeation through polymers will be pre-

sented. Afterwards it will be shown how inorganic and active barrier materials can be integrated into this model.

PERMEATION THROUGH POLYMERS

An important continuum theoretical description of the permeation through polymers is given by the solution-diffusion model. It divides the permeation process into the following four steps (Langowski 2008). When a gas or vapour is in contact with one surface of a polymeric film molecules of the substance are adsorbed at this surface and afterwards dissolved in the polymer. The concentration gradient causes diffusion of the substance to the opposite surface where it is desorbed into gas phase.

In the following sections the sorption and diffusion processes are described in more detail. Afterwards two important examples will be considered: oxygen permeation through EVOH and the dual-mode sorption model. Finally the model of permeation through polymers will be extended to polymeric multilayer films.

Sorption at polymer surfaces

We consider the sorption of a gas or vapour from the atmosphere at a material surface. There the substance concentrations C in the atmosphere and c in the material in thermal equilibrium are related by the Nernst distribution law $c = K C$ (Rogers 1985). In general, the distribution coefficient K will be a function of c and of the temperature. For a defined temperature the sorption isotherm $c = S(p) p$ (Rogers 1985) of the substance can be obtained from the distribution law. The sorption behavior is characterized by the sorption coefficient S which is dependent on the partial pressure p of the substance in the atmosphere.

Four important types of sorption isotherms occurring in polymers are shown in (Rogers 1985). In the case of an ideal dilute solution Henry's law is valid: the sorption coefficient is a constant and therefore c is proportional to p . The Langmuir isotherm appears when sorption preferably takes place at specific sites in the polymer, e.g. functional groups, voids or porous particles. Due to their limited number a saturation of the absorbed substance is obtained at a certain concentration. The Flory-Huggins isotherm is obtained either when the absorbed substance plasticizes the polymer and therefore increases its absorption behaviour or when the substance tends to form clusters within the polymer. Also a combination of Langmuir and Flory-Huggins isotherms is discussed.

Diffusion in polymers

The total amount of a substance diffusing through a material is conserved. This is expressed in the continuity equation $\frac{\partial c}{\partial t} + \text{div } j = 0$ (Crank 1975) with the flux density denoted as j . The gradient of the chemical potential μ (Fließbach 2006) is the driving force of diffusion: $j = -\frac{c}{\beta} \text{grad } \mu$ (Peterlin 1985). Here, β is the frictional resistance.

In the following we assume that the sorption is described by Henry's law. In the case of a more general sorption isotherm we can approximate it by a Henry isotherm at least in the limit case of low substance concentration. Then Fick's first

law $j = -D \text{grad } c$ (Peterlin 1985) with the diffusion coefficient D is obtained. Inserting this into the continuity equation gives Fick's second law $\frac{\partial c}{\partial t} = D \Delta c$, assuming that D is not a function of position or concentration. Especially important is the stationary case where the concentrations are constant in time.

An analogous diffusion equation can also be derived in the case that the sorption isotherm is of a more general form or the diffusion coefficient depends on other variables. However an analytical solution of this equation together with suited initial and boundary conditions is possible only in special cases. In general, numerical methods like the finite element or finite difference method (Marek and Götz 1995) are required.

Examples

Ethylene Vinyl Alcohol Copolymer (EVOH) is one of the most important polymers with barrier properties against oxygen. However these barrier properties are considerably reduced when a sufficient amount of water vapour is absorbed by EVOH (Nentwig 2006). As long as the water content is small the oxygen permeability of EVOH slightly decreases by absorption of additional water molecules since these occupy free volume which therefore is no longer available for oxygen diffusion (Zhang et al. 2001). When the concentration of absorbed water molecules is high they weaken the hydrogen bonds between the polymer chains and therefore increase their mobility resulting in a higher permeability (Zhang et al. 2001).

Permeation through glassy polymers can be described by the dual-mode sorption model (Stern and Trohalaki 1990). Here it is assumed that a substance absorbed in the polymer consists of two fractions which are locally in equilibrium with each other and possess different mobilities. For the sorption of the one fraction in the polymer matrix Henry's law is valid. The sorption of the other fraction takes place in microcavities and is therefore described by a Langmuir isotherm. These examples show how complex the sorption and diffusion behavior of substances in polymers can be. In order to obtain realistic results this behavior has to be included into the equations describing the permeation processes in barrier materials.

Polymeric multilayer films

Most packaging films contain several polymeric layers. Such multilayer films are produced by coextrusion, lamination or lacquering.

In the following the transmission rate Q through a multilayer film in stationary case will be derived from the correspondent values Q_i for the single layers. To this end the interfaces between the layers are considered. In thermal equilibrium the chemical potential is continuous at interfaces. Due to the conservation of the amount of the permeating substance also the normal component of the flux density is continuous there in stationary state. These facts result in the following equation (Langowski 2008) which shows that with regard to the permeation resistance a multilayer film can be considered as a serial connection of the single layers:

$$\frac{1}{Q} = \sum_i \frac{1}{Q_i}. \quad (1)$$

INORGANIC BARRIER MATERIALS

The barrier properties of polymers can significantly be improved by their combination with inorganic nanomaterials. In the first section the integration of nanoparticles into polymers will be considered. Afterwards a model for the permeation through barrier structures containing a nanoscale inorganic layer deposited on a polymeric substrate will be presented.

Inorganic nanoparticles in polymers

In literature various inorganic nanoscale materials, e.g. layered silicates (Langowski 2008) and graphene (Kim et al. 2010), are reported as fillers of polymers in order to improve their barrier properties.

The permeation through a polymer matrix with dispersed particles was theoretically studied in (Nielsen 1967). Considering the reduction of the free volume for permeation as well as the extension of the permeation paths an effective permeability of this system was derived for an ideal case. The calculation shows that optimum barrier properties are obtained for a high aspect ratio of the particles explaining the experimental studies performed with nanoscale platelets.

For oxygen there is good agreement between the reported experimentally and theoretically obtained permeabilities (Langowski 2008). However in the case of water vapor permeation the experimental values are significantly higher than the theoretical values. This is explained by the absorption of water within agglomerates formed by these nanoscale platelets (Langowski 2008).

Therefore, in terms of its effective permeability a polymeric layer containing inorganic particles can be integrated into the continuum theoretic model of multilayer films without the necessity to define the positions of the individual particles explicitly.

Inorganic barrier layers on polymers

The barrier properties of a polymeric film can be improved by up to several orders of magnitude due to deposition of a nanoscale inorganic layer on top of it (Langowski 2008). Typical materials are aluminium and transparent oxides like silicon oxide. Mainly they are applied by physical vapour deposition in vacuum, e.g. by thermal or electron beam evaporation (Kienel and Sommerkamp 1995; Langowski 2008).

The permeation of oxygen through inorganic layers is assumed to take place within defects having diameters of several nanometers to micrometers (Langowski 2008). Such defects are caused by surface roughness or particles on the polymer surface during deposition of the inorganic material. A further possibility for oxygen permeation are cracks which arise due to mechanical stress when the film is bent or winded up (Yanaka et al. 2001).

The permeation of water vapour, however, cannot be explained only due to the mentioned types of defects. In contrast, additional permeation mechanisms for water vapour have to exist. They are assumed to take place within defects in subnano- up to nanoscale, e.g. at grain boundaries, where water vapour can condense and diffuse in liquid state (Langowski 2008).

In (Roberts et al. 2002) a model for permeation in SiO_x films is presented which contains defects of three different ranges of size. Here it is assumed that permeation of oxygen and water vapour takes place mainly through defects which are larger than 1 nm or which are between 0.2 and 0.3 nm, respectively. In contrast, the lattice is believed to be nearly impermeable for these substances. Measuring the activation energy of permeation confirms that the effect of an oxide layer on top of a polymer substrate is to constrain oxygen permeation to the defects whereas for water vapor a chemical interaction with the oxide exists (Henry et al. 2003).

Continuum theoretical modeling of permeation through an inorganic layer

With the objective to integrate inorganic barrier layers into the continuum theoretical model of multilayer films effective permeabilities for oxygen and water vapour can be defined for them. However, it will be discussed that the geometric definition of defects within the model should give more realistic results.

Therefore, a model of an inorganic layer is presented which contains geometrically defined, periodically distributed defects (Langowski 2008). Oxygen permeation is possible only within these defects. In contrast, nanodefects which are responsible for the additional permeation paths for water vapour are considered as a quasicontinuum. Therefore these are modelled in terms of an effective inorganic matrix permeability.

In the next sections results of the numerical simulation of oxygen and water vapour permeation through barrier structures are shown. Thus a structure containing an inorganic layer on a polymer and possibly a polymeric material as a top layer is defined based on the presented model. The resulting diffusion equation is numerically solved by the finite volume method (Marek and Götz 1995).

Permeation through the structure „Polymer / inorganic layer“

For a polymer inverse proportionality between the stationary oxygen transmission rate and the thickness can be derived from Fick's first law. However, numerical calculation shows that this relation for a polymer substrate coated by an inorganic layer is valid only for small substrate thickness. Above a critical thickness the transmission rate decreases very slowly as a function of the thickness (Langowski 2008; Miesbauer and Langowski 2010). This is explained by numerical calculation of the stationary oxygen concentration in the coated polymer substrate which shows that a high concentration gradient exists only near the defects. Therefore, mainly the barrier performance of that part of the substrate is important.

The oxygen transmission rate Q of the considered structure is proportional to the permeation coefficient P of the polymer since oxygen permeation through the inorganic layer takes place within defects which only constrain the region of permeation. Therefore the discussion shows that for a technically reasonable substrate thickness above the critical thickness the ratio $\alpha := Q/P$ depends substantially only on the inorganic defect structure but not on the polymeric substrate thickness (Langowski 2008).

This means that the permeation coefficient, i.e. the product of the sorption and diffusion coefficients, contributes as a factor to the transmission rate of the structure. Therefore it is not reasonable to assign an effective permeability to the inorganic layer which would allow to describe the permeation resistance of the structure as a serial connection similar to (1). Such a simplification is even more problematic due to the fact that also the positions of the individual defects will have an influence on the transmission rate, especially in barrier structures which contain more than one inorganic layer (Langowski 2008; Miesbauer and Langowski 2010).

The factor a can be analytically calculated in the case of substrates above the critical thickness and inorganic layers with circular defects having small total area fraction (Prins and Hermans 1959; Langowski 2008). This calculation shows that the factor a does not depend only on the total area fraction of the defects but on the sizes of the individual defects. Regarding water vapour permeation the considered system can be considered as a parallel connection of two permeation paths, i.e. the inorganic matrix and the defects (Miesbauer et al. 2008; Miesbauer and Langowski 2011). The total transmission rate is therefore the sum of these both contributions. The influence of defect permeation to matrix permeation and vice versa can be neglected if the total area fraction of defects is small or if the permeation coefficient of the inorganic matrix is much smaller than the one of the polymer, respectively.

Permeation through the structure „Polymer / inorganic layer / polymeric layer“

Aside from the deposition of inorganic layers the barrier properties of a film can also be improved by coating it with a polymeric material. We consider a polymeric layer of thickness d_2 and permeability coefficient P_2 on top of a polymer substrate with values d_1 and P_1 . Equation (1) shows that the application of the polymeric layer reduces the transmission rate by a factor of $1+P_1d_2/P_2d_1$. Since $d_2 \ll d_1$ in general, a significant barrier improvement can be obtained only if $P_2 \ll P_1$.

However, the application of a polymeric layer on top of an inorganic layer deposited on a polymer substrate can result in a much better barrier improvement. If the thicknesses of polymer substrate and polymeric layer are both larger than the critical thickness the oxygen transmission rate Q of the barrier structure “polymer / inorganic layer / polymeric layer” is given by (Langowski 2008)

$$\frac{1}{Q} = \frac{1}{a} \left(\frac{1}{P_1} + \frac{1}{P_2} \right). \quad (2)$$

The factor a defined in the previous section applies to both polymeric materials since they are in contact with the same inorganic layer.

The oxygen transmission rate is then reduced due to the polymeric layer by a factor of $1+P_1/P_2$. Therefore, is not relevant here when the polymeric layer has a thickness which is lower than that of the polymer substrate. This is explained by the result that the oxygen barrier properties of a polymeric material in contact with an inorganic layer are dominated by that region which is close to this layer.

The barrier improvement is even better if the polymeric material coated on top of the inorganic layer can fill its defects. Numerical simulation shows that the influence of the defect

filling on the oxygen transmission rate gets more relevant if the defect areas are reduced or the inorganic layer thickness is increased (Miesbauer et al. 2008; Miesbauer and Langowski 2010). The influence of defect filling can be included into (2) by an additional summand (Miesbauer and Langowski 2011).

ACTIVE BARRIER MATERIALS

The barrier properties of films can also be improved by active materials which are integrated into polymers or adhesives or applied e.g. by vacuum deposition (Nentwig 2006; Day 2008; Wanner 2010). Active barrier materials either possess a high absorption capacity for the permeating substance or form a chemical bonding with it. Alternatively, they can catalyze the chemical reaction of the substance with another substance which is included in the packaging.

In the following sections the absorption of water vapour by hygroscopic substances and the reaction of oxygen with scavengers will be discussed. It will be shown how these processes can be integrated into the continuum theoretical model of packaging films.

Water absorbers in packaging films

Water vapour penetrating into a polymeric film can be absorbed by hygroscopic substances contained within it (Nentwig 2006; Day 2008; Sangerlaub 2010). Therefore they hold the humidity in the interior of the packaging for a long time on a low level.

An important example are porous substances like silica gel and zeolites which can absorb a high amount of water in their pores. Other substances chemically react with water, e.g. some salts which can form hydrates.

In the following deliquescent substances will be considered. Important examples of such substances are salts like NaCl. A deliquescent substance begins to absorb water and to dissolve in it when the partial pressure of water vapour reaches a certain value (Mirabel et al. 2000; Sangerlaub 2010). A saturated aqueous solution is formed at this value while the total amount of the substance dissolves. During further absorption at higher partial pressures the solution gets diluted.

A deliquescent substance to be used as a water absorber in a packaging film is dispersed within voids generated in a polymeric layer (Sangerlaub 2010). These voids allow to store the aqueous solution formed during water absorption by the substance.

A continuum theoretical model of water sorption and diffusion in a polymeric layer containing voids and a deliquescent substance therein was developed whereas the voids are not geometrically defined. Instead similar to the dual-mode sorption model absorbed water is assumed to consist of two different fractions. These are characterized by their concentrations within the material and are locally in equilibrium with each other.

One fraction is absorbed within the polymer matrix according to Henry’s law so that its transport is described by Fickian diffusion. The absorption of the other fraction is caused by the deliquescent substance and therefore depends on the concentration of this substance and its sorption isotherm. Since the individual voids are assumed to have only a small

volume and to be not connected with each other no direct transport of this fraction is considered.

This current model allows to calculate the transport of water in the material above the deliquescence point of the substance. In an advanced model also the influence of the finite total volume fraction of the voids will be considered by combining the Langmuir sorption model with the sorption isotherm of the deliquescent substance. Another extension of the model will allow to describe also the processes at the deliquescence point where the sorption isotherm of the substance possesses a vertical section.

Oxygen scavengers in packaging films

The ingress of oxygen into the interior of a packaging can be delayed due to scavengers which are integrated into the packaging material. A review of oxygen scavengers can be found in the literature (Day 2008; Wanner 2010). In this section two important examples will be presented.

Permeating oxygen can be chemically bound by metallic particles contained in a polymeric layer. However, the kinetics of metal oxidation strongly depends on the presence of water and catalysts and on the pH value. For example, iron is electrochemically oxidized to iron(II)hydroxide and subsequently to hydrated iron(III)oxide when a humid environment is caused by a liquid product (Mortimer 1987; Wanner 2010). This reaction is catalyzed by NaCl which is also integrated into the polymer.

Another possibility is the chemical reaction of permeating oxygen with hydrogen which is introduced by modified atmosphere packaging. Within the packaging material the reaction is catalyzed by a vacuum deposited nanoscale metal layer, e.g. platinum or palladium, at whose surface the molecules of both reactants are dissociated and adsorbed (Mortimer 1987; Wanner 2010). The reaction is described by the Langmuir-Hinshelwood mechanism in contrast to the Eley-Rideal mechanism where only one reactand is adsorbed and the other remains in gas phase (Wanner 2010).

In order to extend the continuum theoretical model of multilayer films to active layers the kinetics of chemical reactions taking place within layers or at surfaces have to be considered. Here, only the case of an irreversible chemical reaction of the permeant with a scavenger dispersed within a polymeric layer is described.

The reaction rate f is defined as the amount of permeant reacting per time and volume and it depends on the concentrations of the permeant and of all other reaction partners and catalysts. Including it in the continuity equation extends the diffusion equation to a reaction-diffusion equation

$$\frac{\partial c}{\partial t} = D \Delta c + f(c, \dots). \quad (3)$$

So, when the permeation and reaction of oxygen with iron and water vapour are modelled also the consumption of these two substances due to reaction as well as the diffusion of water vapour have to be considered. However, we will neglect these influences here by the assumption that iron and water are available in a sufficient amount. Additionally we assume that the oxygen concentration in the polymer is sufficient low so that we can approximate f by a linear function, i.e. the reaction is of first order. With the reaction constant k this results in

$$\frac{\partial c}{\partial t} = D \Delta c - k c. \quad (4)$$

Based on these assumptions, the transient permeation of oxygen through a film consisting of two polymeric layers was simulated using the finite volume method. Three cases were considered whereas either in one of the both layers or in none of them a chemical reaction of first order was defined.

Thus, the same thicknesses, diffusion and sorption coefficients were assigned to both layers. This means that an increase of the passive barrier due to scavenger particles dispersed in the polymer as it was discussed for arbitrary particles in an earlier section is neglected.

The calculations show that the time-dependent flux from the film into the half space with low partial pressure is reduced by the scavenger and that it has no influence whether the scavenger is integrated into the one or into the other layer. However, the flux from the half space with high partial pressure into the film is higher if this half space is in contact with the scavenging layer than with the other layer. This is true also in the stationary state where the difference between the fluxes entering or leaving the film, respectively, equals the total reaction rate within the scavenging layer. Consequently, a scavenging layer has to be protected by a passive barrier layer against environment in order to maintain the scavenger activity for a sufficient long time.

SUMMARY

Packaging films containing several layers of passive and active barrier materials are used to protect food against oxygen and water vapour and therefore to preserve their quality. The numerical calculation of permeation through film structures can assist their design in order to obtain optimal barrier properties.

Therefore a continuum theoretical model for the permeation of oxygen and water vapour through multilayer structures was established. Thus the permeation through polymers is divided into sorption and diffusion processes. A large variation of sorption mechanisms and therefore of sorption isotherms can be found for different polymers.

The basic principles of diffusion are conservation of the amount of matter and the fact that the negative gradient of the chemical potential is the driving force of diffusion. Fick's laws can be derived if sorption is described by Henry's law. In other cases the diffusion equation is more complex: examples are the permeation through EVOH and the dual-mode sorption model. Regarding their barrier properties polymeric multilayer films can be considered as a serial connection.

Afterwards the barrier improvement of polymeric films by inorganic materials was discussed. For a polymer which contains inorganic particles an effective permeability can be derived. More important however is the physical vapour deposition of nanoscale inorganic layers on polymers.

Oxygen permeation through such layers is possible only within defects whereas for water vapour additional permeation mechanisms exist which are modelled in terms of an inorganic matrix permeability. The numerical simulation of oxygen permeation through an inorganic layer on a polymer shows the existence of a critical substrate thickness. In case of water vapour this structure can be considered as a parallel connection of both permeation paths. Additionally a larger barrier improvement factor is obtained when a polymeric layer is applied on top of this structure than on top of a polymer substrate.

Finally, the reduction of the permeation rate by active barrier layers was considered. Absorption of water vapour is possible by different types of hygroscopic materials. An example are deliquescent substances which are dispersed within voids of a polymeric layer. During absorption they form an aqueous solution which is stored within the voids. A model for the permeation of water vapour through such materials was developed.

Permeating oxygen can be chemically bound by reaction with metal particles or by reaction with hydrogen catalyzed at metal surfaces. In order to integrate oxygen scavengers into the permeation model the diffusion equation was extended by a reaction term. Oxygen permeation through a film containing a scavenging layer was numerically calculated. The results shows that such a layer has to be protected by a passive barrier layer against environment.

OUTLOOK

In this paper only the stationary permeation through barrier materials was considered. However, calculations show that the time lag (Langowski 2008) of permeation in barrier structures containing several inorganic layers can be very high (Graff et al. 2004).

Therefore, the presented model for multilayer barrier films will be extended to transient permeation. This will allow to calculate lag times and the time dependent permeation behavior in addition to the stationary state reached for time $\rightarrow \infty$. These studies will lead to a better insight how passive and active barrier materials influence the time lag of permeation. Due to the extension of the time lag possibly a sufficiently low permeation rate within a certain time period can be reached. Consequently, the design of barrier films providing further improved life times of packed products will be possible.

ACKNOWLEDGEMENT

The author thanks Prof. Dr. H. C. Langowski, Dr. K. Noller, Dr. C. Stramm, Dr. E. Küçükpinar-Niarchos, Dr.-Ing. K. Müller and S. Sänglerlaub for valuable suggestions and discussions.

REFERENCES

- Baner, A.L. and O.G. Piringer. 2008. "Preservation of Quality Through Packaging". In *Plastic Packaging - Interactions with Food and Pharmaceuticals 2008*, O.G. Piringer and A.L. Baner (Eds.). Wiley-VCH, Weinheim, 1–13.
- Crank, J. 1975. *The Mathematics of Diffusion*. Oxford University Press, Oxford.
- Day, B.P.F. 2008. "Active Packaging of Food". In *Smart Packaging Technologies for Fast Moving Consumer Goods 2008*, J. Kerry and P. Butler (Eds.). Wiley, Chichester, 1–18.
- Fließbach, T. 2006. *Statistische Physik – Lehrbuch zur Theoretischen Physik IV*. Elsevier-Spektrum Akademischer Verlag, Heidelberg.
- Graff, G.L., et al. 2004. *J APPL PHYS* 96, No. 4, 1840–1849.
- Henry, B.M., et al. 2003. "Permeation Studies of Transparent Barrier Coatings". In *46th Annual Technical Conference Proceedings – Society of Vacuum Coaters*. 600–605.
- Kienel, G. and P. Sommerkamp. 1995. "Aufdampfen im Hochvakuum". In *Vakuumbeschichtung 2 – Verfahren und Anlagen 1995*, G. Kienel and K. Röhl (Eds.). VDI Verlag, Düsseldorf.
- Kim, H., et al. 2010. *MACROMOLECULES* 43, No.16, 6515–6530.
- Lewis, J.S. and M.S. Weaver. 2004. *IEEE J SEL TOP QUANT* 10, No.1, 45–57.
- Langowski, H.-C. 2008. "Permeation of Gases and Condensable Substances Through Monolayer and Multilayer Structures". In *Plastic Packaging - Interactions with Food and Pharmaceuticals 2008*, O.G. Piringer and A.L. Baner (Eds.). Wiley-VCH, Weinheim, 297–347.
- Marek, R. and W. Götz 1995. *Numerische Lösung von partiellen Differentialgleichungen mit finiten Differenzen*. Moreno-Verlag, Buchloe.
- Miesbauer, O. and H.-C. Langowski. 2010. "Nanoskalige Komponenten in Barrierefolien". In *Nanotechnologie in der Lebensmittelindustrie. Zum Kenntnisstand nanoskaliger Wirkstoffcarrier in Lebensmitteln und Verpackungsmaterialien 2010*, H. Weber (Ed.). Behr's Verlag, Hamburg, 45–67.
- Miesbauer, O. and H.-C. Langowski 2011. "FEM-Simulation der stationären und instationären Gaspermeation durch Barrierefolien". In *19. Neues Dresdner Vakuumtechnisches Kolloquium* (Dresden, Oct.19-20).
- Miesbauer, O.; M. Schmidt; and H.-C. Langowski 2008. "Stofftransport durch Schichtsysteme aus Polymeren und dünnen anorganischen Schichten" *Vakuum in Forschung und Praxis* 20, No. 6, 32–40.
- Mirabel, P., et al. 2000. *J CHEM PHYS* 113, No. 18, 8200-8205.
- Mortimer, C.E. 1987. *Chemie*. Thieme, Stuttgart.
- Müller-Plathe, F. 1994. *ACTA POLYM* 45, 259–293.
- Nentwig, J. 2006. *Kunststoff-Folien: Herstellung - Eigenschaften - Anwendung*. Carl Hanser Verlag, München.
- Nielsen, L.E. 1967. *J MACROMOL SCI A*. 1, No.5, 929–942.
- Peterlin, A. 1985. *COLLOID POLYM SCI* 263, No.1, 35–41.
- Prins, W. and J. J. Hermans. 1959. *J PHYS CHEM* 63, No. 5, 716–719.
- Roberts, A.P., et al. 2002. *J MEMBRANE SCI* 208, 75–88.
- Robertson, G.L. 2006. *Food Packaging: Principles and Practice*. CRC Press, Boca Raton, FL.
- Rogers, C.E. 1985. "Permeation of Gases and Vapours in Polymers". In *Polymer Permeability 1985*, J. Comyn (Ed.). Chapman & Hall, London, 11–73.
- Sänglerlaub, S. 2010. *Verpackungs-Rundschau* 61, No.2, 33–34.
- Stern, S.A. and S. Trohalaki. 1990. "Fundamentals of Gas Diffusion in Rubbery and Glassy Polymers". In *Barrier polymers and structures 1990*, W.J. Koros (Ed.). ACS Symposium Series 423, American Chemical Society, Washington DC, 22–59.
- Wanner, G.T. 2010. *O₂-zehrende und -anzeigende Packstoffe für Lebensmittelverpackungen*. Dissertation, TU München.
- Yanaka, M., et al. 2001. *THIN SOLID FILMS* 397, 176–185.
- Zhang, Z., et al. 2001. *J APPL POLYM SCI* 82, 1866–1872.

AUTHOR BIOGRAPHY

OLIVER MIESBAUER studied Physics (Technical Physics) at the Technische Universität München (Diploma in 2002). Subsequently he studied Mathematics at the LMU Munich (Master of Science in 2005). Currently he is a scientist at the Fraunhofer Institute for Process Engineering and Packaging IVV where he works on the development of barrier materials for technical products and on the modeling of permeation mechanisms (Ph. D. Thesis).

AUTHOR LISTING

AUTHOR LISTING

Antonio A.L.	59/62/77	Martins A.	77
Barreira J.C.M.	77	Miesbauer O.	91/98
Barros L.	59	Oliveira M.B.P.P.	77
Bento A.	59/62	Osterroth I.	45
Botelho M.L.	62	Pecha P.	72
Braun A.	15	Pechova E.	72
Briesen H.	10/15	Petermeier H.	45/52
Butler F.	80	Pieters J.G.	34
Cadavez V.	80	Quintana B.	62
Carocho M.	59	Ramalhosa E.	62
Cummins E.	29	Reichmann E.	91
Cushen M.	29	Ronsse F.	34
Dewettinck K.	34	Roudot A.-C.	67
Duangkhamchan W.	34	Sanahuja S.	91
Elts E.	10	Sanchez G.	62
Fernandes Â	77	Sängerlaub S.	91
Ferreira I.C.F.R.	59/77	Sheridan J.	80
Fischl R.	20	Stamati I.	5
Franke S.	45/52	Strobl V.	52
Ganzenmüller G.C.	20	Trindade M.	62
Gonzales-Barron U.	80	Van Derlinden E.	5
Greiner M.	10	Van Impe J.	5
Höfler J.	45/52	Voigt T.	45
Hofman R.	72	Wesolek N.	67
Kałuska I.	59	Zacherl C.	20
Langowski H.-C.	45/52		
Logist F.	5		